Interface charge engineering for normally-off operations in GaN-based metal-insulator-semiconductor (MIS) devices using AlTiO insulators

NGUYEN DAI DUONG

Japan Advanced Institute of Science and Technology

Doctoral dissertation

Interface charge engineering for normally-off operations in GaN-based metal-insulator-semiconductor (MIS) devices using AlTiO insulators

by

NGUYEN DAI DUONG

Supervisor: Professor Toshi-kazu SUZUKI

Graduate School of Advanced Science and Technology

Japan Advanced Institute of Science and Technology

Material Science

March, 2022

Abstract

Wide-gap semiconductor GaN is anticipated for its potential to overcome the trade-off between speed and power in semiconductor devices. In particular, GaN-based metal-insulator-semiconductor heterojuction field-effect transistors (MIS-HFETs) have been investigated extensively owing to the merits of gate leakage reduction and passivation to suppress the current collapse. As a gate insulator of GaN-based MIS-HFETs, various materials such as Al_2O_3, TiO_2, TaON, AlN, BN, and so on have been employed and investigated. Although a wide energy gap E_g and a high dielectric constant k_{ins} are preferable for a gate insulator, a trade-off between E_g and k_{ins} generally exists for insulators. Aluminum titanium oxide Al_xTi_yO (AlTiO), an alloy of Al_2O_3 ($E_g \sim 7$ eV, k_{ins} 10) and TiO_2 ($E_g \sim 3$ eV, $k_{ins} \sim 60$) is a versatile insulator since its properties can be modified for energy gap engineering (E_g control) and dielectric constant engineering (k_{ins} control) via its composition. Although there still exists a trade-off between E_g and k_{ins}, we can choose an AlTiO composition according to applications, considering the trade-off. On the other hand, at the interface between an oxide gate insulator and a negatively polarized semiconductor surface, such as a Ga-face (Al)GaN surface, a positive fixed charge tends to be generated and to neutralize the negative polarization charge. The positive interface fixed charge has a significant impact on threshold voltages; a high-density positive interface fixed charge shifts the threshold voltage negatively. The technology aiming to control the threshold voltage by controlling the positive interface charge is called "interface charge engineering".

In this work, we investigated interface charge engineering in AlTiO/AlGaN/GaN MIS devices by evaluating the positive interface fixed charge density depending

on the composition of AlTiO obtained by atomic layer deposition. We found a trend that the interface fixed charge density decreases with a decrease in the Al composition ratio, i.e. increase in the Ti composition ratio. Moreover, X-ray photoelectron spectroscopy characterization of AlTiO/AlGaN reveals a relation between the positive interface fixed charge density and the bonding states of Ga: an increase in Ga-N bonding state or a decrease in Ga-O bonding state leads to an increase in the the positive interface fixed charge density.

In order to realize normally-off operations with good transport properties in AlTiO/AlGaN/GaN MIS-FETs, we investigated combining the interface charge engineering and partial gate recess method with a thick remaining AlGaN layer. For a composition of $x/(x+y) = 0.73$, the positive fixed charge at AlTiO/recessed-AlGaN is significantly suppressed compared to that at Al_2O_3/recessed-AlGaN, leading to a positive slope in the relation between the threshold voltage and the AlTiO insulator thickness. As a result, we successfully obtained normally-off operations in partially-gate-recessed AlTiO/AlGaN/GaN MIS-FETs with a threshold voltage of 1.7 V and good transport properties. For a composition of $x/(x + y) = 0.73$, low-frequency noise characterization of AlTiO/AlGaN/GaN MIS-FETs with different remaining AlGaN thickness reveals two trap levels in AlTiO, independent of AlGaN thickness. Moreover, the noise magnitude increases with a decrease in the remaining AlGaN thickness, owing a decrease in the channel electron mobility.

In summary, we successfully obtained normally-off operation in GaN-based MIS devices by interface charge engineering using AlTiO insulators and investigated the AlTiO/AlGaN interface by X-ray photoelectron spectroscopy and low-frequency noise.

Keywords: III-V compound semiconductor, AlGaN/GaN, AlTiO, interface charge engineering, normally-off operation

Acknowledgment

I would like to express my sincere gratitude to Professor Toshi-kazu Suzuki for guiding me through this work. His in-depth knowledge provided me new lessons everyday, and his working style is a role model that influenced me the most.

I would like to express my thanks to Professor Hideyuki Murata for his instruction in minor research and Associate Professor Masashi Akabori for his support during my course.

Many thanks to my lab members, Yuchen Deng and Kazuya Uryu, for their support during experiments. Many thanks to my friends, who are in badminton club and tennis club, for playing and sharing the laughter with me. These moments have made the graduate school life so enjoyable.

Finally, I would like to express my heartfelt gratitude to my family and my girlfriend Ton Nu Thanh Nhan for their unconditional supports.

Contents

Chapter 1

Introduction

1.1 Compound semiconductors and their applications

While Silicon-based devices still dominate the market for digital integrated circuit, compound semiconductors are having more and more applications which require high-speed wireless-communication and/or high-power switching. For the high-speed wireless-communication applications, the demand for high-quality-content exchange is skyrocketing through various forms of communication devices such as mobile phone, television, and satellite. Figure 1.1(a) exhibits the requirement range for some wireless-communication applications [1], in which each semiconducting material is suitable for some applications based on its physical properties. For examples, Si-based transistors [2] are suitable for mobile communications which require a moderate frequency $\sim$ 1 GHz and low power $\sim$ 1 W, whereas GaAs-based transistors [3, 4] are employed for radar communications where working frequency up to $\sim$ 100 GHz are required. For future wireless-communication system, realization of high-speed and high-power devices is an important step [5]. For the power-switching applications shown in Fig. 1.1(b) [6], the frequency range is downscaled by 10^5 orders while the power range is upscaled by the same orders in comparison with these of the wireless-communication applications. In these applications, the employed semiconductor devices should have the capability to

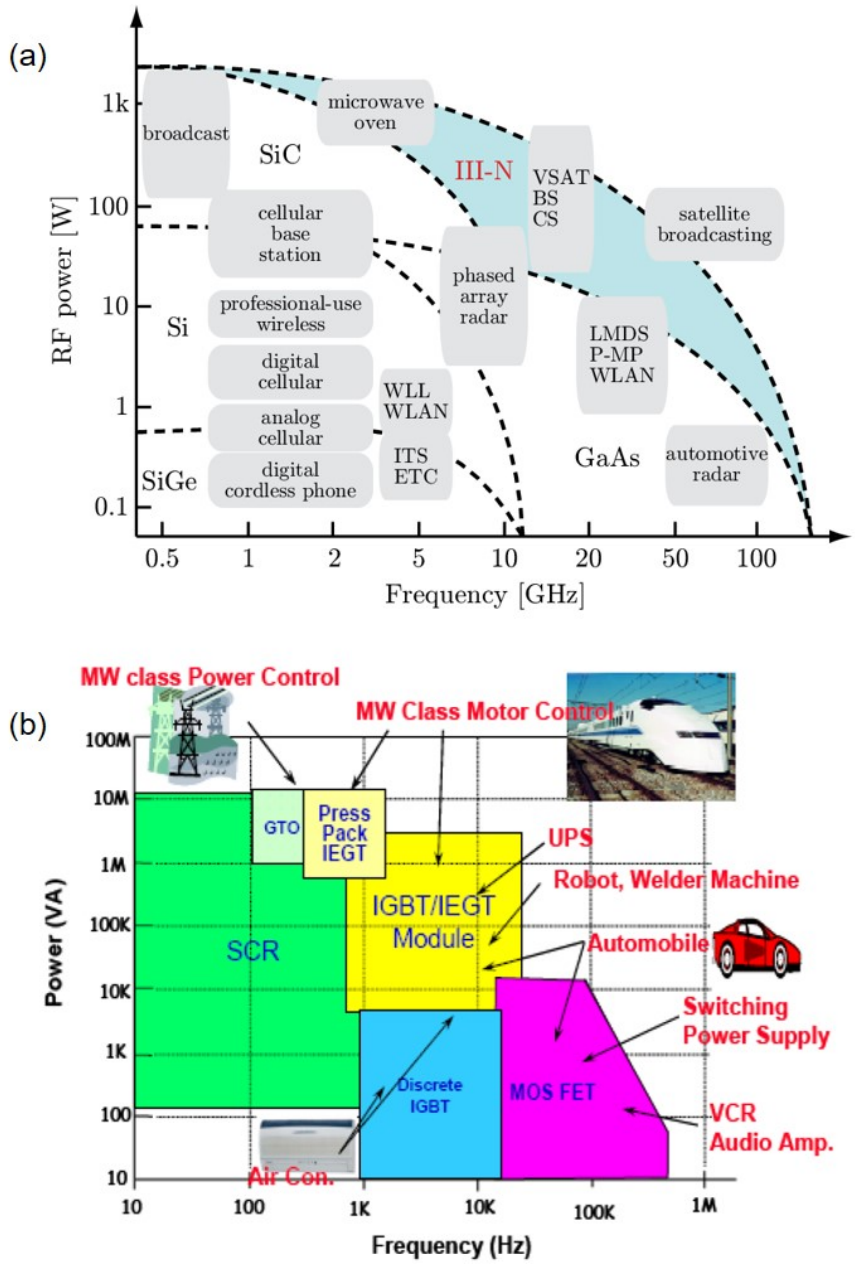

Figure 1.1: Relation between frequency and power for (a) wireless-communication applications [1] and (b) power-switching applications [6].

handle a large power. Depending on the application, a moderate switching speed is sometimes required. However, there is a trade-off between speed (frequency) and power for both applications, which means that the devices which are required to operate at high frequency cannot work at high power and vice versa, the devices which are required to work at high power cannot operate at high frequency.

Let us discuss about the trade-off between operating speed and power of elec-

tronic devices such as field-effect transistors (FETs). The operating frequency of the devices can be expressed by current-gain cut-off frequency f_{T} given by

$$f_{\mathrm{T}} \simeq \frac{1}{2\pi\tau_{\mathrm{tr}}} = \frac{v}{2\pi L_{\mathrm{G}}}, \tag{1.1}$$

where τ_{tr} is the transition time, v is the carrier velocity, and L_{G} is the gate length. The cut-off frequency is a limit that beyond this frequency, an FET can no longer be used for amplification. In technical terms, f_{T} is the frequency at which the current gain, i.e. the ratio of the change in the output current over the change in the input current, equals to 1. Based on Eq. (1.1), to increase f_{T}, we can employ a high-carrier-velocity semiconductor and/or reduce the gate length. Until now, reduction in the gate length of Si-based FETs has led to continuous improvement of device performance [7]. As we approach sub-20-nm dimensions, it becomes increasingly difficult to maintain the required device performance. We have to employ other semiconducting materials with higher carrier velocity. Regarding the carrier velocity, drift velocity v_{d} at low electric field and saturation velocity v_{sat} at high electric field should be taken into consideration. The drift velocity at low electric field is

$$v_{\mathrm{d}} = \mu E = \frac{q\tau}{m^*} E, \tag{1.2}$$

where μ is the electron mobility, $q > 0$ is the electron charge, τ is the scattering time, m^* is the electron effective mass, and E is the electric field under the gate. At low electric field, the electron drift velocity in a material is directly proportional to the electric field, which means that the electron mobility is a constant. Thus a material possessing a high mobility will have a high drift velocity. On the other hand, at high electric field, carriers are accelerated enough to gain sufficient kinetic energy between collisions to emit an optical phonon, which make their velocity drop to 0 before being accelerated again. The saturation velocity, which is the velocity the carrier reaches before emitting a phonon, is given by

$$v_{\mathrm{sat}} = \sqrt{\frac{2\hbar\omega_{\mathrm{op}}}{m^*}}, \tag{1.3}$$

where $\hbar\omega_{\mathrm{op}}$ is the optical phonon energy. From Eq. (1.2) and (1.3), we find that both μ and v_{sat} are proportional to $1/m^*$, thus materials with small m^* are ad-

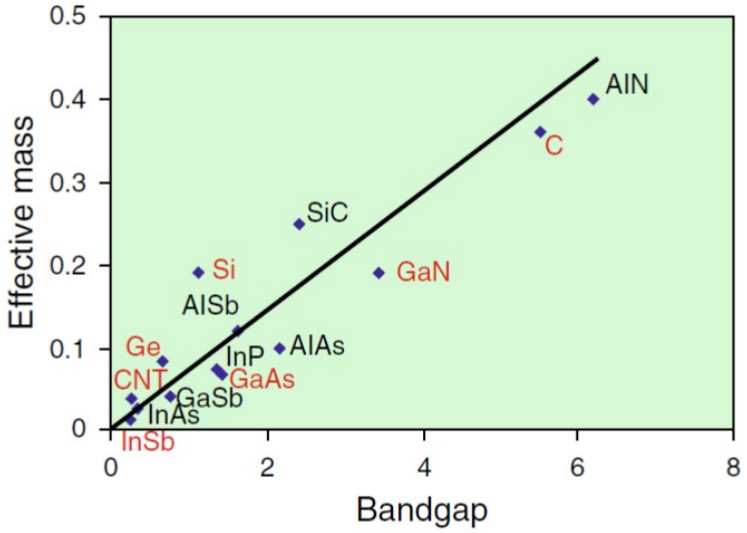

Figure 1.2: Relation between effective mass and bandgap in semiconducting materials [9].

vantageous for high-speed applications. On the other hand, in high-power applications, the applied source-drain voltage is high. Moreover, due to the decrease in the gate length, the electric field under the gate becomes stronger, leading to the breakdown of the semiconductor. Therefore, materials with high breakdown field are advantageous for power-handling applications. The breakdown field F_{Br} of a semiconductor is usually related to its energy gap E_{g} by the relation

$$F_{\mathrm{Br}} \propto E_{\mathrm{g}}^{\alpha}, \tag{1.4}$$

where $\alpha \simeq$ 1-3, making F_{Br} be an increasing function of E_{g} [8]. Thus, for high-power applications, wide-bandgap semiconducting materials are preferable.

In summary, we can conclude that semiconducting materials with small m^* and large E_{g} are advantageous for high-speed and high-power applications, respectively. However, there is a relation between m^* and E_{g} as shown in Fig. 1.2 [9], illustrating a trend that m^* is an increasing function of E_{g}. i.e. $m^* \propto E_{\mathrm{g}}$. Therefore, a trade-off between speed (frequency) and power exists in general cases [10]. However, if we look back at Eq. (1.3) indicating $v_{\mathrm{sat}} \propto \sqrt{\hbar\omega_{\mathrm{op}}}$, which suggests that semiconducting material having a large optical phonon energy and a wide bandgap is suitable for high-speed and high-power applications. A compound semiconductor like GaN holding such physical properties is able to overcome the

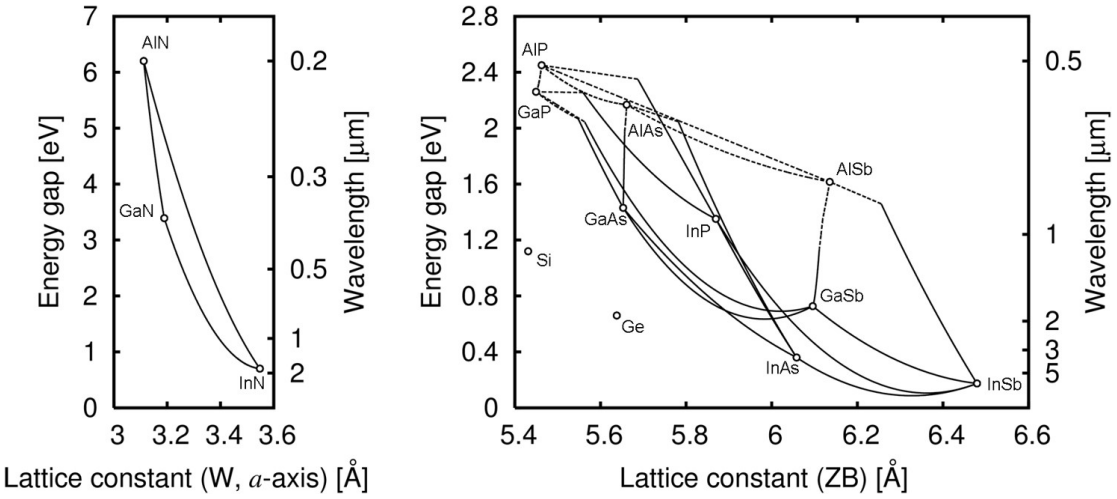

Figure 1.3: The energy gap and corresponding wavelength as functions of the lattice constant for some III-V compound semiconductors [12, 13].

limitations set by the trade-off between speed and power.

1.2 GaN-based semiconductors and related devices

Compound semiconductor devices are obtained by crystalline growth, so heterogeneous integration between the semiconducting materials and the host substrates is important. The heterogeneous integration is divided into two methods: one is direct growth method in which the device material are directly grown on a substrate, and another is separation-bonding method in which the device material is firstly grown on a substrate, then separated (for instance by epitaxial lift-off [11]), and bonded on another substrate. Although the heterogeneous integration method can give various choices for the materials, it also induces non-ideal interfaces between the semiconductor layer and the substrate due to the dissimilarities in the materials. One of the most serious issues is the difference in lattice constants, which can induce serious defects not only at the interface but also in the grown device layers. Figure 1.3 shows the relation between the energy gap and the lattice constant for several III-V compound semiconductors [12, 13]. The di-

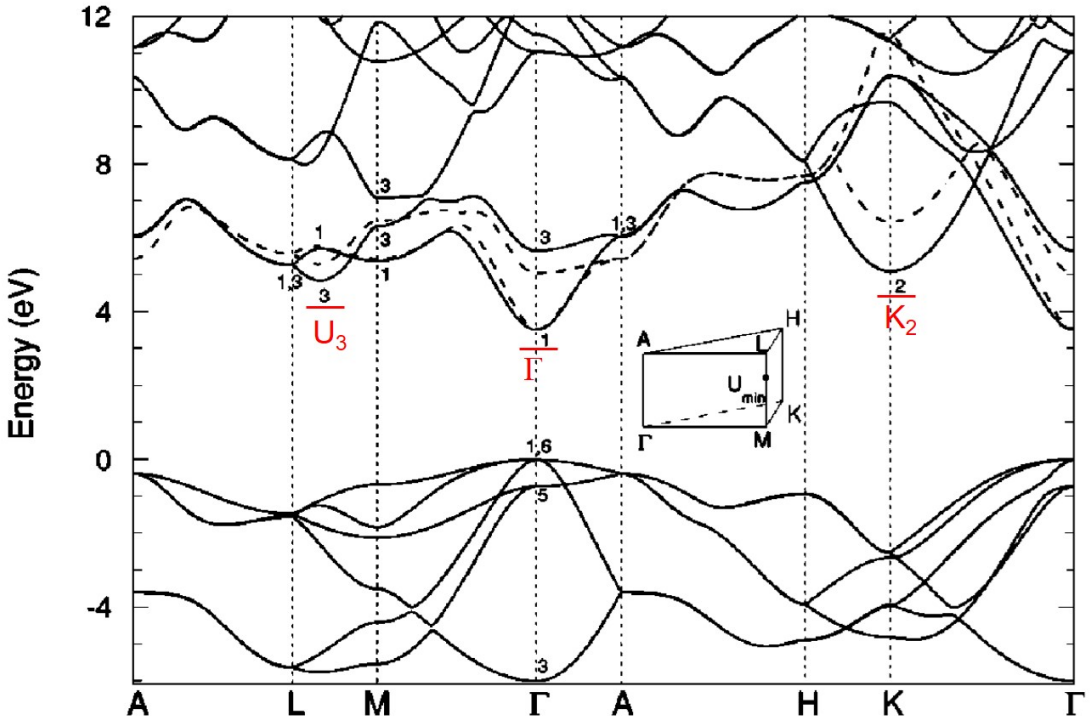

Figure 1.4: The energy band structure of wurtzite GaN [15].

rect growth method is suitable for lattice-matched or small lattice-mismatched systems such as AlGaN on GaN, whereas the separation-bonding method is suitable for large lattice-mismatched systems such as InAs-based ones. However, one difficulty for high-quality GaN growth was the lack of a suitable lattice-matched substrate. It has been solved by low temperature growth of a buffer layer having 16% lattice-mismatch with sapphire substrate by MOVPE (metal organic vapor phase epitaxy) [14]. This technology has enabled the crystal growth quality of GaN, AlN, InN, or their alloys, to the production level.

Figure 1.4 plots the calculation of the energy band structure of wurtzite GaN [15], showing a direct bandgap with a large E_g of 3.4 eV, corresponding to a very high breakdown field of 3.3 MV/cm, which is favorable for high-power applications. Moreover, GaN also has a large valley-separation energy and a large optical phonon energy of 90 meV, leading to a high saturation velocity. Figure 1.5 shows the electron drift velocity as functions the electric field for several semiconductors obtained by Monte Carlo simulation [16]. As expected, GaN possesses a high

Table 1.1: Comparison of electrical properties between GaN and other semiconductors.

Mater.	Bandgap [eV]	Electron mobility [$cm^2/V.s$]	Electron saturation velocity [cm/s]	Breakdown field [V/cm]
Si	1.12	1500	1.0×10^7	3.0×10^5
GaAs	1.42	8500	2.0×10^7	4.0×10^5
InAs	0.36	33000	$\sim 4.0 \times 10^7$	4.0×10^4
SiC	3.33	900	2.0×10^7	3.0×10^6
GaN	**3.39**	**1100**	$\mathbf{2.7 \times 10^7}$	$\mathbf{3.3 \times 10^6}$

electron peak velocity of 2.5×10^7 cm/s and a high electron saturation velocity $\geq 1.5 \times 10^7$ cm/s, which are suitable for high-speed applications. We summarized the physical properties for several semiconducting materials in Table 1.1, showing that GaN is a superior material owing to its high saturation velocity and wide bandgap.

In order to measure the suitability of a semiconducting materials for high-speed and high-power applications, we employ two types of figure of merit (FoM) in the following. The first one is Johnson's FoM, which is given by

$$f_T V_{Br} \leq \frac{F_{Br} v_{sat}}{2\pi}, \tag{1.5}$$

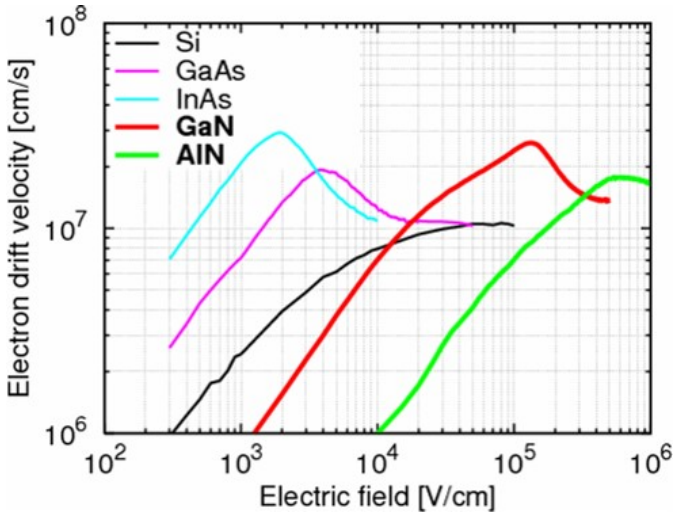

Figure 1.5: Relation between drift velocity and electric field obtained by Monte Carlo simulation [16].

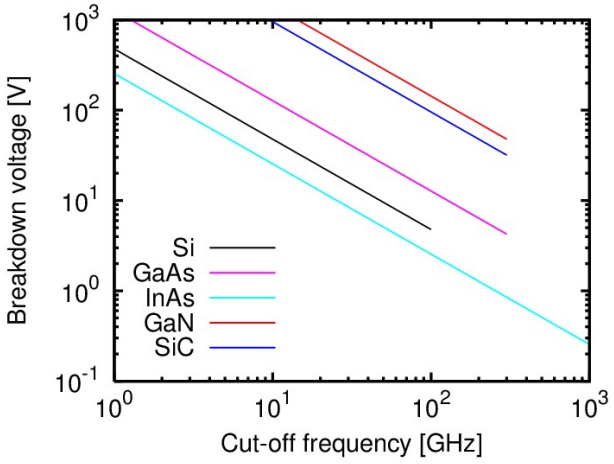

Figure 1.6: Relation between V_{Br} and f_{T} for several semiconductors.

where f_{T} is cut-off frequency and V_{Br} is breakdown voltage. Figure 1.6 shows the relation between V_{Br} and f_{T}; it is clear that GaN is superior than Si or GaAs in both breakdown voltage and cut-off frequency. GaN-based FETs are expected to have high-speed and high-power applications such as power amplifiers for cellular base station, satellite communication, and automotive radar system [17–19], where operating frequency ≥ 10 GHz with high-power output.

The other FoM is Baliga's, which is given by

$$\epsilon_0 k \mu F_{\mathrm{br}}^3 \geq \frac{4V_{\mathrm{br}}^2}{R_{\mathrm{on}}}, \tag{1.6}$$

where ϵ_0 is the vacuum permittivity, k is the dielectric constant of the semiconducting material, and R_{on} is the on-resistance. The relation between R_{on} and V_{br} for several semiconductors is depicted in Fig. 1.7. Baliga's FoM is used to rate the suitability for power-switching applications. Such applications require moderate speed and higher power compared to these of wireless-communication applications. It is clear that GaN with relatively low R_{on} at high V_{Br} is advantageous than other semiconducting materials. Power-switching electronics such as Si-based vertical type MOS (metal-oxide-semiconductor) FETs used in power supply of servers or personal computers, and Si-IGBT (insulated gate bipolar transistor) used in electric vehicles or hybrid cars, are expected to see appearance of GaN-based devices [20].

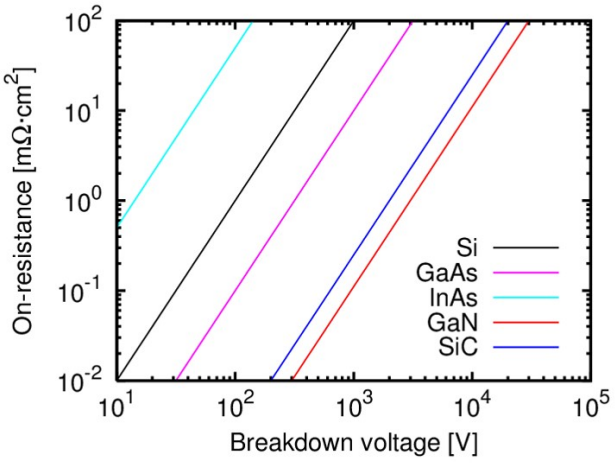

Figure 1.7: Relation between R_{on} and V_{Br} for several semiconductors.

From the above discussion, GaN is expected to break through the speed-power trade-off to realize high-speed and high-power devices. Moreover, GaN can form a heterojunction with AlGaN for higher-speed operation. AlGaN is grown pseudomorphically with a tensile strain to match the lateral constant of Ga-face GaN, which induces spontaneous and piezoelectric polarization effects [21, 22]. The spontaneous polarization comes from an intrinsic asymmetry of the bonding in equilibrium wurtzite crystal structures of AlN and GaN; and the piezoelectric polarization comes from mechanical stress, i.e. tensile or compressive strain of AlGaN and GaN layers. These two effects form a two-dimensional electron gas (2DEG) with high concentration at AlGaN/GaN heterointerface as shown in Fig. 1.8 [22]. Typically, Al composition of 20-30% gives a 2DEG concentration $\simeq 10^{13}$ cm^{-2}, which can be utilized as the channel for AlGaN/GaN heterojunction FETs for high-speed and high-power applications [23]. However, high gate leakage current despite of wide band gap [24–27] and current collapse due to surface electron trapping [28–30] still occur in Schottky AlGaN/GaN FETs.

In order to solve these problems, GaN-based metal-insulator-semiconductor (MIS) devices have been investigated according to the advantages of gate leakage reduction [27] and passivation to suppress the current collapse [28–30], whose schematics is shown in Fig. 1.9. Many types of the gate insulators have been in-

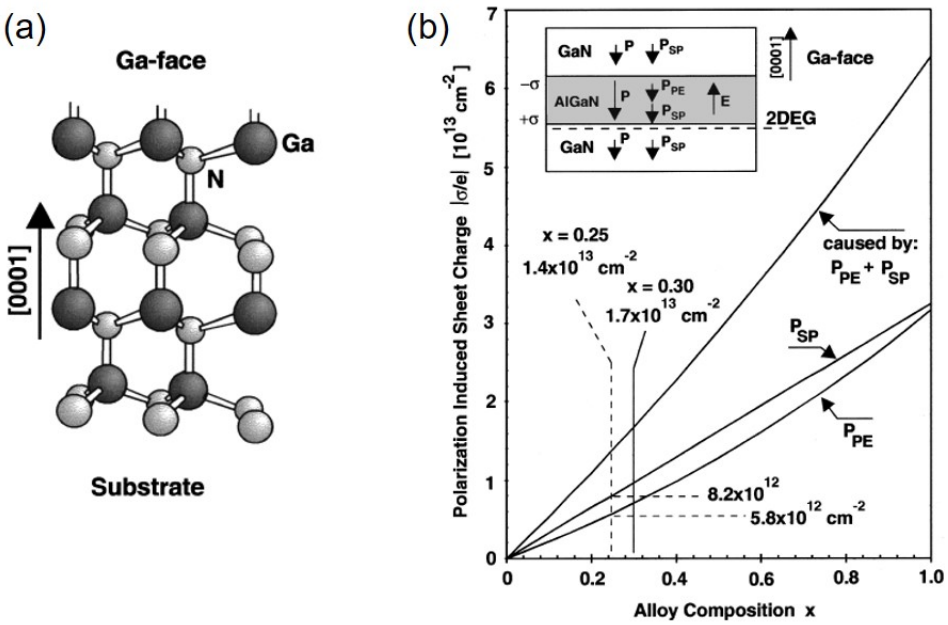

Figure 1.8: (a) Crystal structure of wurtzite Ga-face GaN. (b) Calculated sheet charge density caused by spontaneous and piezoelectric polarization of a GaN-face GaN/AlGaN/GaN heterostructure [22].

tensively investigated, which are oxides such as Al_2O_3 [31–35], HfO_2 [36, 37], TiO_2 [38, 39], AlSiO [40], nitrides such as AlN [41–45], BN [46, 47], and oxynitrides such as TaON [48], AlON [49], and so on. In any cases, understanding and controlling the insulator/semiconductor interface is indispensable for the development of the MIS device technology. In addition to the problem of device instability caused by the interface traps [50], effects of the interface fixed charge are critical issues.

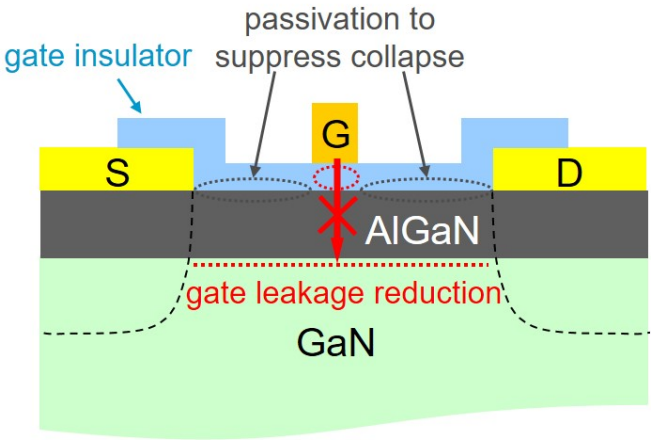

Figure 1.9: A schematic cross section of GaN-based MIS devices.

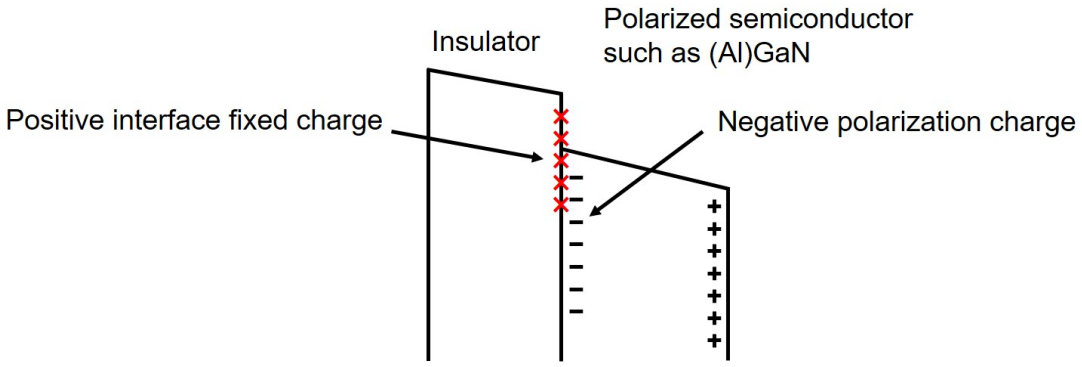

Figure 1.10: The positive interface fixed charge at insulator-semiconductor interface.

Figure 1.10 shows that, when an insulator is deposited on a negatively polarized GaN-based semiconductor surface, a positive interface fixed charge tends to be generated and neutralizes the polarization charge [51–58]. The positive interface fixed charge has significant impact on the threshold voltages. V_{th} is a linear function of the insulator thickness d_{ins} whose slope depends on the positive interface

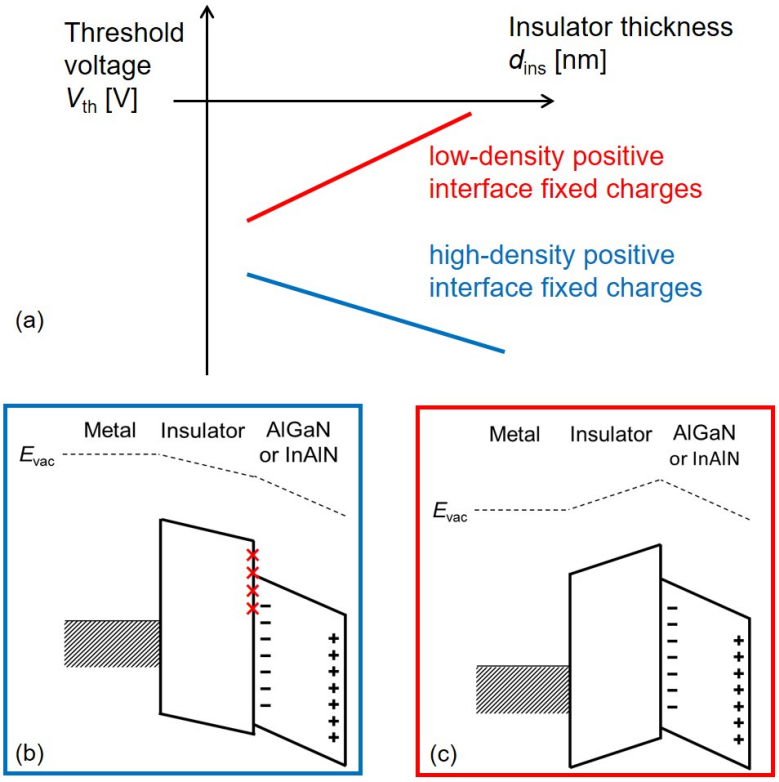

Figure 1.11: (a) V_{th} as functions of d_{ins}. Theoretical band diagram of GaN-based MIS devices when the positive interface fixed charge density is (b) high and (c) low.

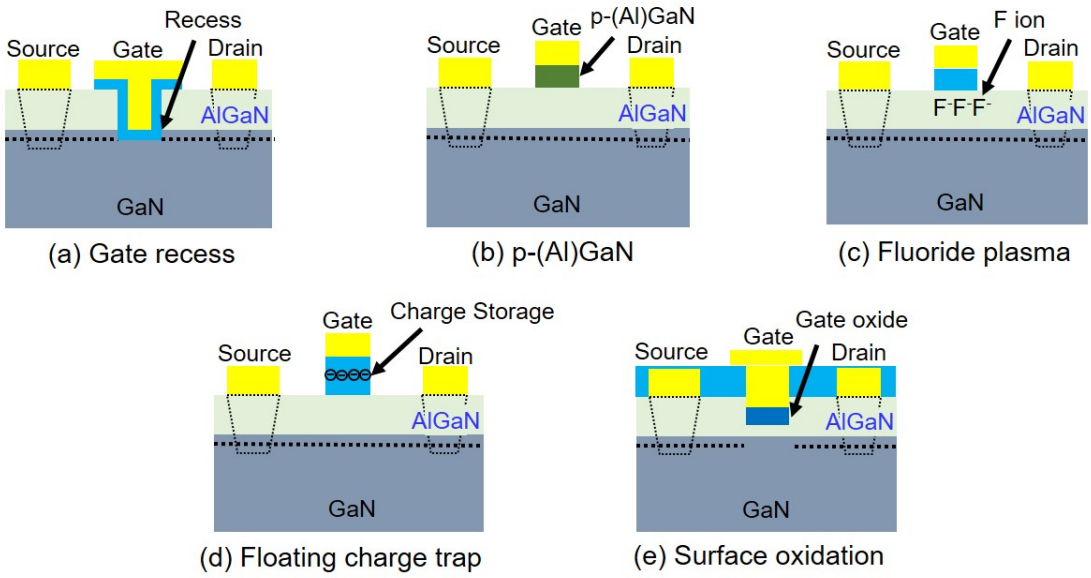

Figure 1.12: Some methods to realize normally-off operations in AlGaN-GaN MIS-FETs.

fixed charge density, as shown in Fig. 1.11(a). If the density of the positive fixed charge is high, forming a band diagram shown in Fig. 1.11(b), $V_{\rm th}$ becomes more negative as $d_{\rm ins}$ increases, which is unfavorable for the device applications. On the other hand, if the density of the positive fixed charge is low, the electric field inside the insulator can be reverted as shown in Fig. 1.11(c), which leads to a positive slope in $V_{\rm th}$-$d_{\rm ins}$ relation. In other words, $V_{\rm th}$ will be more positive when $d_{\rm ins}$ increases, which is favorable for the device applications. Thus, there is a possibility that the threshold voltages can be controlled by controlling the positive interface fixed charge density, which is called "interface charge engineering" [55].

Due to the existence of the 2DEG, AlGaN/GaN MIS-FETs are conventionally normally-on devices. However, there are many applications in which normally-off devices are desirable for fail-safe operations. Towards realization of normally-off AlGaN/GaN devices, several methods, such as partial gate recess [59], full gate recess [60], fluoride plasma treatment [61], p-type (Al)GaN capping [62, 63], selective electro-chemical oxidation [64], and fin-structure formation [65], have been investigated. These methods are illustrated in Fig. 1.12. Among these methods,

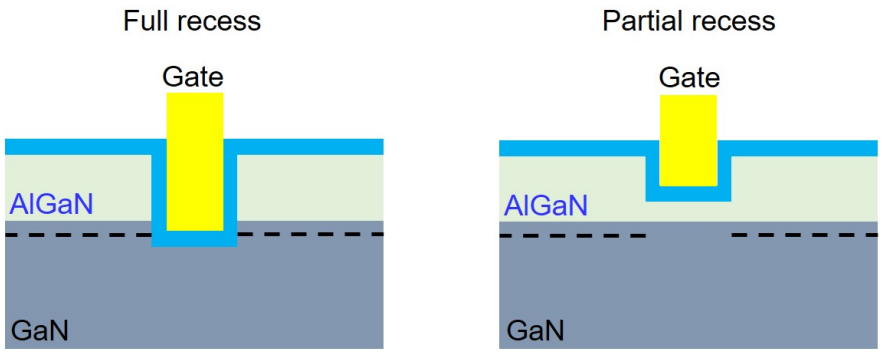

Figure 1.13: Schematic diagram for the full gate recess (left) and partial gate recess (right).

the gate recess method, in which the device layer under the gate electrode is etched in order to deplete the 2DEG, is usually employed. The method is divided intro two cases: one is full recess, etching down to the GaN layer, another is partial recess, etching with a remaining AlGaN layer, which are schematically shown in Fig. 1.13.

For the full recess method, although high threshold voltage can be obtained, the etching-damaged interface can directly degrade the channel electron transport properties, leading to a high on-resistance and low output currents. On the other hand, the partial recess method is more suitable to obtain normally-off operations with high output currents and a low on-resistance. However, due to the existence of the positive interface fixed charge, the threshold voltages are shifted negatively as illustrated in Fig. 1.14. In the case of fully-recessed Al_2O_3/GaN MIS-FETs, the measured $V_{th} \sim 2$ V in Fig. 1.15(a), which is low in comparison with the theoretical value of 10 V calculated in Fig. 1.15(b), owing to the high-density positive interface charge around the middle of 10^{13} cm^{-2} [51, 56]. In the case of partially-recessed Al_2O_3/AlGaN/GaN MIS-FETs, a thin remaining AlGaN layer $\lesssim 2$ nm is often required owing to such a high-density positive interface fixed charge [66]. Such a thin-remaining AlGaN layer can also have the transport properties degraded by scattering due to the interface. Therefore, if the interface charge engineering succeeds to suppress the positive interface fixed charge, we can realize normally-off devices using partial gate recess with a thicker remaining AlGaN layer, exhibiting

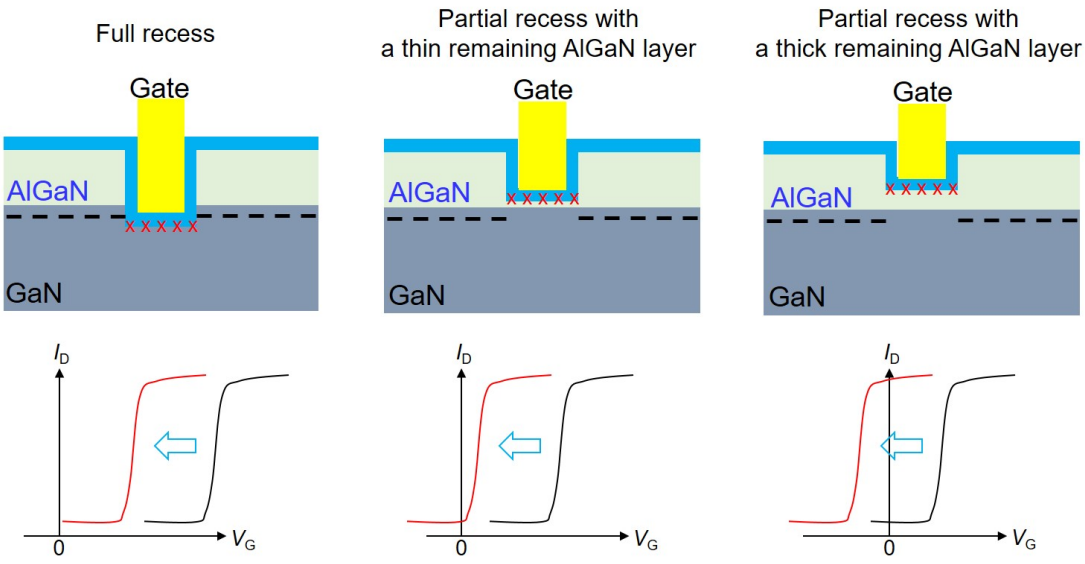

Figure 1.14: The interface fixed charge can shift the threshold voltage negatively, from high values to low values, or even to negative values in case of partial recess with a thick remaining AlGaN thickness.

good electron transport properties.

On the other hand, electrical noise is fundamental problem in science and engineering, because noise directly affects the device/instrument performances by

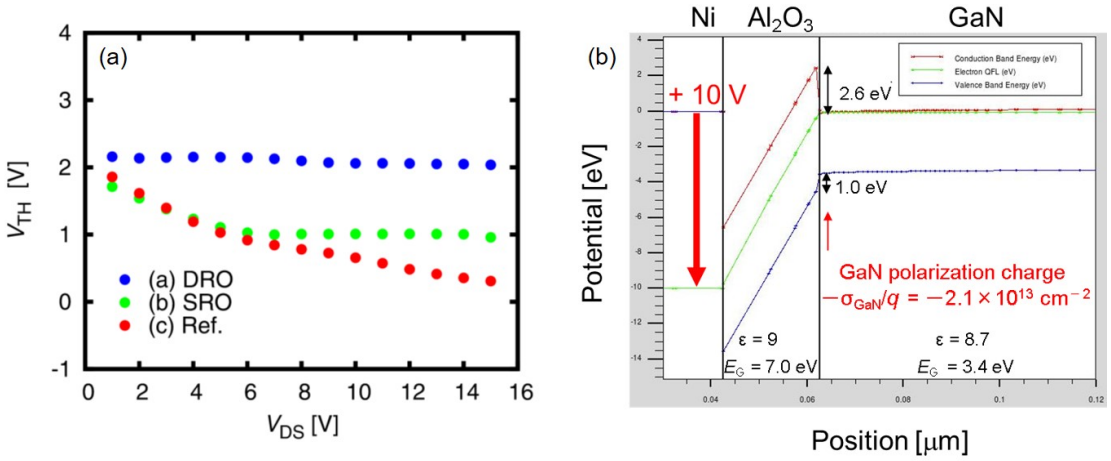

Figure 1.15: (a) Threshold voltages of fully-gate-recessed Al_2O_3/GaN MIS-FETs. (b) Theoretical band diagram of the MIS-FETs, showing a threshold voltage of 10 V [67].

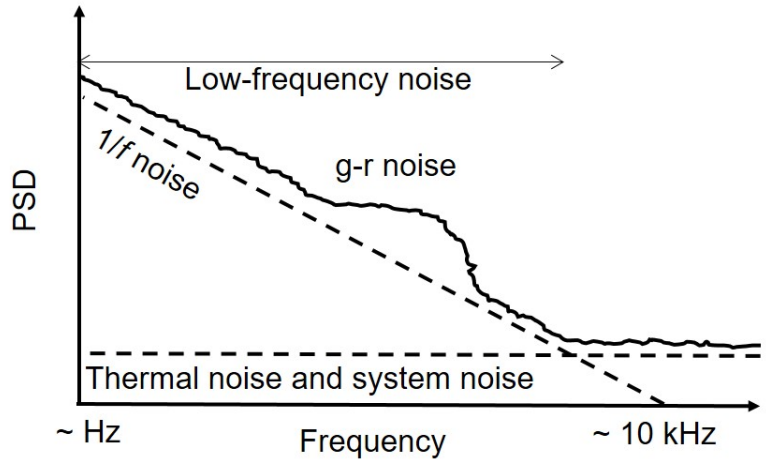

Figure 1.16: Noise power spectral density (PSD) as a function of the frequency f.

limiting the measurement accuracy and the magnitude of detectable signals. In particular, the device noise characteristics are strongly influenced by the semiconductor materials themselves, and also their interfaces. Midgap deep levels including interface deep levels can trap/detrap electrons, leading to fluctuation in the carrier-number and also the mobility. These fluctuations give the noise to the signals (current or voltage) in the devices. Depending on the frequency f, noise can be classified as thermal noise whose power spectral density (PSD) is independent of f, generation-recombination (g-r) noise which is bumpy at specific frequencies, and $1/f$ noise whose PSD is inversely proportional to the frequency. These types are illustrated in Fig. 1.16. Low-frequency noise is the noise at low frequencies, usually below 10 kHz. In this range, g-r noise and $1/f$ noise dominate the PSD. The $1/f$ noise PSD always increases with a decrease in the frequency, thus it becomes the most significant noise source at very low frequencies. On the other hand, the g-r noise bumps caused by midgap deep levels with specific time constants can interfere with the device operations. Moreover, the signal-to-noise ratio (SNR), which indicates the reliability of the signal processing of a device (the higher the ratio, the better the signal), becomes smaller when the device size reduces [68], hence the low-frequency noise becomes a major concern for nano-device technologies. Therefore, understanding and overcoming the low-frequency noise problems are important for the future of electronic devices and circuits.

In AlGaN/GaN MIS-FETs, there are imperfections such as threading dislocations, bulk deep levels, and interface deep levels, in particular at insulator-semiconductor interface. These imperfections can cause electron scattering and electron trapping/detrapping, which can influence the low-frequency noise. Moreover, in gate-recessed AlGaN/GaN MIS-FETs, the insulator/etched-(Al)GaN interface and the insulator near to the 2DEG channel can lead to electron scattering, degrading the channel electron mobility. Furthermore, the deep levels can trap/detrap electrons from the 2DEG, causing current fluctuations. These effects can enhance the low-frequency noise, limiting the device applications. Therefore, understanding the low-frequency noise in gate-recessed AlGaN/GaN MIS-FETs can help improving the device performances.

1.3 Purpose of this study

Aluminum titanium oxide Al_xTi_yO (AlTiO), an alloy of Al_2O_3 and TiO_2, is an useful insulator because its physical properties can be controlled by controlling its composition. In this study, for AlTiO/AlGaN/GaN MIS devices, we systematically investigated the positive interface fixed charge depending on the composition of AlTiO obtained by atomic layer deposition. We evaluated the positive interface fixed charge density from the insulator-thickness dependence of the threshold voltages of the MIS devices and found that interface charge engineering, i.e. the ability to control the threshold voltages by controlling the positive interface charge density, using AlTiO gate insulator is possible for GaN-based MIS devices. Moreover, we combined interface charge engineering using AlTiO gate insulator with a partial gate recess method for AlGaN/GaN MIS-FETs and successfully obtained normally-off operations with a high threshold voltage and good transport properties. In addition, employing X-ray photoelectron spectroscopy and low-frequency noise characterization, we looked for physical insights at AlTiO/AlGaN interface.

1.4 Organization of the dissertation

This dissertation includes four chapters. The content of each chapter is summarized as follows.

Chapter 1 is the introduction to this research, which introduces the general background on compound semiconductors, the GaN-based semiconductors and related devices, the interface charge engineering, and the purpose of this study.

Chapter 2 is the investigation of the interface charge engineering in non-recessed AlTiO/AlGaN/GaN MIS devices. We show the fabrication process of the MIS devices and evaluate the positive fixed charge density at AlTiO/AlGaN interface depending on AlTiO composition. Furthermore, we look for the relation between the positive fixed charge and the bonding states of the metals at the AlTiO/AlGaN interface by employing X-ray photoelectron spectroscopy.

Chapter 3 is the investigation of the interface charge engineering in partially-gate-recessed AlTiO/AlGaN/GaN MIS devices with a rather thick remaining AlGaN layer. As a result, we obtained a normally-off MIS-FETs with good device performances.

Chapter 4 is the investigation of the low-frequency noise in non-recessed and partially-recessed AlTiO/AlGaN/GaN MIS devices. We found two trap levels in AlTiO insulators which is independent of AlGaN thickness. Furthermore, a decrease in the remaining AlGaN thickness leads to an increase in the noise magnitude.

Chapter 5 concludes this work and discusses the future perspective of the work.

Chapter 2

Interface charge engineering in non-recessed AlGaN/GaN MIS devices using AlTiO insulators

It has been reported that for AlGaN/GaN MIS devices, employing Al_xTi_yO (AlTiO) gate insulators with a composition of $x/(x+y) = 0.73$ leads to a suppressed positive interface fixed charge density in comparison with Al_2O_3 gate insulators [69]. The result indicates that AlTiO can be applied for interface charge engineering since its physical properties can be controlled via its composition. Therefore, in this chapter, for non-recessed AlGaN/GaN MIS devices, we investigate interface charge engineering using AlTiO insulators by systematically evaluating the insulator-semiconductor interface fixed charge density depending on the composition of AlTiO obtained by atomic layer deposition (ALD).

2.1 Properties of AlTiO deposited by ALD

Figure 2.1 shows the relation between band gap E_g and dielectric constant k for several insulators, which exhibits a trade-off (the dashed line) between E_g and k. For examples, Al_2O_3 has a large E_g ($\simeq$ 6.8 eV), but not so high k ($\simeq$ 9); on the other hand, TiO_2 has a very high k ($\simeq$ 60), but small E_g ($\simeq$ 3 eV). For a gate

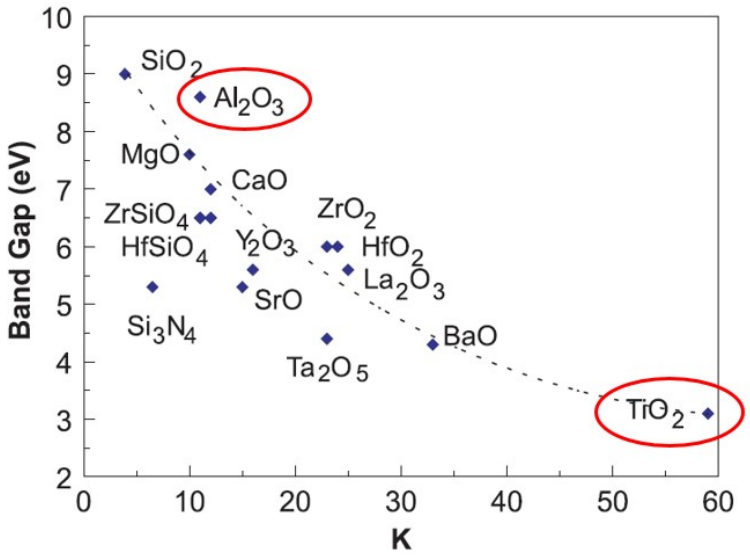

Figure 2.1: Band gap versus dielectric constant k for several insulators.

insulator, it is desirable to have both high k and large E_g. Therefore, AlTiO (aluminum titanium oxide) [69–73], an alloy of Al_2O_3 and TiO_2, can have immediate properties between them, which is useful not only for energy gap engineering and dielectric constant engineering, but also for balancing k and E_g. Furthermore, many other properties of AlTiO can be controlled by controlling it composition, as shown in Fig 2.2.

The AlTiO gate insulators are deposited by ALD. The precursors are trimethyl

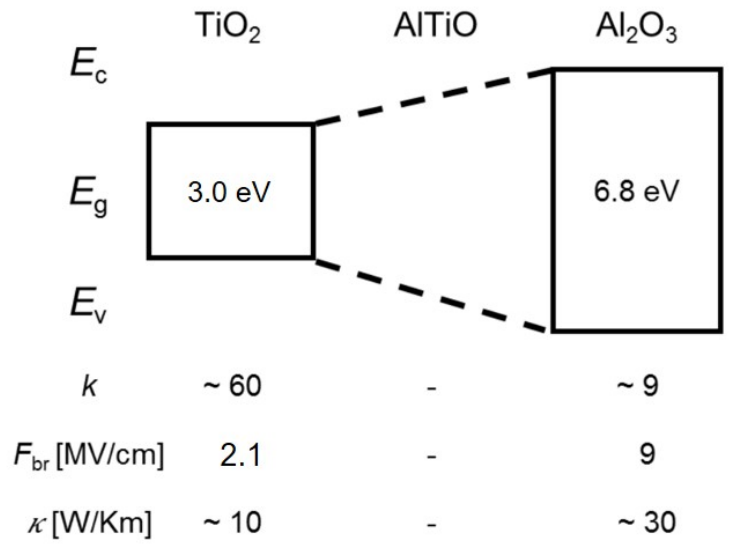

Figure 2.2: Properties of AlTiO can be controlled between TiO_2 and Al_2O_3.

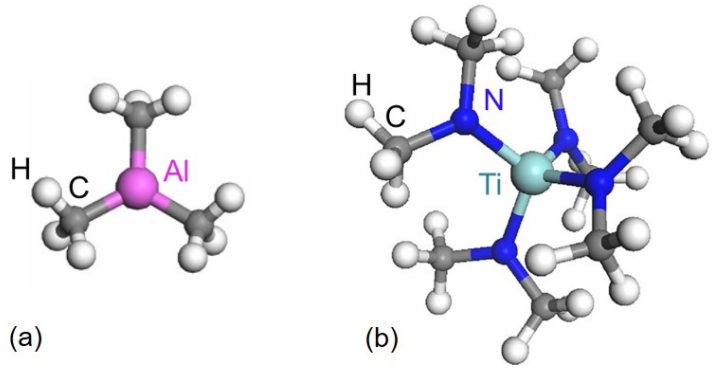

Figure 2.3: Chemical structures of (a) TMA and (b) TDMAT [74].

aluminum $Al(CH_3)_3$ (TMA), tetrakis dimethyl amino titanium $Ti[N(CH_3)_2]_4$ (TDMAT) and water H_2O. Figure 2.3 shows the chemical structure of the two precursors. The reactions between the precursors are

$$2Al(CH_3)_3 + 3H_2O \rightarrow Al_2O_3 + 6CH_4$$
$$Ti[N(CH_3)_2]_4 + 2H_2O \rightarrow TiO_2 + 4N(CH_3)_2H.$$

The deposition of AlTiO is carried out as follows. l-cycle of TMA-H_2O is at first introduced into the ALD chamber, forming a cluster of Al_2O_3 on the semiconductor surface, followed by m-cycle of TDMAT-H_2O, forming TiO_2. This step is defined as one cycle-set, as shown in Fig. 2.4. Thus, the AlTiO composition and thickness can be modulated through the (l, m) combinations and the number of cycle-sets, respectively.

It should be noted that the full expression of AlTiO is Al_xTi_yO, not $Al_xTi_{1-x}O$. It is due to the fact that AlTiO is an alloy of Al_2O_3 and TiO_2, so we can express AlTiO as $(Al_2O_3)_x(TiO_2)_y$, or $Al_{2x}Ti_yO_{3x+2y}$. We can see that the sum of the number of Al atoms and Ti atoms is not equal to the number of O atoms. In order to estimate the composition of Al_xTi_yO, we employed X-ray photoelectron spectroscopy (XPS). Figure 2.5(a) shows XPS spectra of Al_xTi_yO films with dif-

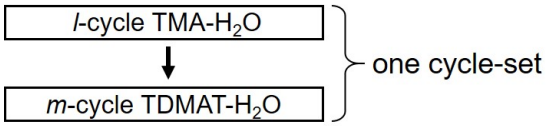

Figure 2.4: Deposition procedure for AlTiO.

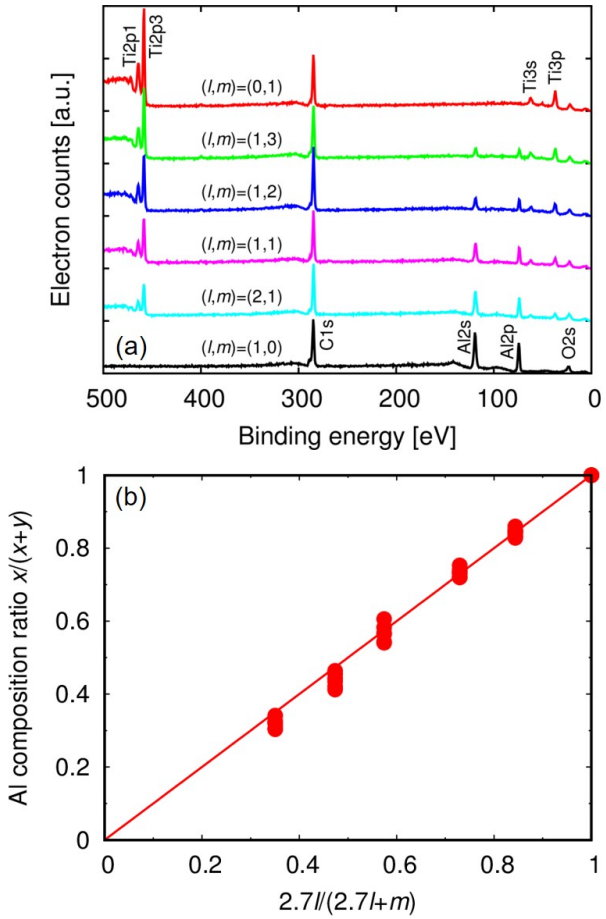

Figure 2.5: (a) XPS spectra of Al_xTi_yO thin films with different combinations of (l, m). (b) Relation between the composition $x/(x + y)$ and (l, m), showing a linear relation.

ferent combinations of (l, m). From the data, the peak intensity ratio between (Al2s, Al2p) and (Ti2p, Ti3s, Ti3p) are calculated and plotted in Fig. 2.5(b). The graph shows a linear relation between Al composition ratio $x/(x + y)$ and $2.7l/(m + 2.7l)$, giving the expression of the composition based on (l, m) to be $x/y \simeq 2.7l/m$. From here on, the Al composition ratio $x/(x + y)$ will be referred as the AlTiO composition.

The thickness and refractive index at 630 nm of AlTiO films are measured by ellipsometry, which are shown in Fig 2.6(a) and (b), respectively. The AlTiO refractive index systematically changes depending on the composition as expected. We obtain a stable deposition rate for each AlTiO composition, which is summarized in Table 2.1. From the deposition rate of Al_2O_3 and TiO_2, we determine that 0.3 monolayers and 0.2 monolayers are deposited for $l = 1$ and $m = 1$, re-

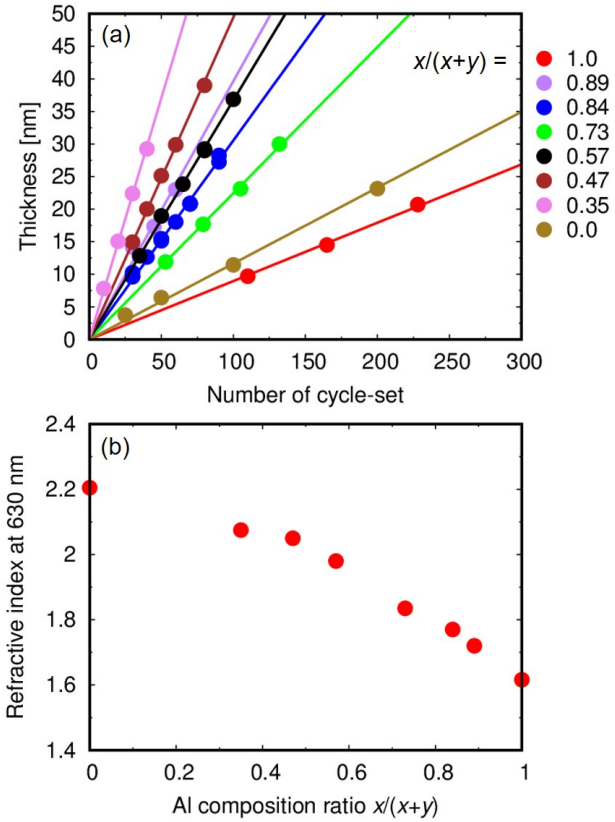

Figure 2.6: (a) The thickness and (b) the refractive index at 630 nm of AlTiO films obtained by ellipsometry.

spectively. Therefore, with these combinations of (l, m), less than 1 monolayer is deposited per cycle-set, so the insulator is an alloy, not a super-lattice structure.

Table 2.1: Deposition rate for each AlTiO composition.

$(l,\ m)$	$x/(x+y)$	Deposition rate [nm/cycle-set]
(1, 0)	1.0	0.09
(3, 1)	0.89	0.40
(2, 1)	0.84	0.31
(1, 1)	0.73	0.22
(1, 2)	0.57	0.37
(1, 3)	0.47	0.49
(1, 5)	0.35	0.74
(0, 1)	0.0	0.13

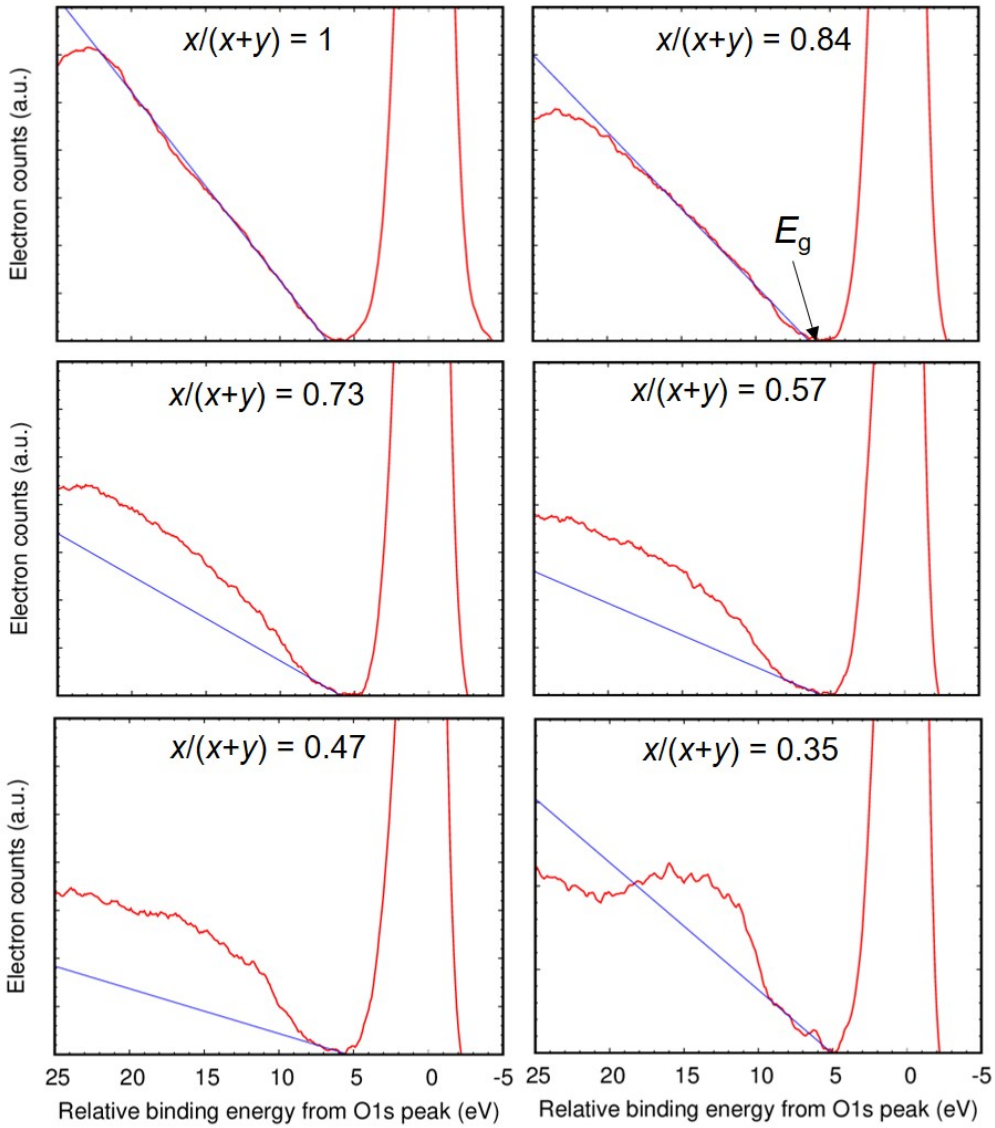

Figure 2.7: XPS O1s EELS spectra for each AlTiO composition.

In order to estimate the energy gap, we employed electron energy loss spectroscopy (EELS). Figure 2.7 shows the EELS spectra plotted as functions of the relative binding energy to the O1s peak. The estimated E_g as a function of the AlTiO composition is shown in Fig. 2.8. As expected, E_g systematically decreases with a decrease in the composition. For $x/(x+y) = 0.35$ composition, $E_g \simeq 5$ eV, close to the energy gap of AlGaN (4.2 eV), which may not enough for a gate insulator. We consider that AlTiO with even smaller composition is not suitable for a gate insulator.

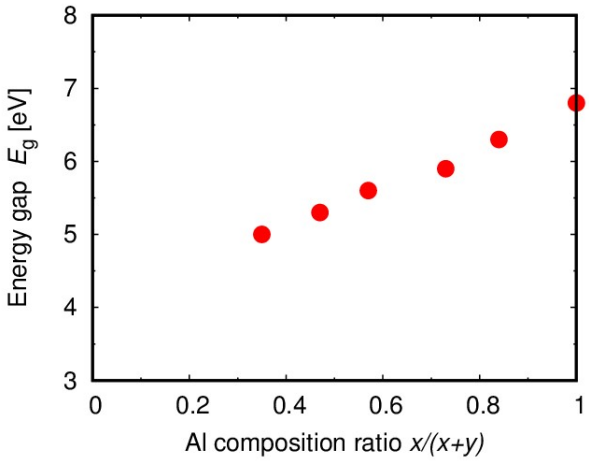

Figure 2.8: E_g obtained by EELS as a function of the composition.

2.2 AlTiO/AlGaN/GaN MIS device fabrication process

In order to investigate the positive fixed charge at AlTiO/AlGaN interface, we fabricated AlTiO/AlGaN/GaN MIS-capacitors. The fabrication process started from an $Al_{0.24}Ga_{0.76}N$ (20 nm)/GaN (3000 nm) heterostructure grown by metal-organic vapor phase epitaxy on sapphire(0001), whose schematics is shown in Fig 2.9. The electrical properties of the heterostructure are: the sheet resistance of 580 Ω/□, electron sheet concentration of 7.8×10^{12} cm^{-2}, and electron mobility of 1400 cm^2/V·s. The process flow of the MIS-capacitors is shown in Fig. 2.10. First,

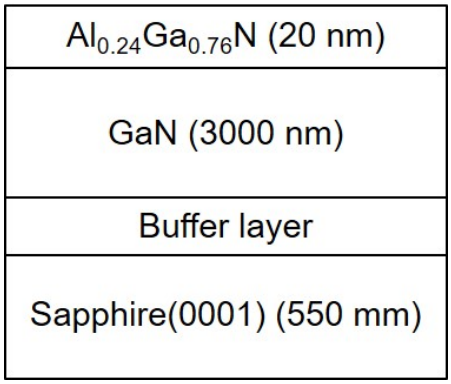

Figure 2.9: The schematics of $Al_{0.24}Ga_{0.76}N$ heterostructure.

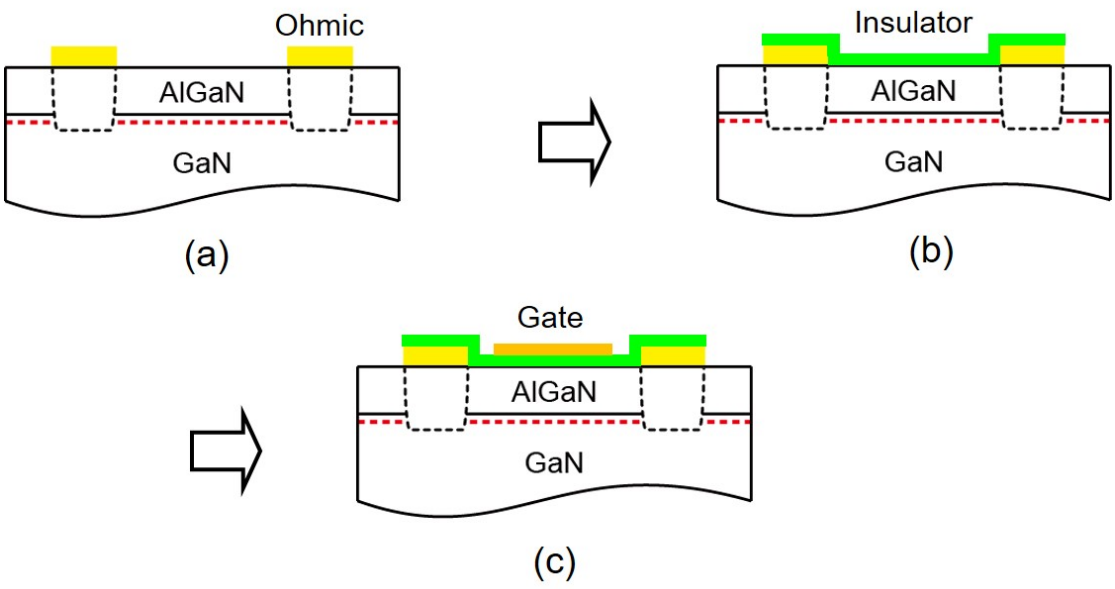

Figure 2.10: Process flow of the MIS-capacitors. (a) Ohmic electrode formation. (b) Insulator deposition. (c) Gate electrode formation.

the Ohmic electrodes were formed on the AlGaN/GaN substrates. Then AlTiO gate insulators were deposited by ALD with several compositions and thicknesses. Finally, gate electrode formation completed the fabrication process. Each process will be discussed in details in the following sections.

Ohmic electrode formation

The process flow of the Ohmic electrode formation is shown in Fig. 2.11. Starting from a 4-inch wafer, 6 × 6 mm rectangular samples were cut. Then wet surface treatment was carried out by using organic solutions such as acetone, methanol, and deionized water (DIW) for 3 minutes, followed by O_2 plasma treatment at 50 Pa, 10 W, and 4 minutes to fully remove organic impurities on the sample surface. After that, the samples were put in a semico-clean solution in 5 mintues, which is a dilute solution of tetramethyl ammonium hydroxide (TMAH), or $N(CH_3)_4OH$ to remove oxide layer at the surface, then washed in DIW for 3 minutes.

Before carrying out resist coating process, the samples were baked at 110 °C to

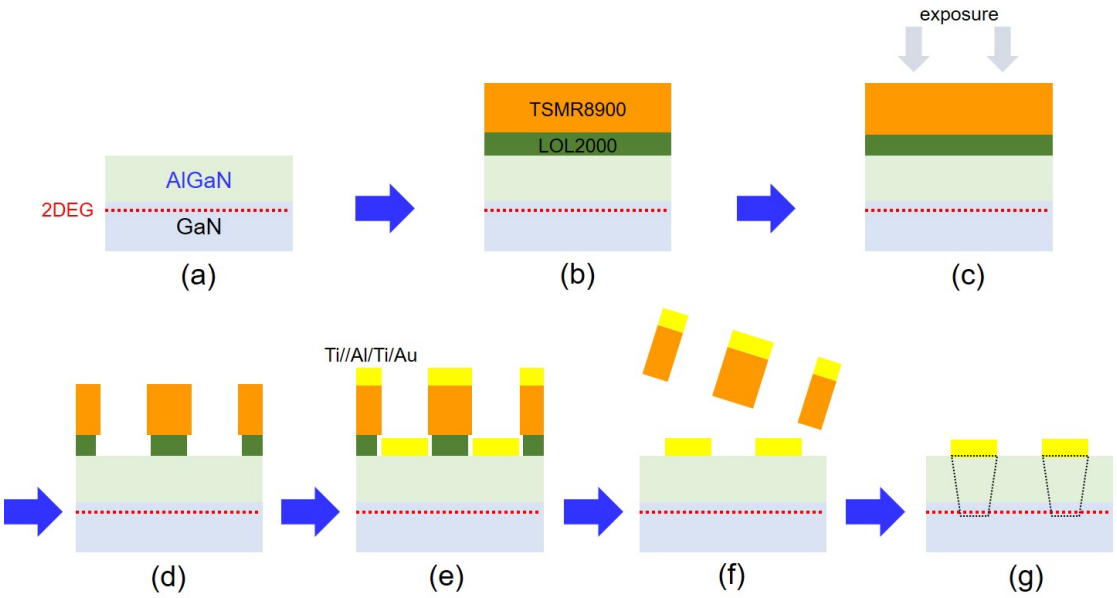

Figure 2.11: Process flow of the Ohmic electrode formation. (a) Surface treatment. (b) Resist coating. (c) Patterning. (d) Development. (e) Metal deposition. (f) Lift-off. (g) Annealing.

remove remaining water. Lift-off resist LOL2000 was coated at 3000 revolutions per minute (rpm) in 60 seconds, which gives a thickness of 0.2 μm, followed by a 180-second baking at 180 °C to harden the resist layer. After that, positive resist TSMR-8900 was coated at 4000 rpm in 60 seconds, which gives a thickness of 1 μm, and baked at 110 °C in 90 seconds.

Next, the coated samples were exposed to laser light using maskless aligner (MLA). The laser wavelength is 405 nm with a power of 140 mJ/cm^2. Then the samples were developed in TMAH for 50 seconds, and washed in DIW for 3 minutes. Again the samples were treated by O_2 plasma at 50 Pa, 10 W, and 1 minute to remove remaining resist, followed semico-clean solutions in 5 minutes to remove oxide layer formed after long time exposure in the air.

The coated samples were then put inside resistance heating evaporator (RHE) chamber. After 4 hours vacuuming, the pressure was at the low of 10^{-4} Pa. Then Ti/Al/Ti/Au metals were deposited with the thickness of 5/100/200/50 nm.

After metal deposition, the samples were dipped in a resist remover, 1-methyl-

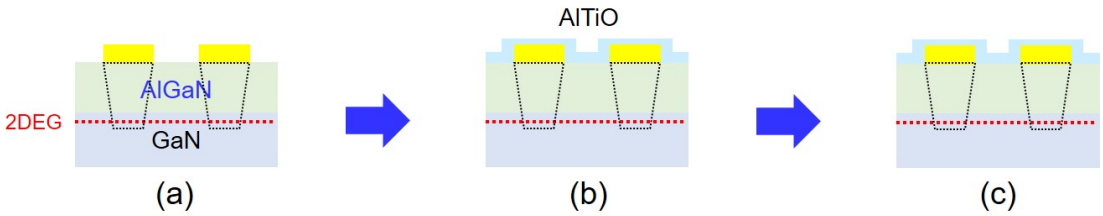

Figure 2.12: Process flow of the insulator deposition. (a) Surface treatment. (b) Insulator deposition. (c) Post-deposition annealing.

2-pyrrolidinone-based solution (commercial name: 1165), at 60 °C in 15 minutes. After removing the unnecessary metal parts, the samples were cleaned by wet surface treatment.

The last process was annealing in N_2 atmosphere at 575 °C for 5 minutes to make the Ohmic contact between metal and semiconductor.

Insulator deposition

The process flow of insulator deposition is shown in Fig. 2.12. Before introducing into ALD chamber, the samples were cleaned with the similar surface treatment as in the Ohmic formation process. To determine the insulator's thickness and refractive index, GaAs reference samples were put together. The Al_xTi_yO insulators with several compositions and thicknesses were then deposited. After that, post-deposition annealing in H_2-mixed (10%) Ar atmosphere at 350 °C for 30 minutes was carried out.

Gate formation

The process flow of the gate formation is shown in Fig. 2.13. Same surface treatment for the samples was carried out before resist coating process. Because TMAH can dissolve AlTiO, semico-clean treatment was omitted. For resist coating, addition layer is needed to protect AlTiO films from development process. Thus, we employed electron beam resist GL2000, which cannot be dissolved by TMAH. The resist GL2000-M was coated at 4000 rpm in 60 seconds, which gives 0.3 μm,

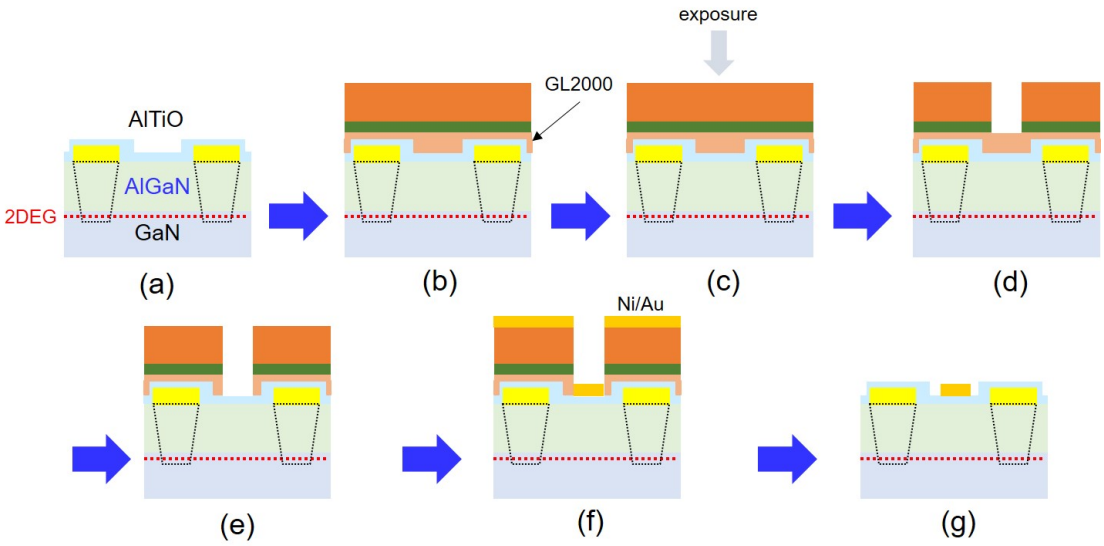

Figure 2.13: Process flow of the gate formation. (a) Surface treatment. (b) Resist coating. (c) Patterning. (d) Development. (e) O_2 plasma treatment. (f) Gate metal deposition. (g) Lift-off.

followed by a baking at 180 °C in 180 seconds. The lift-off resist LOL2000 and positive photoresist TSRM8900 were coated similarly in the Ohmic process.

After exposure by MLA and development by TMAH with the same condition, only GL2000 was left at the exposed area as shown in Fig. 2.13(d). To remove the resist, O_2 plasma treatment was employed at 30 Pa, 20 W, 6 minutes. The samples was then loaded into RHE chamber. The gate metal Ni/Au with the thickness of 5/100 nm was deposited.

Due to the additional layer of electron beam resist, the samples were kept in the resist remover solution for longer time, about 1 hour, to fully dissolve all the resists. Finally, surface treatment was carried out in acetone, methanol, and DIW in 3 minutes to complete the process. We successfully fabricated Al_xTi_yO/AlGaN/GaN MIS-capacitors whose schematics and top view are shown in Fig. 2.14. In this chapter, we employed eight compositions of Al_xTi_yO: $x/(x+y) = 1.0$, 0.89, 0.84, 0.73, 0.57, 0.47, 0.35, and 0.0.

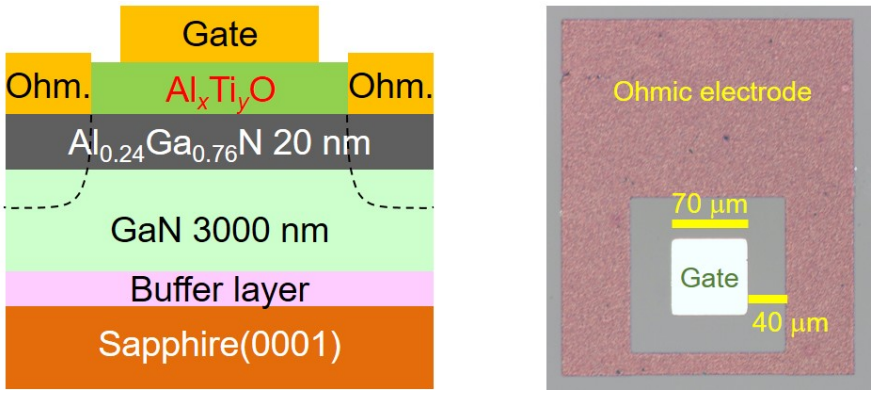

Figure 2.14: The schematics (the left image) and top view (the right one) of the Al_xTi_yO/AlGaN/GaN MIS-capacitors.

2.3 AlTiO/AlGaN/GaN MIS device characterization

2.3.1 Electrical characterization

Figure 2.15 shows the I-V_G characteristics of the Al_xTi_yO/AlGaN/GaN MIS-capacitors for each composition and insulator thickness. As expected, except for $x/(x+y) = 1.0$ composition, Al_2O_3 case, the leakage currents at the negative bias are almost at the same order with 0.0 composition, TiO_2 case. On the other hand, the leakage currents at the positive bias increase as the composition decreases, owing to the fact that the energy gap of AlTiO also decreases with the decrease in the composition.

Figure 2.16 shows the C-V_G characteristics of the Al_xTi_yO/AlGaN/GaN MIS-capacitors for each composition and insulator thickness. The gate voltage sweep is from 0 to -10 V under the frequency of 1 MHz with a sweep rate of 0.36 V/s. By integrating C as a function of V_G, we obtain the sheet concentration of the 2DEG n_s under the gate as shown in Fig. 2.17, from which the threshold voltage V_{th} can be determined at $n_s = 0$ by linear fitting of n_s-V_G relation.

Figure 2.18 shows the theoretical band diagram of Al_xTi_yO/AlGaN/GaN MIS-capacitors, assuming the positive interface charge. From this, we obtain

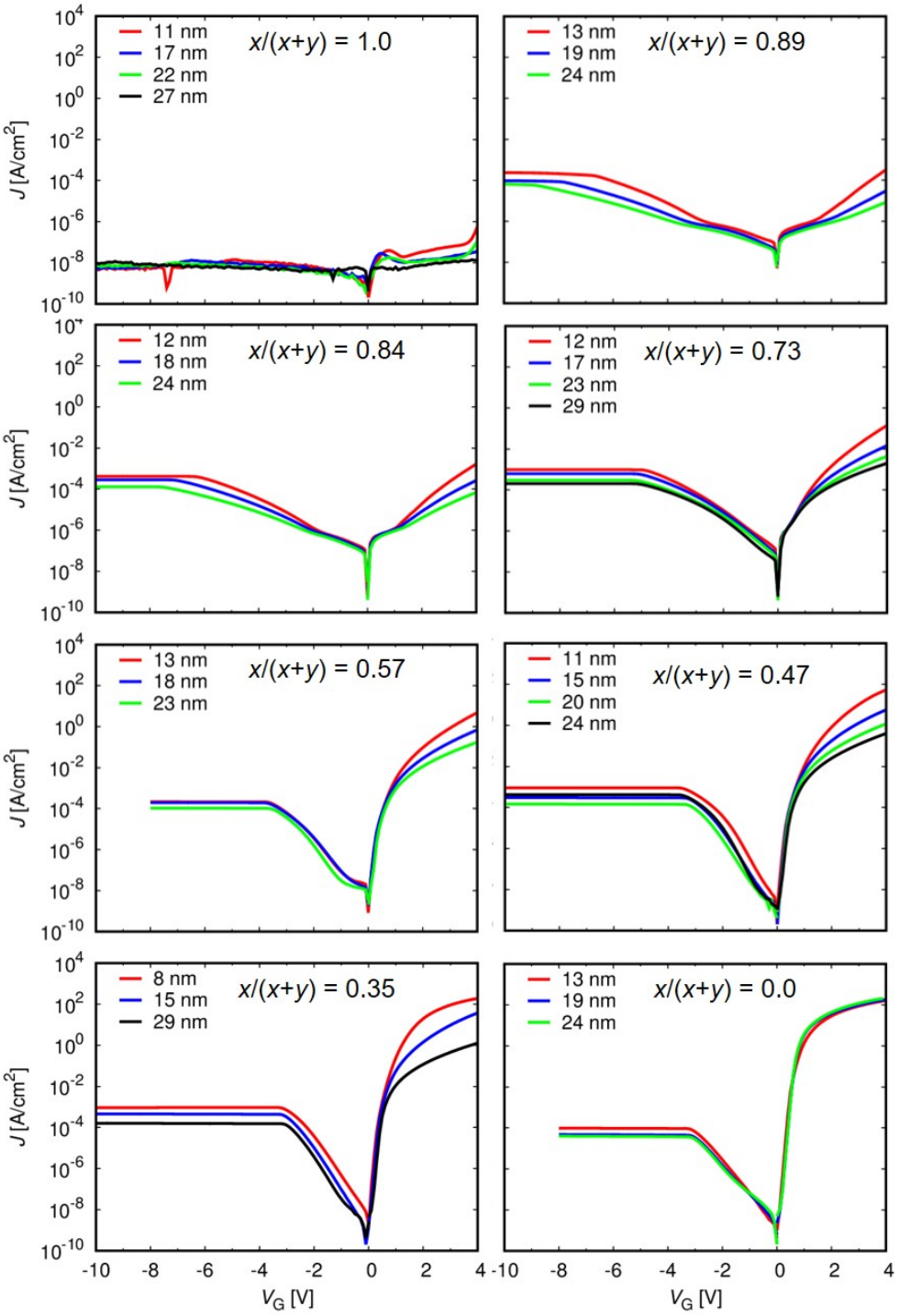

Figure 2.15: I-V_{G} characteristics of the $\mathrm{Al}_x\mathrm{Ti}_y\mathrm{O}$/AlGaN/GaN MIS-capacitors for each composition and insulator thickness.

$$\begin{aligned}
&\frac{\sigma_{\mathrm{ins}} - \sigma_{\mathrm{GaN}} - qn_{\mathrm{s}}}{k_{\mathrm{ins}}\varepsilon_0} d_{\mathrm{ins}} + \frac{\sigma_{\mathrm{AlGaN}} - \sigma_{\mathrm{GaN}} - qn_{\mathrm{s}}}{k_{\mathrm{AlGaN}}\varepsilon_0} d_{\mathrm{AlGaN}} \\
&= \frac{\phi - \varphi - \Delta E_{\mathrm{c}}}{q} + E_{\mathrm{F}}/q - V_{\mathrm{G}} \\
&= \psi/q + E_{\mathrm{F}}/q - V_{\mathrm{G}},
\end{aligned} \tag{2.1}$$

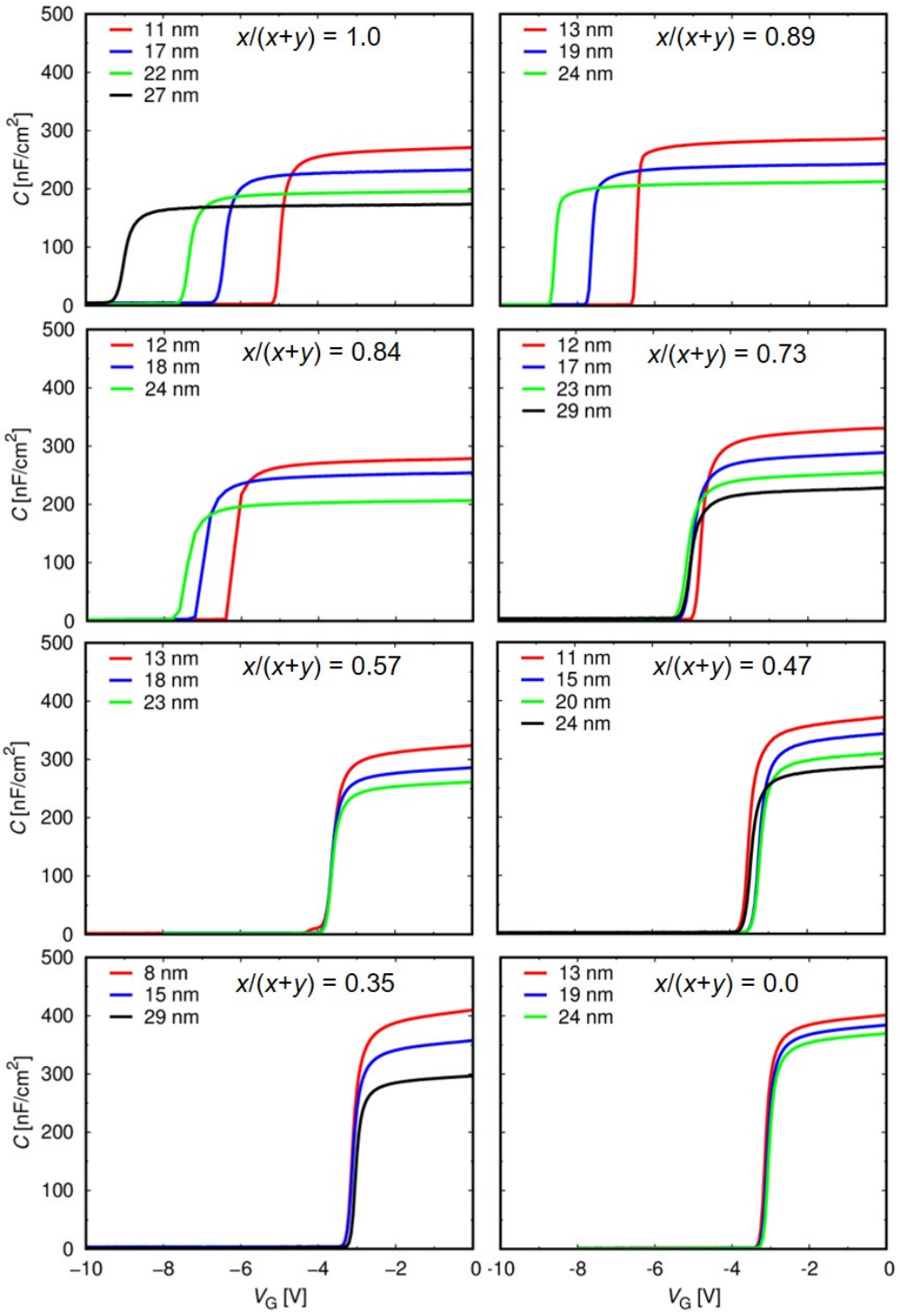

Figure 2.16: C-V_{G} characteristics of the $\mathrm{Al}_x\mathrm{Ti}_y\mathrm{O}$/AlGaN/GaN MIS-capacitors for each composition and insulator thickness.

using the elementary charge $q > 0$, the vacuum permittivity ϵ_0, the dielectric constants k_{ins} and k_{AlGaN}, the metal-AlTiO barrier height ϕ, the AlTiO-AlGaN conduction band offset φ, the AlGaN-GaN conduction band offset ΔE_{c}, the positive

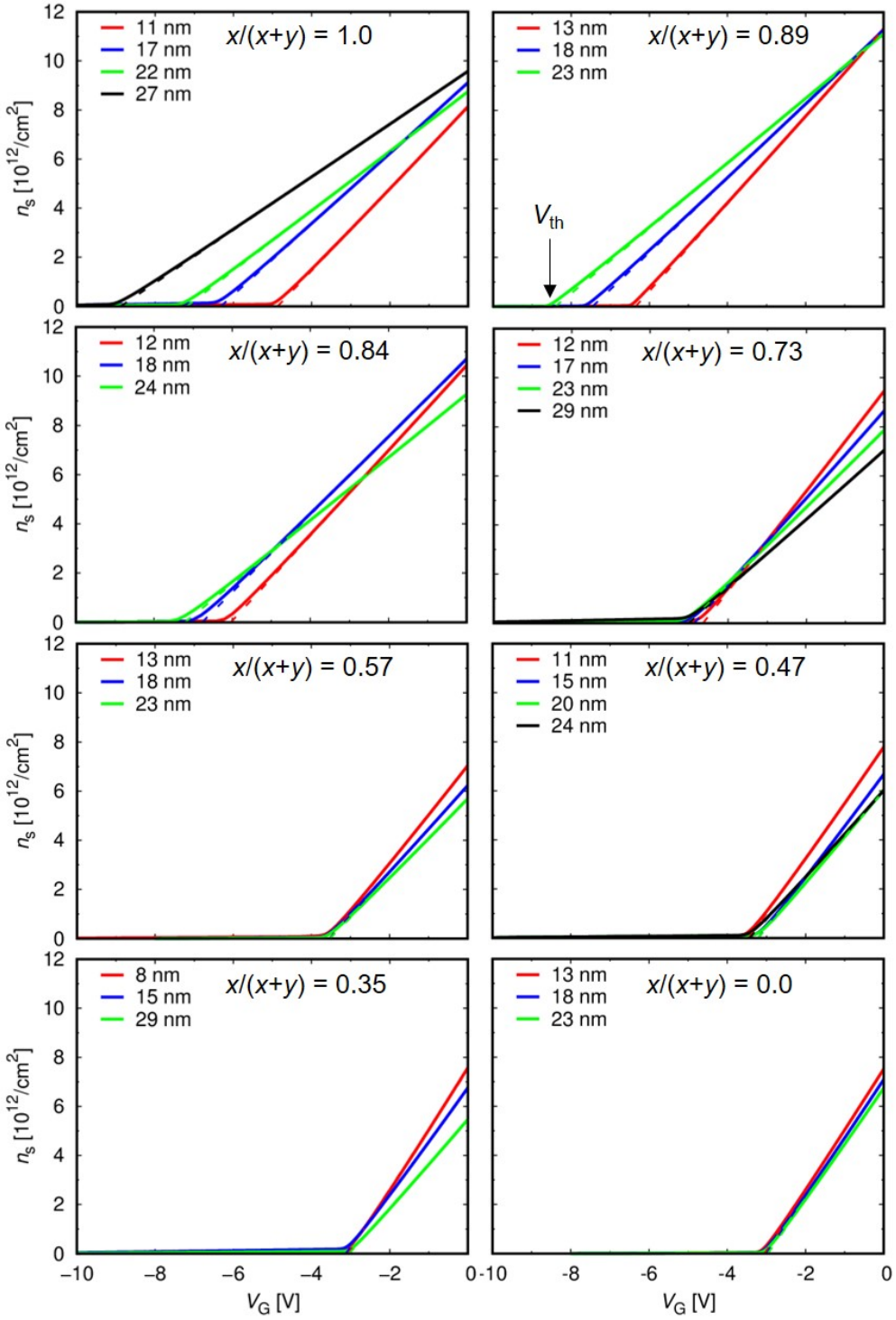

Figure 2.17: n_s-V_G characteristics of the Al_xTi_yO/AlGaN/GaN MIS-capacitors for each composition and insulator thickness.

interface fixed charge density σ_{ins}, the AlGaN polarization charge density σ_{AlGaN}, the GaN polarization charge density σ_{GaN}, and the 2DEG Fermi energy E_F de-

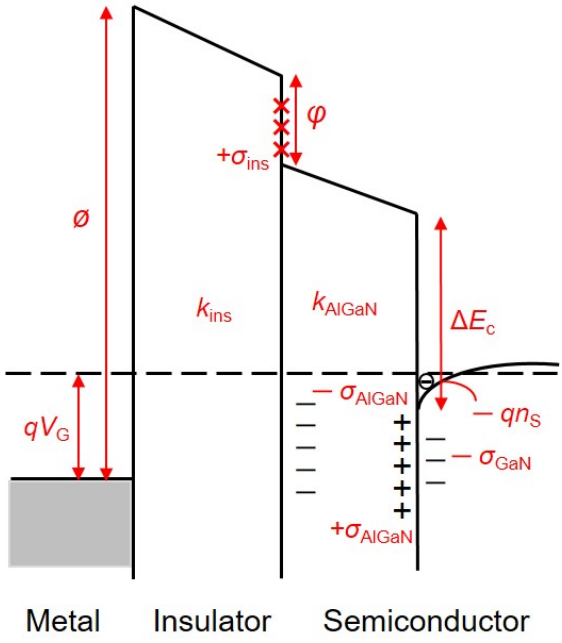

Figure 2.18: Theoretical band diagram of the Al_xTi_yO/AlGaN/GaN MIS-capacitors.

fined in Fig. 2.18. These equations are derived in Appendix A. Using Eq. (2.1), the measurement results can be analyzed.

The capacitance C is calculated by $1/C = \partial V_G/\partial n_s$. From Eq. (2.1), taking differential of both sides with respect to n_s, we obtained the capacitance C_0 at zero bias, i.e. $V_G = 0$ V:

$$\frac{1}{C_0} = \frac{d_{ins}}{k_{ins}\epsilon_0} + \frac{d_{AlGaN}}{k_{AlGaN}\epsilon_0}. \tag{2.2}$$

Figure 2.19(a) shows the measured $1/C_0$ as functions of d_{ins}, showing the linear relation (2.2). From the fittings, we estimated dielectric constants $k_{AlGaN} \simeq 10$, and k_{ins} depending on the AlTiO composition which is summarized in Fig. 2.19(b). As expected, k_{ins} increases with a decrease in the Al composition ratio, i.e. with a increase in the Ti composition ratio, since the dielectric constant of Al_2O_3 is smaller than that of TiO_2. Figure 2.20 shows the correlation between E_g and k for the obtained AlTiO insulators, illustrating the trade-off. This behavior confirms that we can control AlTiO insulator properties by controlling its composition, which is useful to balance E_g and k.

At the threshold voltage $V_G = V_{th}$, since $n_s = 0$ and $E_F = 0$, the relation (2.1)

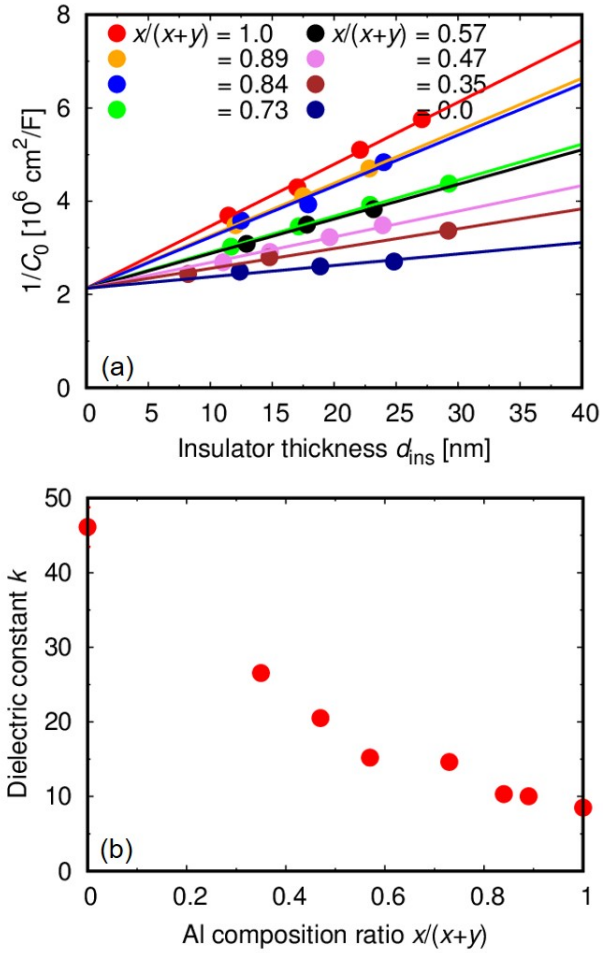

Figure 2.19: (a)$1/C_0$ as linear functions of $d_{\rm ins}$ with fitting lines. (b) The dielectric constant $k_{\rm ins}$ of $\mathrm{Al}_x\mathrm{Ti}_y\mathrm{O}$ depending on the composition $x/(x+y)$.

gives

$$V_{\rm th} = -\frac{\Delta\sigma_{\rm ins}}{k_{\rm ins}\epsilon_0}d_{\rm ins} - \frac{\Delta\sigma_{\rm AlGaN}}{k_{\rm AlGaN}\epsilon_0}d_{\rm AlGaN} + \psi/q, \tag{2.3}$$

where $\Delta\sigma_{\rm ins} = \sigma_{\rm ins} - \sigma_{\rm GaN}$ and $\Delta\sigma_{\rm AlGaN} = \sigma_{\rm AlGaN} - \sigma_{\rm GaN}$. Since $V_{\rm th}$ is a linear function of $d_{\rm ins}$ with a slope of $-\Delta\sigma_{\rm ins}/(k_{\rm ins}\epsilon_0)$, $\Delta\sigma_{\rm ins}$ can be evaluated by the slope of $V_{\rm th}$-$d_{\rm ins}$ relation. Figure 2.21 depicts the measured $V_{\rm th}$ as functions of $d_{\rm ins}$, showing the linear relation (2.3), which indicates that $V_{\rm th}$ is dominated by the positive interface fixed charge (the bulk charge in AlTiO has insignificant effect). We find a trend that, as the AlTiO composition decreases, the slope of $V_{\rm th}$-$d_{\rm ins}$ relation is positively shifted, suggesting that $\Delta\sigma_{\rm ins}$ is reduced, i.e. the positive interface fixed charge density $\sigma_{\rm ins}$ is suppressed. In addition, we observe almost flat $V_{\rm th}$-$d_{\rm ins}$ lines below $x/(x+y) = 0.73$ composition, indicating that the positive

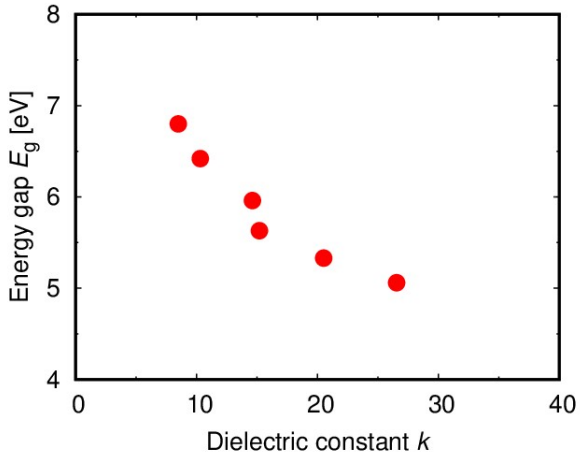

Figure 2.20: Correlation between E_g and k of the AlTiO insulators.

interface charge density is not further suppressed for lower compositions.

From the fitting of V_{th}-d_{ins} using relation (2.3), we obtain $\Delta\sigma_{ins}/q$ as shown in Fig. 2.22(a). Even though $\Delta\sigma_{ins}$ is obtained experimentally, in order to evaluate σ_{ins}, the values of σ_{GaN} and σ_{AlGaN} are required. If we assume $\sigma_{GaN}/q = 2.1 \times 10^{13}$ cm^{-2} and $\sigma_{AlGaN}/q = 3.25 \times 10^{13}$ cm^{-2} for $Al_{0.24}Ga_{0.76}N$ [22, 75–78], we obtain Fig. 2.22(b) plotting σ_{ins} as function of the composition $x/(x+y)$, where the black dotted line corresponds the neutral AlTiO/AlGaN interface. We find a trend that,

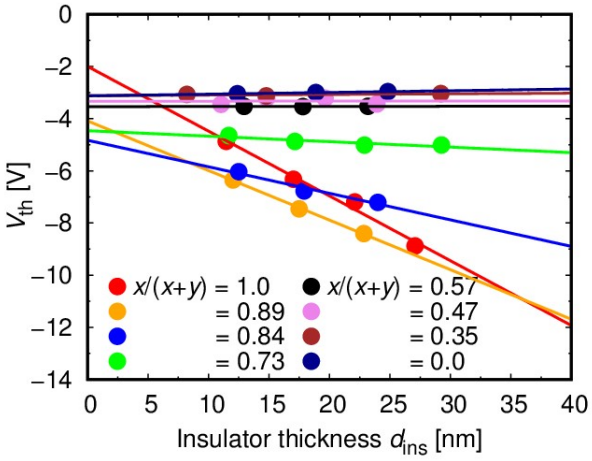

Figure 2.21: V_{th} of the AlTiO/AlGaN/GaN MIS-capacitors as functions of d_{ins} with fitting lines.

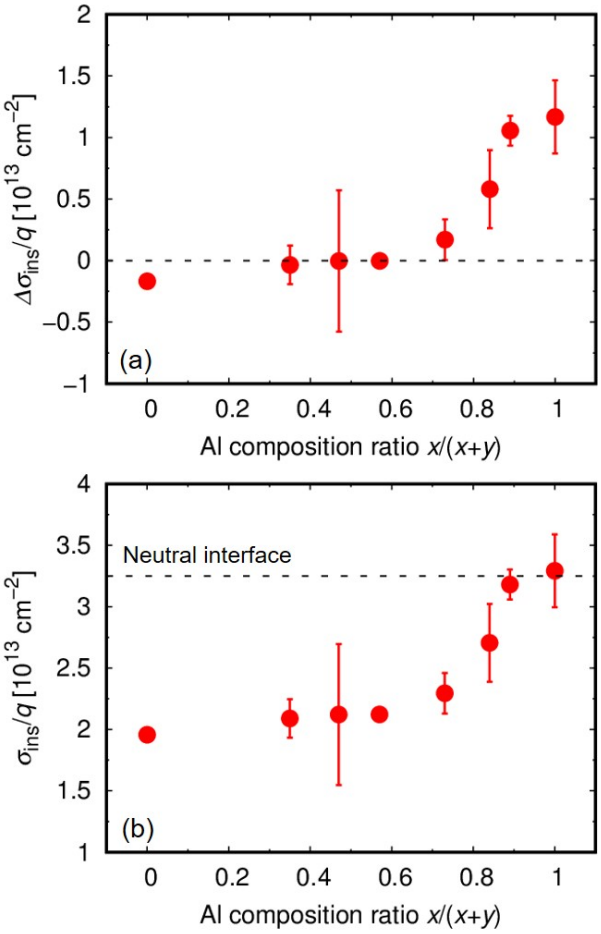

Figure 2.22: (a) $\Delta\sigma_{\mathrm{ins}}$ and (b) the positive interface fixed charge density σ_{ins} depending on the composition $x/(x+y)$. The black dotted line corresponds to the neutral AlTiO/AlGaN interface.

with decrease in the Al composition ratio, i.e. increase in the Ti composition ratio, the positive interface fixed charge density decreases and the AlTiO/AlGaN interface becomes more negatively charged, while the trend is saturated below $x/(x+y) = 0.73$ composition. Moreover, in the previous report, we evaluated σ_{ins} for $Al_{0.27}Ga_{0.73}N$ (7 nm)/ n-$Al_{0.27}Ga_{0.73}N$ (20 nm, Si doping concentration of 2×10^{18} cm^{-3})/ $Al_{0.27}Ga_{0.73}N$ (3 nm)/ GaN (3000 nm) [72] using AlTiO insulators. Interestingly, we find that, for both structures of AlGaN/GaN employing AlTiO with low compositions, although the saturated values of σ_{ins} are different, the saturated values of $\Delta\sigma_{\mathrm{ins}} \simeq 0$, leading to the flat behavior of V_{th}-d_{ins} relation in both cases.

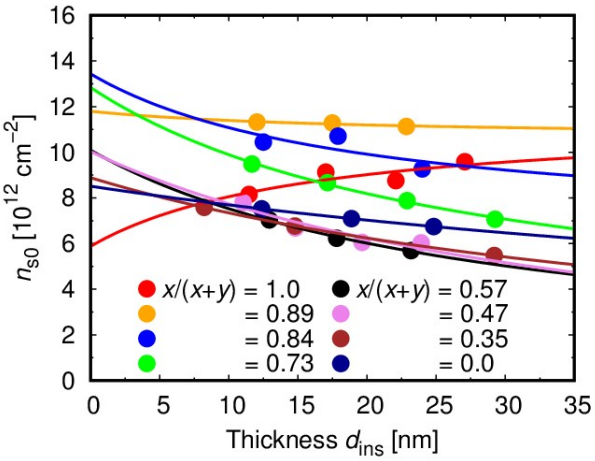

Figure 2.23: n_{s0} of the Al_xTi_yO/AlGaN/GaN MIS-capacitors as functions of d_{ins} with fitting curves.

The 2DEG density at $V_G = 0$ is given by

$$qn_{s0} \simeq \frac{\Delta\sigma_{ins} d_{ins}/(k_{ins}\varepsilon_0) + \Delta\sigma_{AlGaN} d_{AlGaN}/(k_{AlGaN}\varepsilon_0) - \psi/q}{d_{ins}/(k_{ins}\varepsilon_0) + d_{AlGaN}/(k_{AlGaN}\varepsilon_0)}. \tag{2.4}$$

It should be noted that the derivative is given by

$$\frac{\partial n_{s0}}{\partial d_{ins}} \simeq \frac{C_0}{k_{ins}\varepsilon_0}(\Delta\sigma_{ins}/q - n_{s0}), \tag{2.5}$$

whose sign depends on the difference between $\Delta\sigma_{ins}/q$ and n_{s0}. Figure 2.23 depicts the experimental n_{s0}-d_{ins} with fitting curves using relation (2.4). According to (2.5), n_{s0} is an increasing function of d_{ins} for $x/(x+y) = 1.0$, a flat function for 0.89 composition, and a decreasing function for $x/(x+y) \leq 0.84$.

Using the experimental results, we estimated the band diagrams of the Al-TiO/AlGaN/GaN MIS-capacitors using Poisson-Schrödinger calculation. For the calculation, the metal-AlTiO barrier height ϕ and the AlTiO-AlGaN conduction band offset φ are needed. Using the electron affinities ~ 1.9 eV for ALD-deposited Al_2O_3 [79] and ~ 4.0 eV for ALD-deposited TiO_2 [80], we can assume the Al_xTi_yO electron affinity is a linear function of the composition, from which we can derive the AlTiO electron affinity $\sim 4.0 - 2.1x/(x+y)$ eV. If there is no vacuum level discontinuity at the AlTiO/AlGaN, the AlGaN electron affinity ~ 3.5 eV (the GaN electron affinity ~ 4.1 eV) leads to the AlTiO-AlGaN conduction band offset

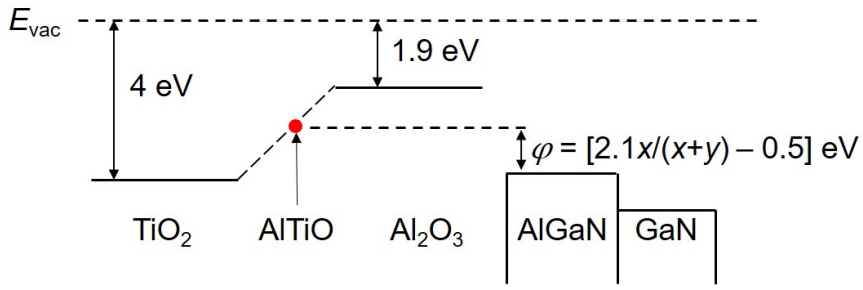

Figure 2.24: AlTiO/AlGaN conduction band offset φ estimated from the electron affinity.

$\varphi \simeq x/(x+y) \times 2.1$ eV $- 0.5$ eV, as shown in Fig. 2.24. Since we experimentally obtained $\phi - \varphi$ from the $V_{\rm th}$-$d_{\rm ins}$ fitting based on (2.3), ϕ can be obtained by using the above φ. The estimated values of the positive interface fixed charge density $\sigma_{\rm ins}$, the metal-AlTiO barrier height ϕ, and the AlTiO-AlGaN conduction band offset φ for each AlTiO composition are summarized in Table 2.2. From these, we obtained the calculated band diagrams shown in Fig. 2.25 for a typical insulator thickness of 20 nm. We find that the suppression in $\sigma_{\rm ins}$ can revert the electric field inside the insulator, shifting the threshold voltage positively. If the positive interface fixed charge can be further suppressed, normally-off operations can be realized.

Table 2.2: Estimated values of $\sigma_{\rm ins}$, ϕ, and φ for each AlTiO composition.

$x/(x+y)$	$\sigma_{\rm ins}/q$ [10^{13} cm^{-2}]	ϕ [eV]	φ [eV]
1.0	3.3	4.6	1.7
0.89	3.2	2.3	1.5
0.84	2.7	1.5	1.4
0.73	2.3	1.6	1.1
0.57	2.1	2.2	0.8
0.47	2.1	2.2	0.6
0.35	2.1	2.1	0.3
0.0	2.0	1.3	-0.5

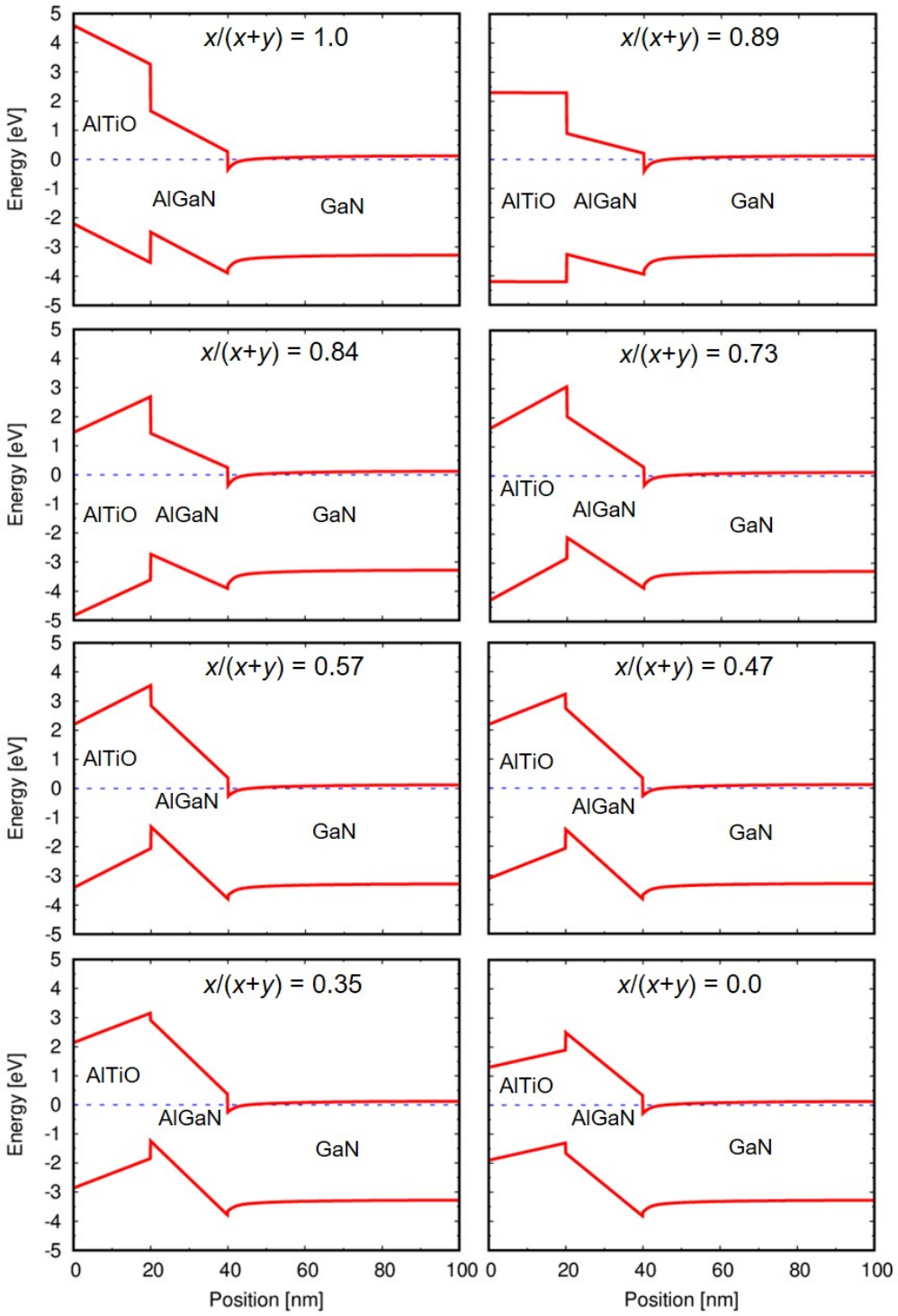

Figure 2.25: The band diagrams of the Al_xTi_yO/AlGaN/GaN MIS-capacitors obtained by Poisson-Schrödinger calculation. The blue-dotted lines indicate Fermi level.

2.3.2 Interface state analysis

The measured positive fixed charge at AlTiO/AlGaN interfaces could be the sum of positive and negative charge, where an electron at the deep interface state

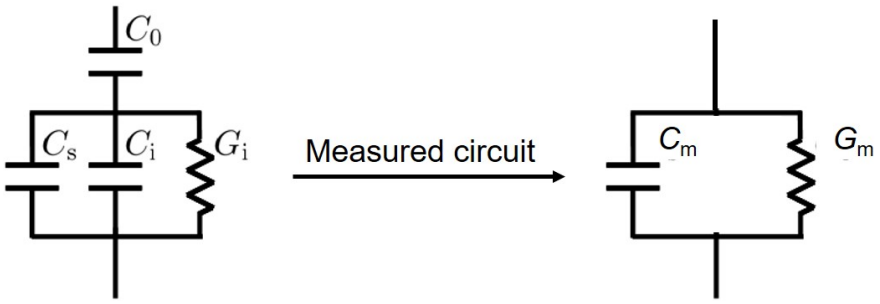

Figure 2.26: (Left) The equivalent circuit of the MIS capacitor. (Right) The measured circuit.

could act as a negative charge due to a very long time constant. Therefore, the difference in the positive interface fixed charge density for each AlTiO composition might come from the difference in the AlTiO/AlGaN interface state density for each composition. In order to investigate the relation, we carried out conductance method to estimate the interface state density at AlTiO/AlGaN interfaces.

Conductance method

The conductance method was carried for the MIS capacitors, whose equivalent circuit is shown in Fig. 2.26(left), where C_0 is the insulator capacitance, C_s is the semiconductor capacitance, G_i is the interface conductance, and C_i is the interface capacitance. When we carry out C-V measurements, the equivalent circuit will be transform into the measured circuit shown in Fig. 2.26(right), where C_m and G_m are the measured capacitance and conductance, respectively. Therefore, we have the total impedance given by

$$\begin{aligned} Z &= \frac{1}{j\omega C_0} + \frac{1}{j\omega C_s + j\omega C_i + G_i} \text{ (equivalent circuit)} \\ &= \frac{1}{j\omega C_m + G_m} \text{ (measured circuit).} \end{aligned} \tag{2.6}$$

Thus,

$$\begin{aligned} \frac{1}{j\omega(C_s + C_i) + G_i} &= \frac{1}{j\omega C_m + G_m} - \frac{1}{j\omega C_0} \\ &= \frac{j\omega(C_0 - C_m) - G_m}{(j\omega C_m + G_m) j\omega C_0}. \end{aligned} \tag{2.7}$$

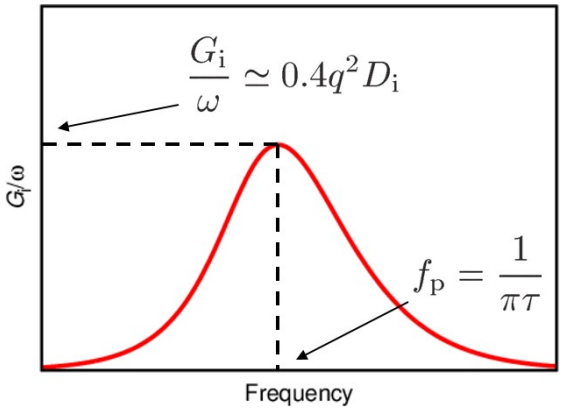

Figure 2.27: G_i/ω as a function of measured frequency f.

As a result,

$$\begin{aligned} j\omega(C_s + C_i) + G_i &= \frac{(j\omega C_m + G_m)j\omega C_0}{j\omega(C_0 - C_m) - G_m} \\ &= -\frac{(-\omega^2 C_0 C_m + j\omega C_0 G_m)[j\omega(C_0 - C_m) + G_m]}{\omega^2(C_0 - C_m)^2 + {G_m}^2} \\ &= \frac{\omega^2(C_0 - C_m)C_0 G_m + \omega^2 C_0 C_m G_m}{\omega^2(C_0 - C_m)^2 + {G_m}^2} + j \times ... \end{aligned} \tag{2.8}$$

Equating two sides for Eq. 2.8 and extracting the real part, we obtain

$$\frac{G_i}{\omega} = \frac{\omega {C_0}^2 G_m}{\omega^2(C_0 - C_m)^2 + {G_m}^2}, \tag{2.9}$$

from which we can calculate the interface state conductance from the measurement data.

Moreover, using the admittance of continuous interface states, which will be derived in appendix B, we obtain

$$\begin{aligned} \frac{G_i}{\omega} &= \frac{q^2 D_i \ln(1 + \omega^2\tau^2)}{2\omega\tau} \\ C_i &= \frac{q^2 D_i \text{atan}(\omega\tau)}{\omega\tau}, \end{aligned} \tag{2.10}$$

where q is the electron charge, D_i is the interface state density, τ is the electron trapping time, and ω is the angular frequency. Equation 2.10 is the basis of the conductance method. If we plot G_i/ω as a function of the measured frequency $f = \omega/2\pi$, we will observe a peak as shown in Fig. 2.27. From the peak of frequency-dependence G_i/ω, we can calculate the interface density D_i given by

$$\frac{G_i}{\omega} \simeq 0.4q^2 D_i, \tag{2.11}$$

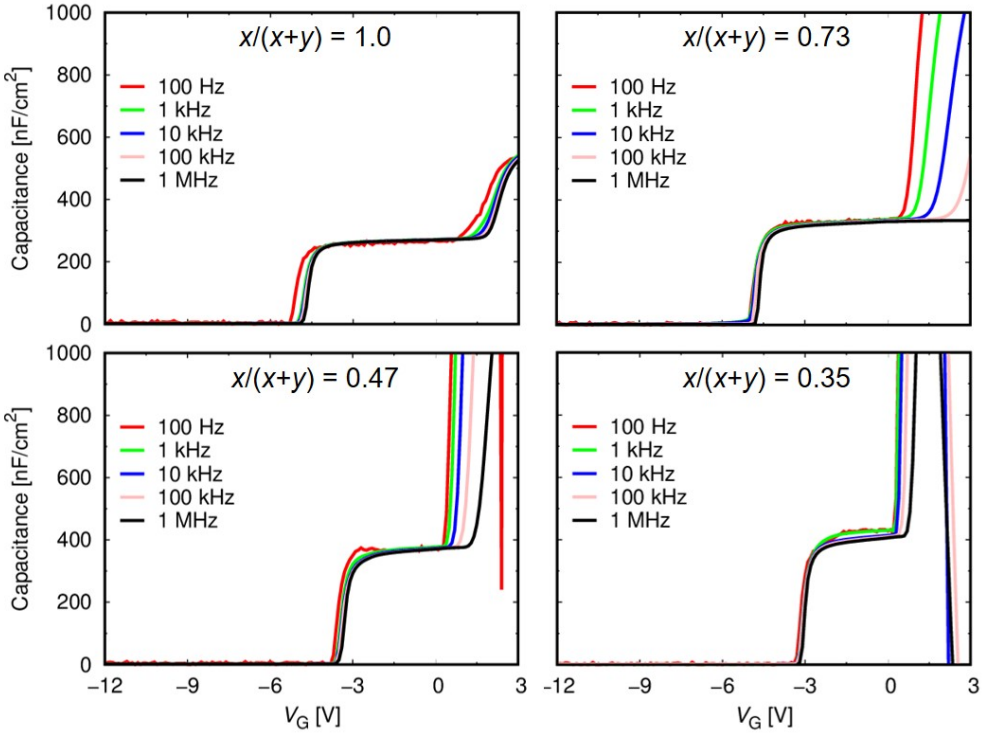

Figure 2.28: *C-V* measurements with different frequencies for the AlTiO/AlGaN/GaN MIS capacitors.

and electron trapping constant τ given by

$$\tau = \frac{1}{\pi f}. \tag{2.12}$$

Frequency dispersion analysis of AlTiO/AlGaN/GaN MIS devices

Figure 2.28 shows the *C-V* measurements under different frequencies for the AlTiO/AlGaN/GaN MIS capacitors with the insulator thickness of 11 nm. We carried out the measurement only for four compositions: $x/(x+y) = 1.0$, 0.73, 0.47, and 0.35. Using the experiment data, we extract $G_{\rm i}/\omega$ based on Eq. 2.9 and plot as function of f in Fig. 2.29, exhibiting the form given by Eq. 2.10.

From the peak positions, we estimate the interface state density $D_{\rm i}$ and the electron trapping constant τ based on Eq. 2.11 and Eq. 2.12. Figure 2.30 shows the relation between $D_{\rm i}$ at the AlTiO/AlGaN interfaces and τ for four compositions.

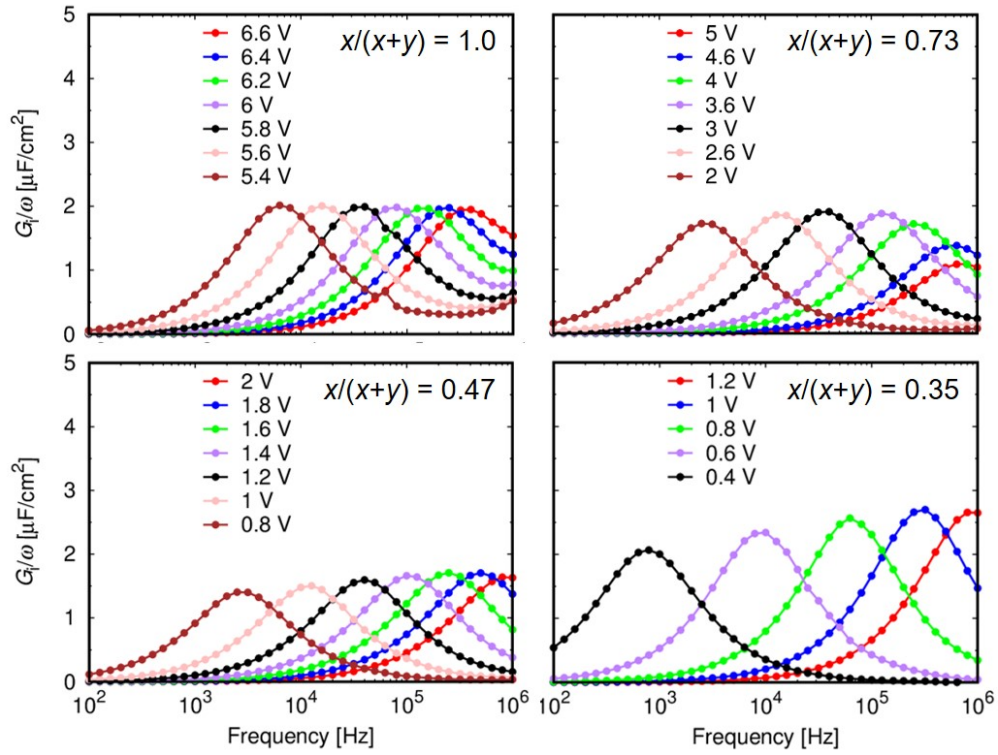

Figure 2.29: G_i/ω depending of the frequency for the AlTiO/AlGaN/GaN MIS capacitors.

The trapping constant is given by

$$\tau = \tau_0 \exp\left(\frac{E_c - E}{k_B T}\right), \tag{2.13}$$

where τ_0 is a time constant determined by the capture cross section of the trap, E is the energy level of the trap below conduction band level E_c, k_B is the Boltzmann

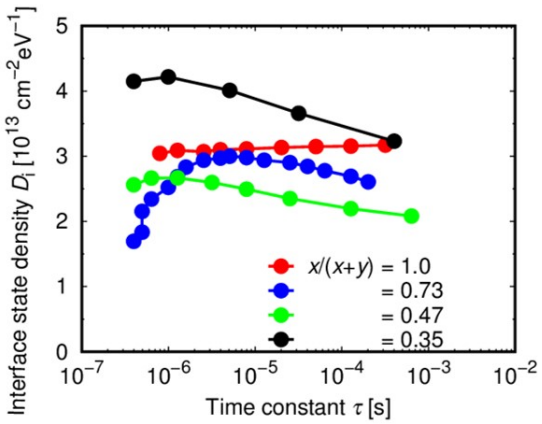

Figure 2.30: The relation between the interface state density D_i and the electron trapping constant τ for each composition.

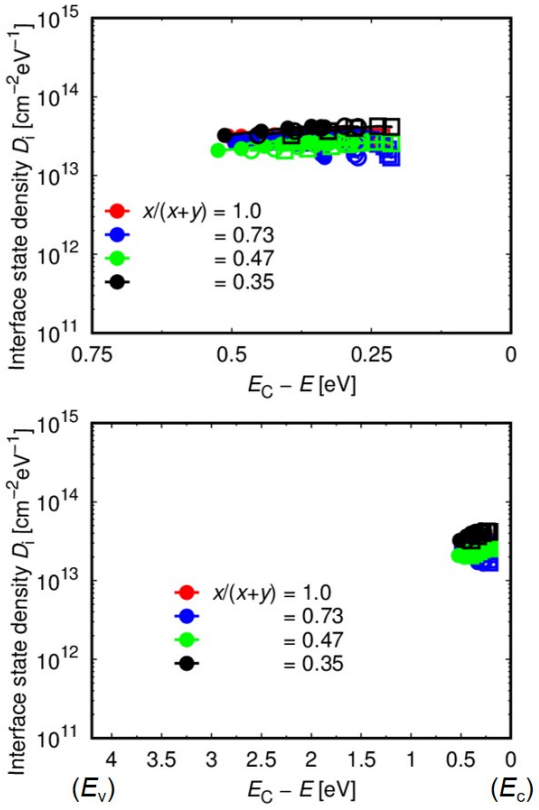

Figure 2.31: The interface state density D_i as functions of the energy $E_\mathrm{c} - E$ for each composition.

constant, and T is the temperature. Although τ_0 is ambiguous, assuming a wide range of $\tau_0 = 1 - 100$ ps, we can estimate $E_\mathrm{c} - E$. As a result, we obtain Fig. 2.31, showing D_i as functions of $E_\mathrm{c} - E$.

Figure 2.31 indicates a very similar shallow interface state density $D_\mathrm{i} \sim 2 \times 10^{13}$ cm^{-2}eV^{-1} at the AlTiO/AlGaN/GaN interfaces for four compositions. This suggests that deep interface state densities are also similar, since interface states generally have a U-shaped density of states, from the shallow interface state density above, we can expect a deep interface state density of $\leq 10^{13}$ cm^{-2}eV^{-1} or less. Therefore, at deep interface states, the generated negative charge density could be $\sim 10^{13}$ cm^{-2}. However, there is a difference between the positive interface fixed charge densities for each composition as shown in Table 2.2, roughly $\sim 1 \times 10^{13}$ cm^{-2} as the Al composition decreases from $x/(x+y) = 1$ to 0.35. Thus, it is safe to clarify that there is almost no correlation between the interface fixed charge

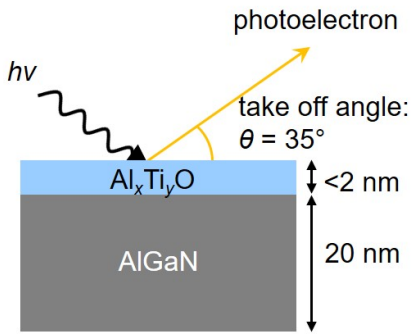

Figure 2.32: The sample schematics for XPS measurement.

density and interface state density.

2.3.3 Material characterization

Although the mechanism of formation of the positive interface fixed charge is not fully elucidated, there are some suggestions that the positive interface fixed charge is generated due to a positively ionized donor at the oxide insulator-AlGaN interface, where oxygen [51] or oxygen vacancy acts as the donor. In any cases in which the positive fixed charge at AlTiO/AlGaN interface is formed, the oxygen bonding states could affect the formation of the positive interface fixed charge. Therefore, we carried out X-ray photoelectron spectroscopy (XPS) to investigative the bonding states at the AlTiO/AlGaN interface. Because the inelastic mean free path of electron $\simeq$ 2 nm for the photon energy of 1486 eV [81], samples with thin AlTiO thickness were prepared as shown in Fig. 2.32.

Figure 2.33 shows the wide scan spectra for three typical compositions of AlTiO, from which we can identify the peak positions of each element. Afterward, high resolution scan for each peak was carried out. Due to the potential difference between samples and detector, the spectra will be shifted. Thus, we calibrated the peak positions by using C-C binding energy from C1s spectra. Figure 2.34 shows XPS spectra of C1s, illustrating different bonding states of carbon (C-C, C-O-C, or O-C=O). The open dots are measurement data and the red lines are the fitted curves given by the sum of individual Gaussian peaks for each bonding state. We fixed the peak position of C-C at 284.8 eV, and used the shifting energy

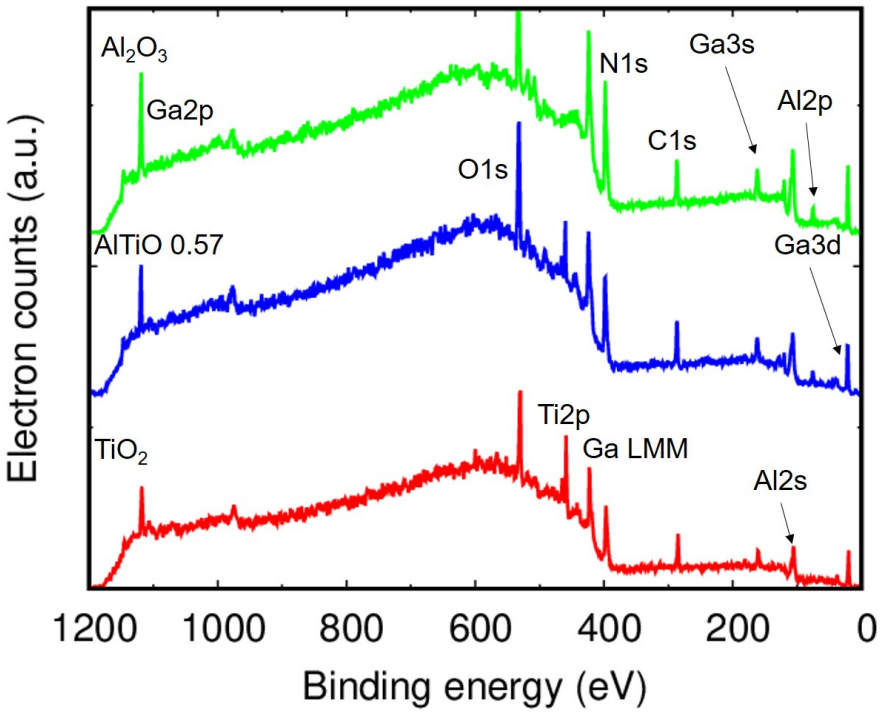

Figure 2.33: Examples of wide scan spectra of the samples.

to calibrate for other peak positions.

At AlTiO/AlGaN interface, Al, Ti, and Ga bonding with O and N are important to identify the origin of the positive interface fixed charge. Here we focus on the chemical shifts of Al2p, Ti2p, and Ga3d because they are responsible for chemical structures of AlTiO and AlGaN. Figure 2.35, 2.36, and 2.37 show the XPS spectra of Al2p, Ti2p, and Ga3d, respectively.

For each peak position, we assume that only N and O make the chemical bond with each element, so each peak position was fitted with 2 Gaussian functions corresponding to metal-O and metal-N binding energies. The parameters used for fitting are summarized in Table 2.3. From the fitting, we can estimate the ratio of

Table 2.3: Peak position of each bonding state for fitting [82].

Bonding state	Peak position [eV]	Bonding state	Peak position [eV]
Al-N	73.5	Al-O	74.3
Ti-N	458.2	Ti-O	459.2
Ga-N	19.4	Ga-O	20.4

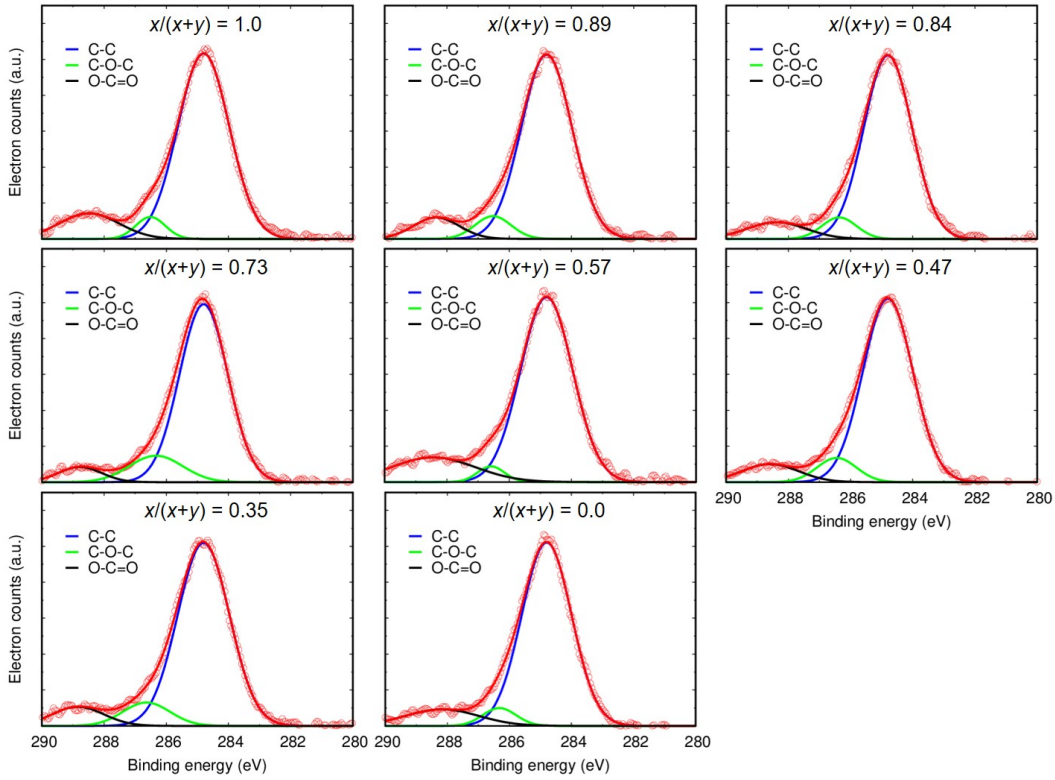

Figure 2.34: XPS spectra of C1s.

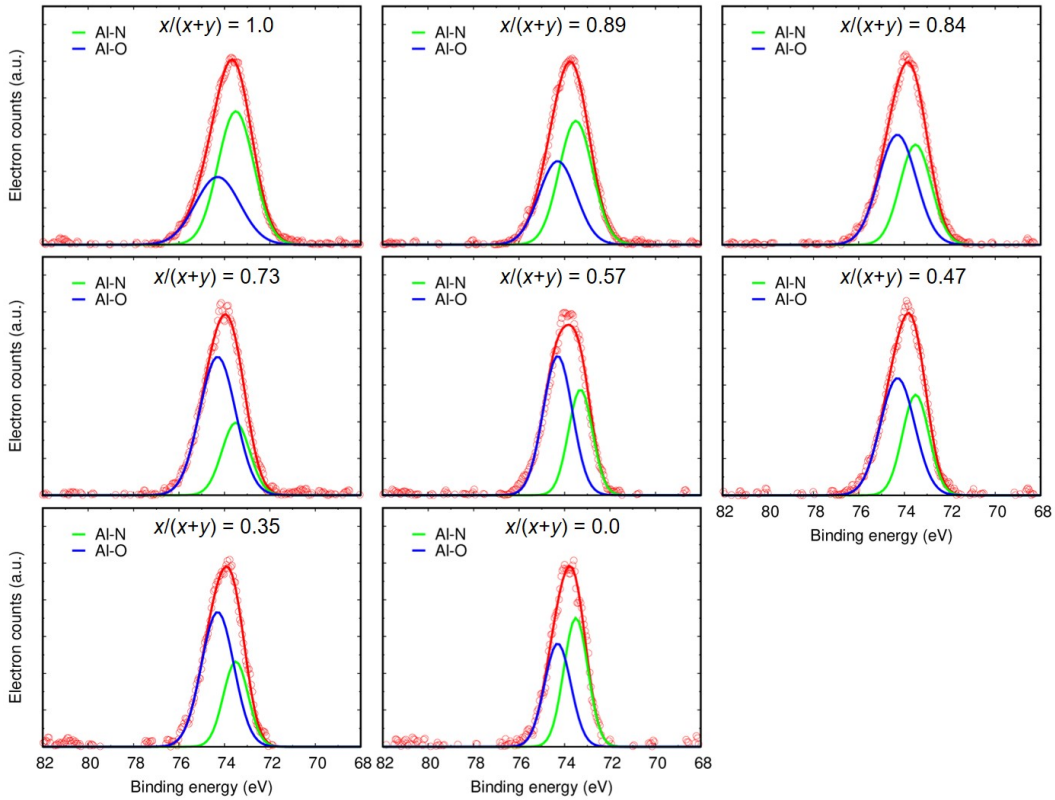

Figure 2.35: XPS spectra of Al2p.

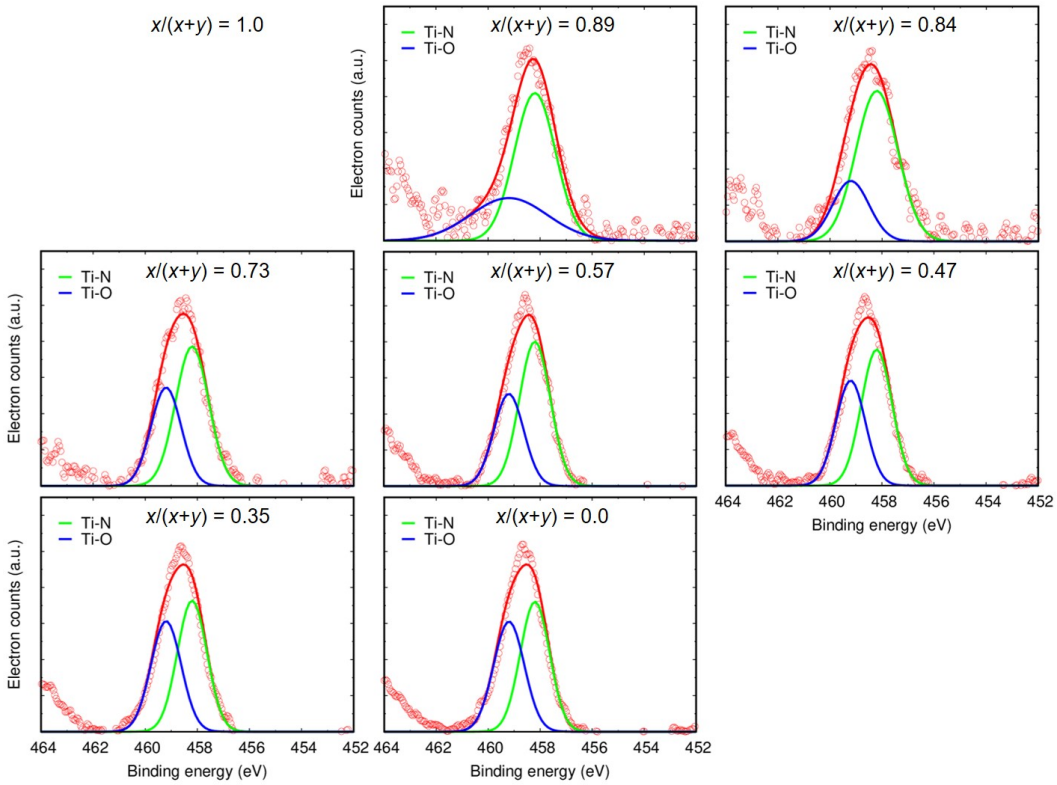

Figure 2.36: XPS spectra of Ti2p.

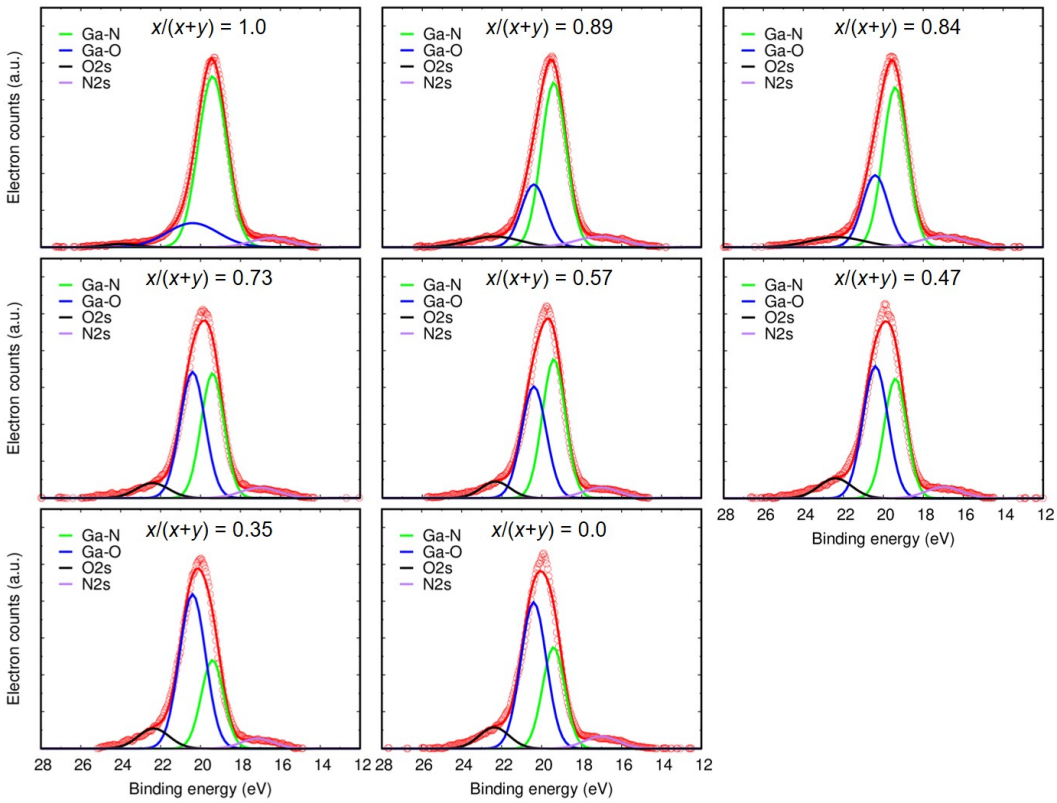

Figure 2.37: XPS spectra of Ga3d.

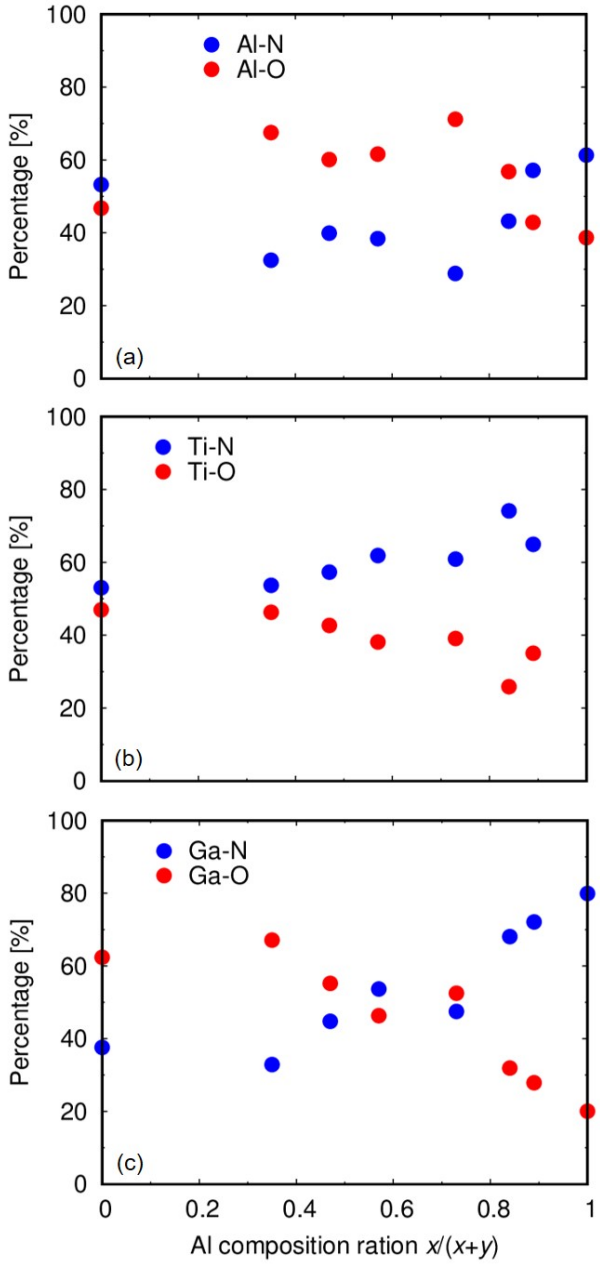

Figure 2.38: Percentage of O-related and N-related bonding states for (a) Al2p, (b) Ti2p, and (c) Ga3d.

O-related and N-related bonding state for each metal by calculating the area ratio. Figure 2.38 summarizes the percentage of O-related and N-related bondings with the metals as functions of the AlTiO composition. We find a trend that, with a decrease in the composition, the percentage of O-related bond increases and the percentage of N-related bond decreases. This behavior is expected for Ti2p spectra, since more TiO_2 molecules are deposited at the interface for low com-

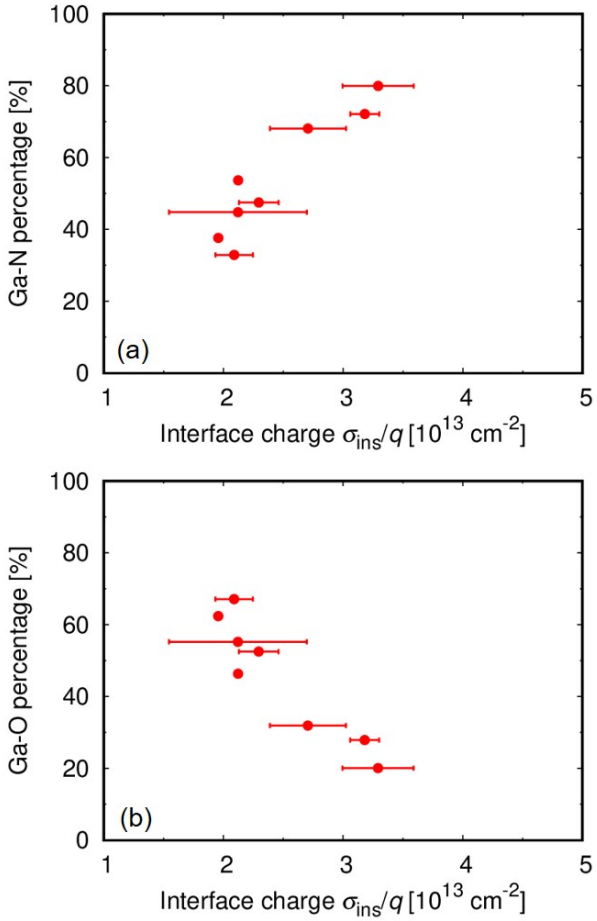

Figure 2.39: (a) Ga-N percentage and (b) Ga-O percentage of Ga3d as functions σ_{ins}.

positions. On the other hand, for low AlTiO compositions, less Al_2O_3 molecules are deposited and the number of Ga atoms is fixed. Thus we can conclude that oxygen related bonding increases as the composition decreases.

Because the number of Ga atoms is independent of the AlTiO composition, the bonding state of Ga3d can attribute to the formation of the positive interface fixed charge. Figure 2.39 plots relation between Ga-N percentage and Ga-O percentage of Ga3d as functions of the positive interface fixed charge density σ_{ins}. We observe a trend that with a decrease in the positive interface fixed charge density, the Ga-N percentage decreases, i.e. the Ga-O percentage increases. This suggests that incorporation of TiO_2 leads to an increase in the O-related bonding, suppressing the interface fixed charge, although we do not know the mechanism of this behavior. Further works are required to clarify this behavior.

Chapter 3

Interface charge engineering in partially-recessed AlGaN/GaN MIS devices using AlTiO insulators and normally-off operations

It has been shown in the previous chapter that AlTiO is useful for interface charge engineering owing to a trend that the positive AlTiO/AlGaN interface fixed charge is suppressed in comparison with Al_2O_3. Using 1D Poisson-Schrödinger calculation, we estimate the positive interface fixed charge density σ_{ins} needed to obtain the indicated threshold voltages in the partially-gate-recessed AlTiO/AlGaN/GaN MIS devices using $x/(x+y) = 0.73$ composition as depicted in Fig. 3.1. The figure shows the benefits of utilizing interface charge engineering for normally-off operations in AlGaN/GaN MIS devices; we can obtain high threshold voltages with a thick remaining AlGaN thickness, resulting in a good channel electron transport. Therefore, in this chapter, we investigate interface charge engineering in partially-gate-recessed AlTiO/AlGaN/GaN MIS devices with a rather thick remaining AlGaN layer.

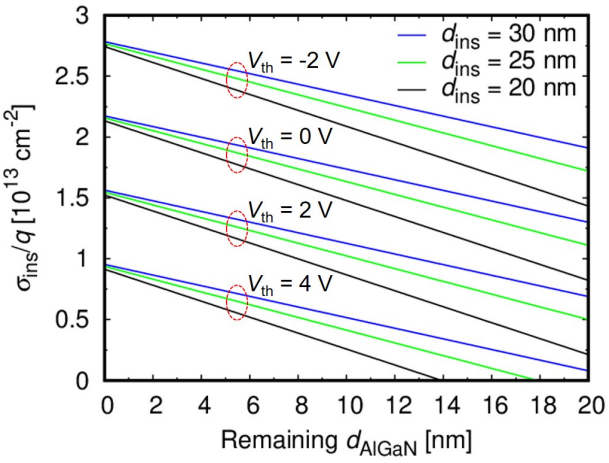

Figure 3.1: Estimated positive fixed charge density σ_{ins} at AlTiO ($x/(x+y) = 0.73$)/AlGaN interface depending on the remaining AlGaN thickness in order to obtain the indicated threshold voltages for some insulator thickness.

3.1 AlTiO/AlGaN/GaN MIS device fabrication process employing partial gate recess method

The process flow of the partially-gate-recessed AlTiO/AlGaN/GaN MIS devices, MIS-capacitors and MIS-FETs, is illustrated in Fig. 3.2. Starting from an AlGaN/GaN heterostructure, Ohmic electrodes were formed on the substrate. As gate recess process, the AlGaN layer was etched by using electron cyclotron resonance (ECR) nitrogen plasma. After that, AlTiO deposition by ALD was carried out. After a necessary device isolation, gate electrodes were formed, completed the device fabrication.

Because the Ohmic electrode formation and insulator deposition processes are the same with the previous chapter, I will omit them in the following sections.

Gate recess process

The process flow of the gate recess is shown in Fig. 3.3.

Surface treatment in acetone, methanol, and DIW for 3 minutes was carried out before coating the resist. LOL2000/TSRM89000 were coated on the samples.

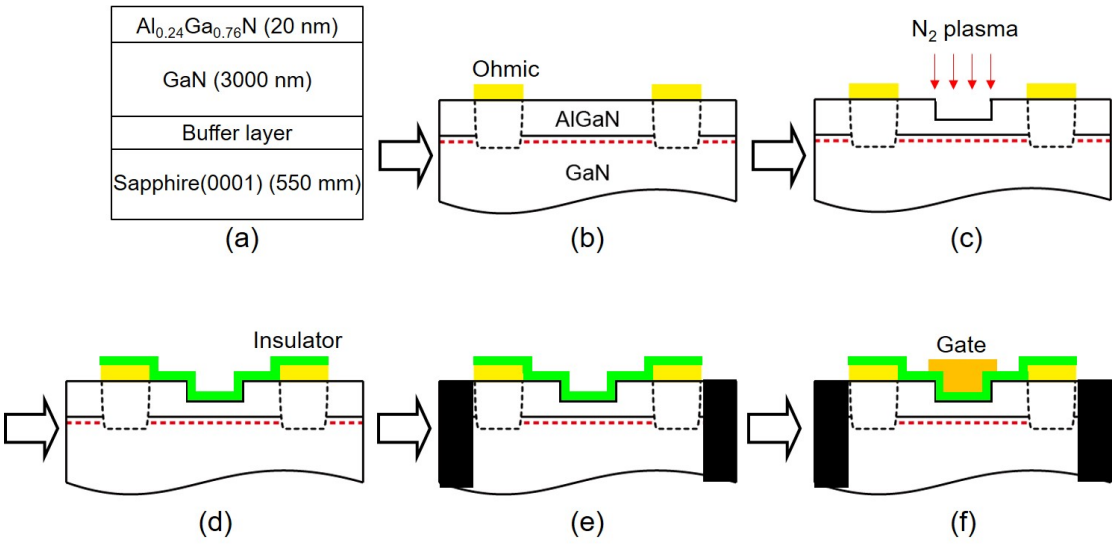

Figure 3.2: Process flow of the partially-gate-recessed AlTiO/AlGaN/GaN MIS devices. (a) AlGaN/GaN heterostructure. (b) Ohmic electrode formation. (c) Gate recess by N_2 plasma etching. (d) Insulator deposition. (e) Device isolation. (f) Gate electrode formation.

After exposure by MLA and development by TMAH for 50 seconds, the samples were loaded into ECR chamber.

Figure 3.4 illustrates a simplified schematics of the ECR system used for etching. The samples were put in the center of the sample stage, which can be rotated. Nitrogen gas was introduced into the chamber, where it would be ionized to make plasma. The ionized atoms were accelerated through an acceleration electrode, and their density can be measured by Faraday cup. For the etching process, we employed the acceleration voltage of 100 V, microwave power of 100 W, and Faraday cup current density of ~ 0.3 mA/cm^2.

Next, surface treatment was carried out by O_2 plasma ashing at 50 Pa, 20 W, and 10 minutes to remove fragments sticking to the resist edges during the etching process. Then the samples were cleaned by semico-clean for 5 minutes, and DIW for 3 minutes. Finally, the resist layers were removed by the resist remover.

After finishing the resist removal process, the etching depth and surface roughness were measured by atomic force microscopy (AFM). Figure 3.5(a) shows a

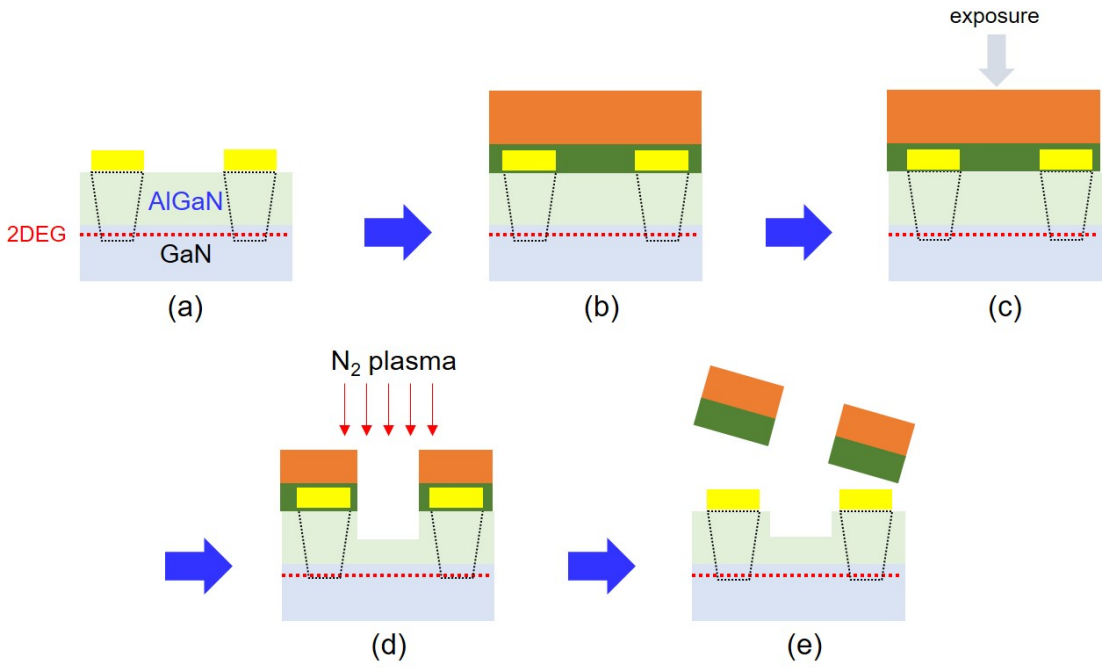

Figure 3.3: Process flow of the gate recess. (a) Surface treatment. (b) Resist coating. (c) Patterning and development. (d) Etching by N_2 plasma. (e) Surface treatment and resist removal.

linear relation between the etching depth d_e and the etching time, from which we obtain a stable etching rate of 1.8 nm/min. Moreover, the morphology of the etched surface shown in Fig. 3.5(b) illustrates a smooth surface with the surface roughness of 0.5 nm, which is not changed from that before etching. We consider

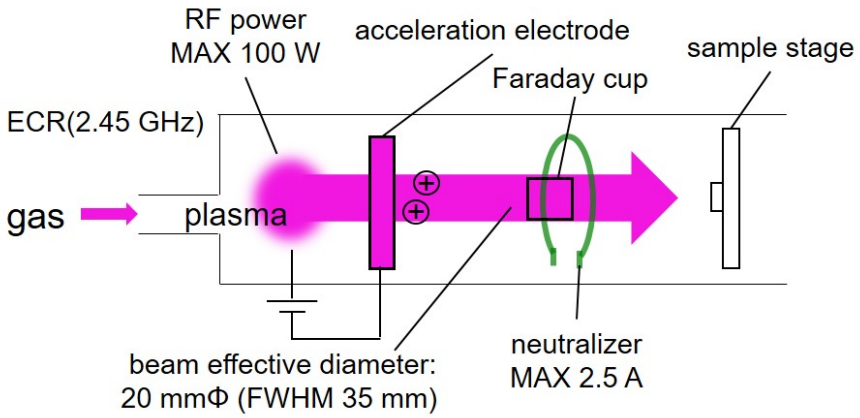

Figure 3.4: A simplified schematics of the ECR system.

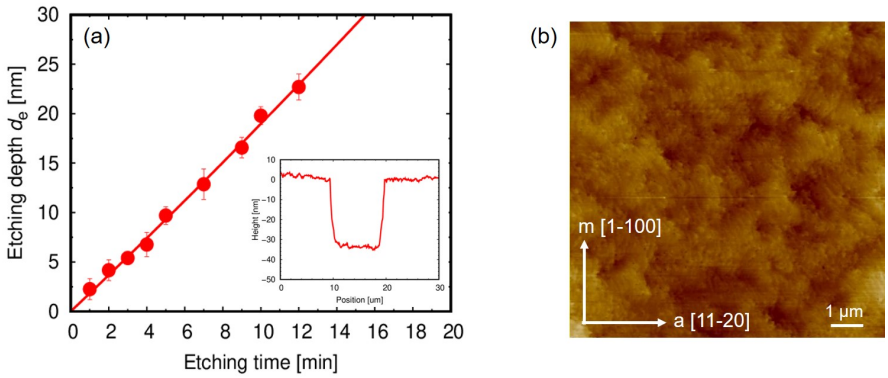

Figure 3.5: (a) Etching depth d_e as functions of etching time, showing linear relation. The inset shows an example of AFM measurement, from which we can estimate the etching depth. (b) The morphology of the etched surface, showing a smooth surface.

that dry etching by ECR N_2 plasma is advantageous for the gate recess method.

Device isolation

After the insulator deposition process, device isolation process was carried out. The process flow of the device isolation is shown in Fig. 3.6.

After the usual wet surface treatment using acetone, methanol, and DIW for 3 minutes, 3 resist layers, GL2000/LOL2000/TSRM8900 were coated on the samples. After exposure by MLA and development by TMAH, the samples were baked at 140 °C for 5 minutes to harden the TSRM8900 layer. Then, the samples were treated by O_2 plasma at 30 Pa, 20 W, and 6 minutes to remove the GL2000 layer on the exposed areas.

Next, the ion implantation process was carried out. Implant isolation is a common method used in semiconductor device fabrication processes for inter-device isolation [84]. The general ion implantation method is to cause damages in the semiconductor crystal, resulting in the enhancement of electrical resistance in the defined area between the devices. It was reported that the implanted ion creates energy levels in or near mid-gap [85].

B^+ ion from BF_3 gas was induced and implanted into the sample by acceleration voltages of 30 keV, 50 keV, and 100 keV. The three-step implantation ensures uniform distribution of ions upto a certain depth in GaN from the AlGaN surface.

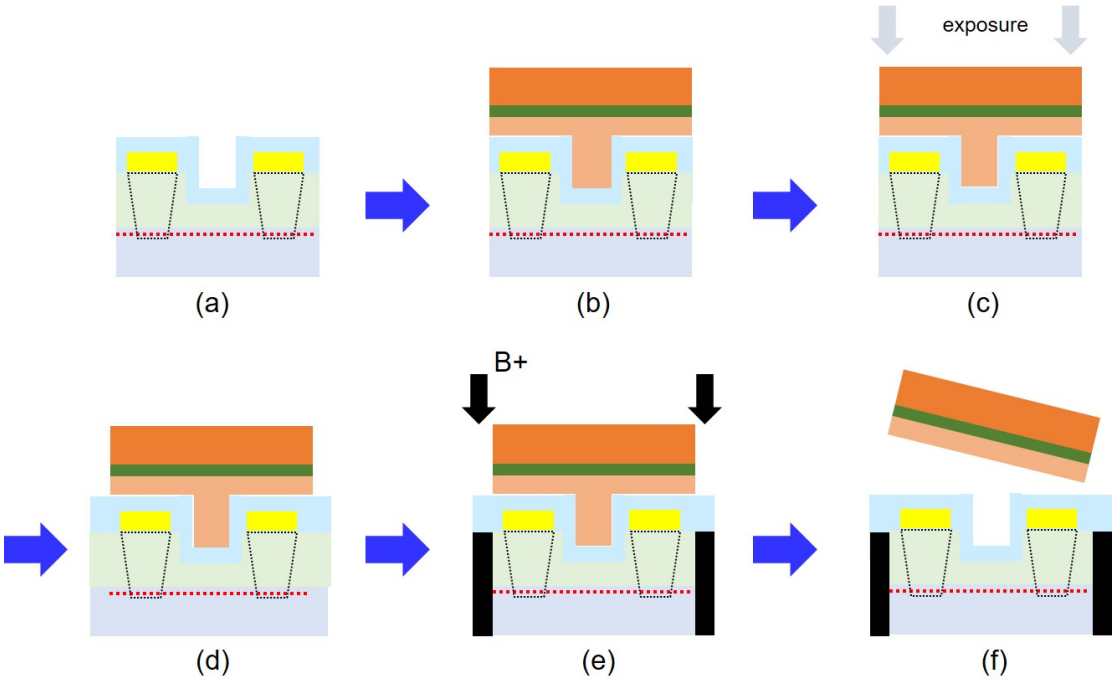

Figure 3.6: Process flow of the device isolation. (a) Surface treatment. (b) Resist coating. (c) Patterning and development. (d) O_2 plasma ashing. (e) Ion implantation. (f) Resist removal.

Figure 3.7 obtained by SRIM/TRIM simulator [83] depicts the B^+ concentration distribution relation with depth and acceleration voltage, showing that $\sim$ 300 nm

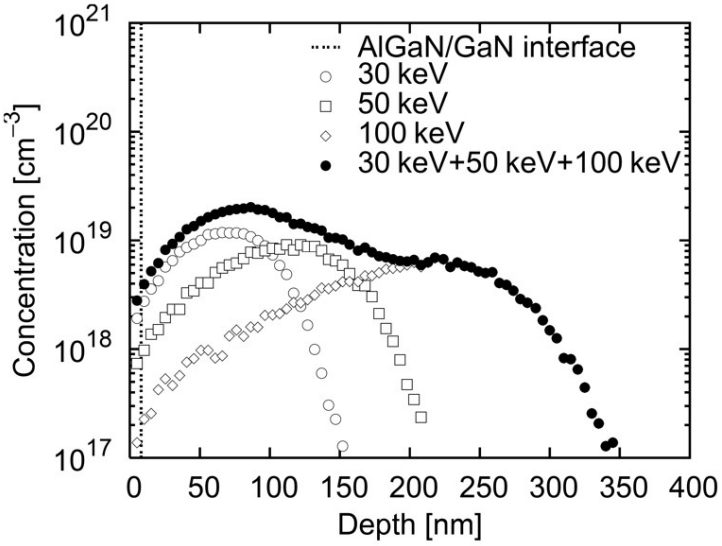

Figure 3.7: The ion concentration as a function of depth and acceleration voltage [83].

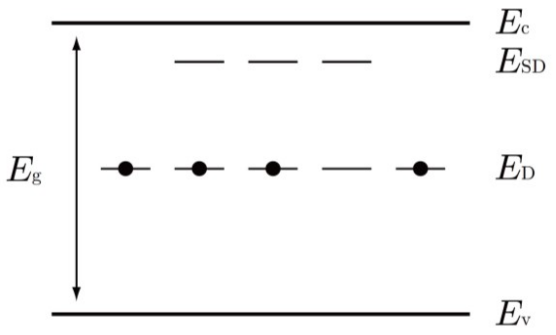

Figure 3.8: Deep level created by ion implantation.

from the AlGaN surface can be ion-implanted, even if we include the insulator layer. The substitutional or interstitial B^+ ions can cause Al, Ga, N vacancies which create deep levels that trap the carriers as shown in Fig. 3.8. As a result, the implanted area has high electrical resistance. Such deep levels can absorb and emit visible light with corresponding energy, causing the dark-yellowish look of the wafer after the ion implantation. The ion source for implantation is not limited to B^+, O^+ and Fe^+ are possible options [86, 87].

After that, resist removal was carried out. After dipping in resist remover for 30 minutes at 60 °C, the samples were treated by ultrasonic for 1 minutes to fully remove the remaining resist. Finally, wet treatment using acetone, methanol, DIW for 3 minutes completed the device isolation process.

Gate formation

The process flow is carried out similarly with that of the previous chapter. However, it has been reported that post-gate annealing (PGA) is beneficial for fully-recessed Al_2O_3/GaN MIS-FETs [88]. Therefore, we also conducted PGA at 400 °C in N_2 atmosphere for 10 minutes, and compare the results with the devices without PGA.

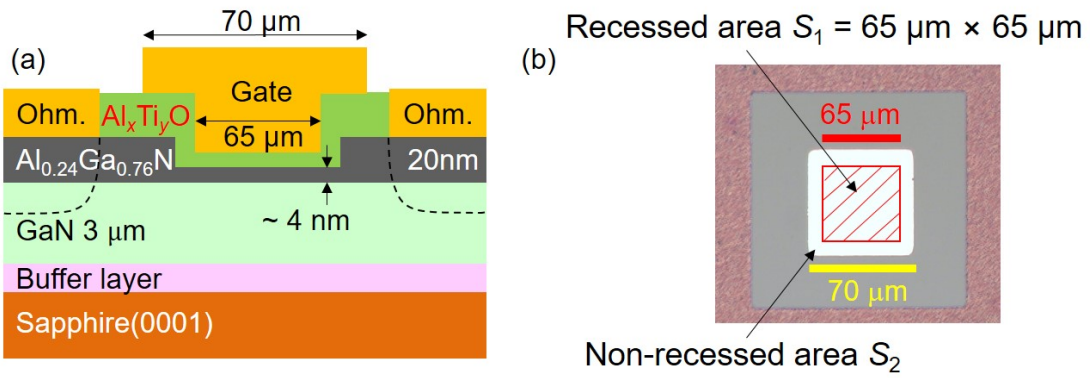

Figure 3.9: (a) Device size and (b) top view image of the partially-recessed AlTiO/AlGaN/GaN MIS-capacitors.

3.2 AlTiO/AlGaN/GaN MIS-capacitor characterization

In the previous chapter, we found a trend that a decrease in the AlTiO compositions leads to a decrease in the positive interface fixed charge density, as well as decreases in the energy gap E_g and the AlTiO/AlGaN conduction band offset φ. Therefore, in this chapter, we employed three compositions: $x/(x+y)$ =1.0 ($k \simeq 8$, $E_g \simeq 7$ eV, $\varphi \simeq 1.7$ eV), $x/(x+y)$ =0.84 ($k \simeq 10$, $E_g \simeq 6.3$ eV, $\varphi \simeq 1.4$ eV), and $x/(x+y)$ =0.73 ($k \simeq 13$, $E_g \simeq 6$ eV, $\varphi \simeq 1.3$ eV), whose $\varphi \leq 1$ eV to avoid the leakage. The device size and the top view image of the fabricated capacitors are shown in Fig. 3.9(a) and (b), respectively, where the recessed area $S_1 = 65^2$ μm^2 and the non-recessed area $S_2 = (70^2 - 65^2)$ μm^2 under the gate are surrounded by the Ohmic electrodes.

Figure 3.10 shows the I-V_G characteristics of the MIS-capacitors without and with PGA for several insulator thicknesses. We find that PGA can effectively suppress the leakage currents. In the negative bias, the current magnitude is reduced to the same order for all the compositions, while the leakage in the positive bias is suppressed $\simeq 10^2$ orders lower compared to that for the devices without PGA. Moreover, in case of Al_2O_3, PGA can improve the device operation, namely, suppress current collapse at high bias.

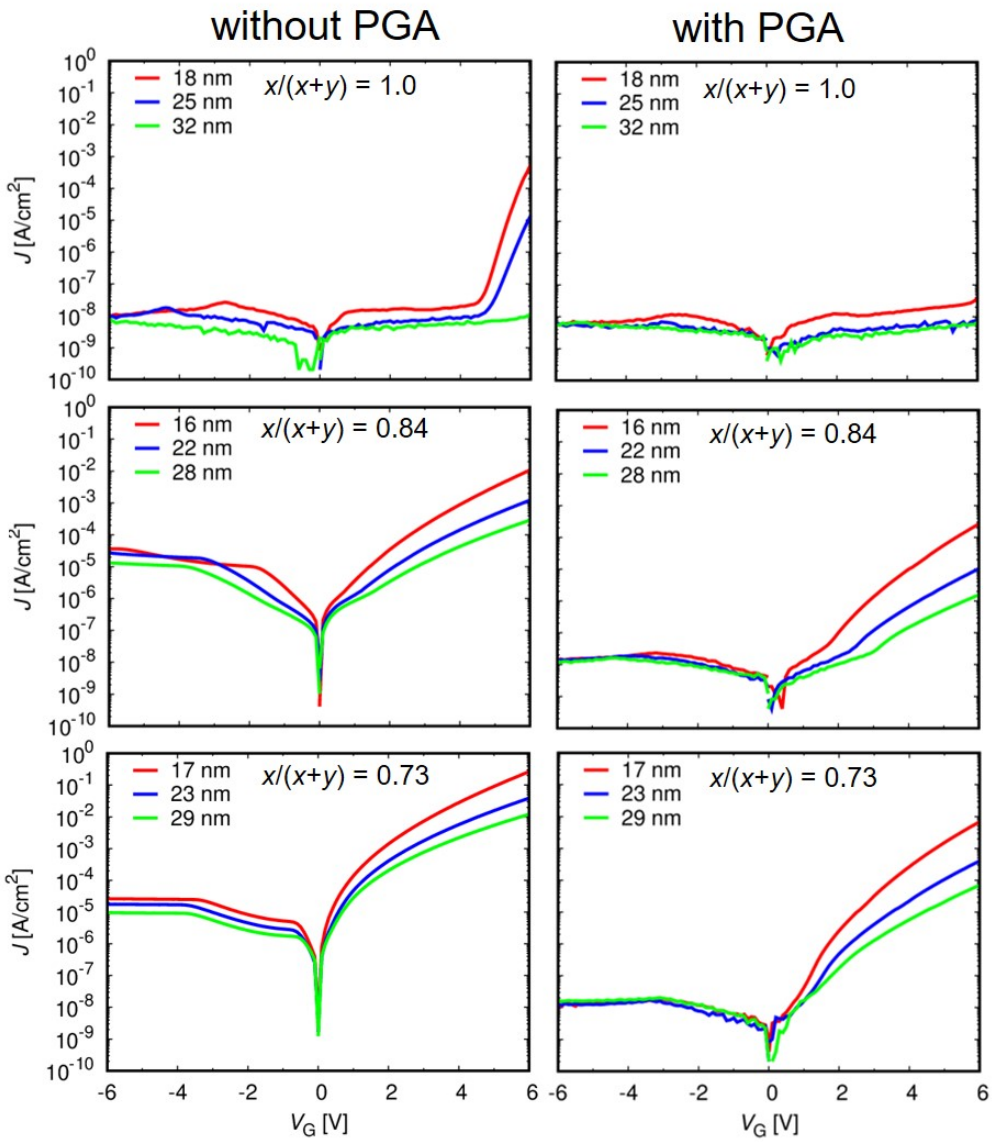

Figure 3.10: I-V_{G} characteristics of the MIS-capacitors.

Figure 3.11 shows the C-V_{G} characteristics of the MIS-capacitors at 1 MHz for several AlTiO insulator thicknesses, with the inset depicting the equivalent circuit of the devices, where the capacitance of the recessed area S_1 are in parallel with the capacitance of the non-recessed area S_2. We observe a step-like behavior of the C-V_{G} characteristics; the lower-voltage step corresponds to the threshold voltage of the non-recessed area, whereas the higher-voltage step to that of the recessed area. For $x/(x+y) = 1.0$, additional steps are observed in the range of $V_{\mathrm{G}} \gtrsim 3$ V, owing to the spill-over at the insulator/AlGaN in the non-recessed area, where rather large overdrive voltages are applied due to the negatively large threshold

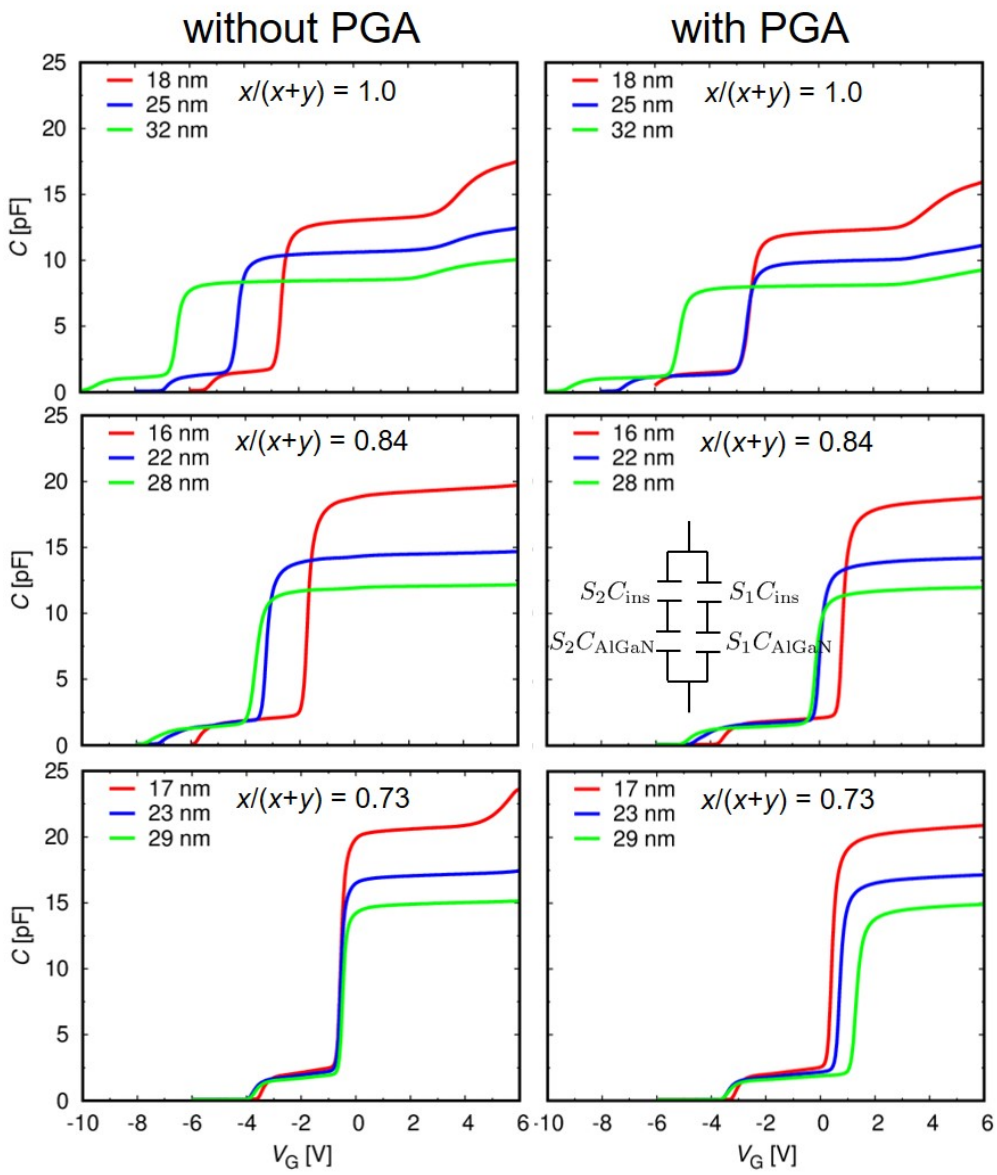

Figure 3.11: C-V_{G} characteristics of the MIS-capacitors.

voltages. PGA can slightly mitigate the effect, in particular, for $x/(x+y) = 0.73$, the spill-over effect is removed.

The 2DEG sheet concentration n_{s} is obtained by integration of C as a function of V_{G}, as shown in Fig. 3.12 with two linear fittings corresponding to n_{s} increases in the non-recessed and recessed area. The threshold voltage of the non-recessed area V_{th2} is determined at $n_{\mathrm{S}} = 0$, while that of the recessed area V_{th1} is obtained by the intersection between the two fitting lines.

As previous shown, the threshold voltage V_{th} of an AlGaN/GaN MIS device

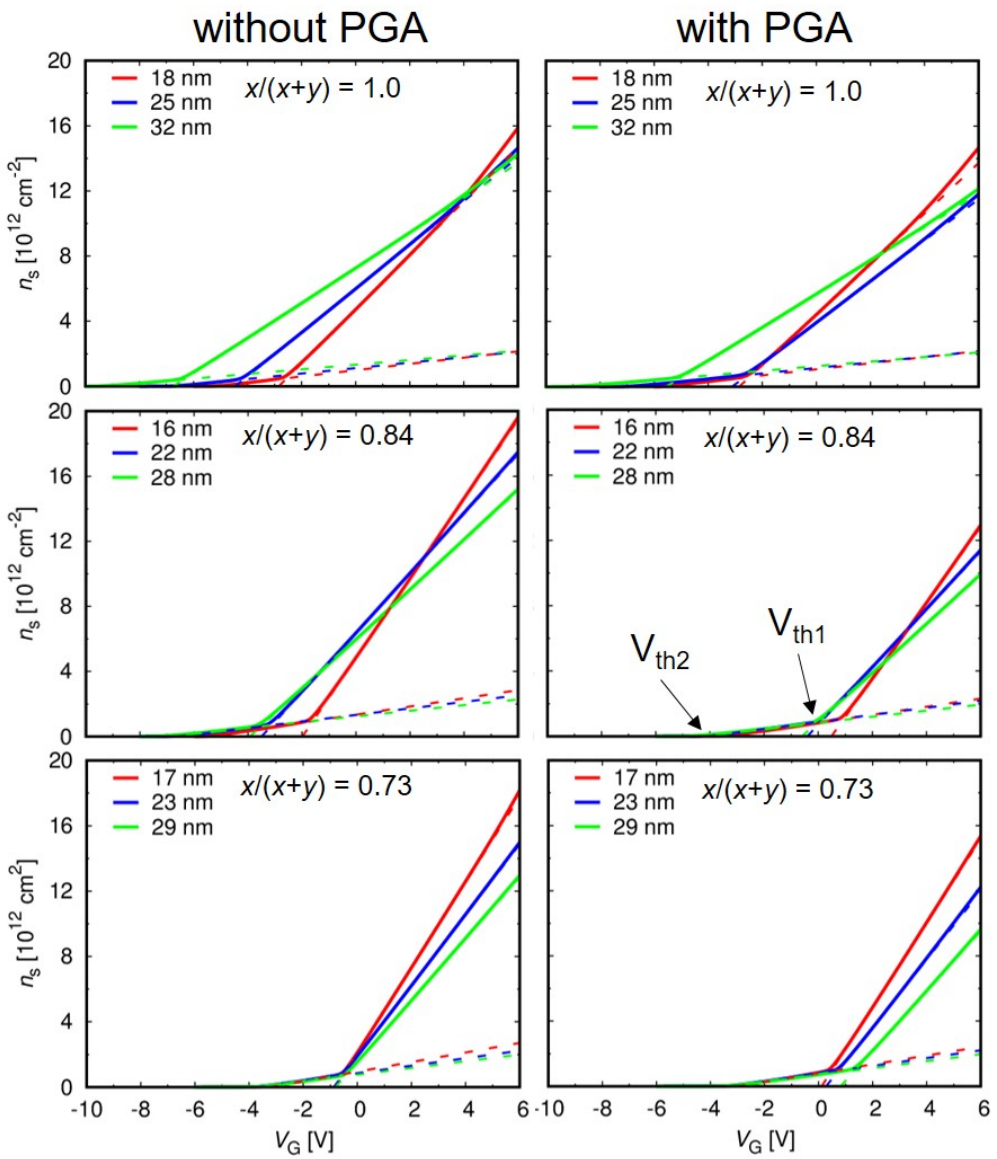

Figure 3.12: n_s-V_G characteristics of the MIS-capacitors.

having an insulator/semiconductor interface fixed charge density $\sigma_{\rm ins}$ is given by a linear function of the insulator thickness $d_{\rm ins}$,

$$V_{\rm th} = \frac{\sigma_{\rm GaN} - \sigma_{\rm ins}}{k_{\rm ins}\epsilon_0} d_{\rm ins} - \frac{\sigma_{\rm AlGaN} - \sigma_{\rm GaN}}{k_{\rm AlGaN}\epsilon_0} d_{\rm AlGaN} + (\phi - \varphi - \Delta E_{\rm C})/q. \qquad (3.1)$$

Figure 3.13 shows the obtained threshold voltages as functions of $d_{\rm ins}$. Basically we observe linear relations of $V_{\rm th}$-$d_{\rm ins}$, confirming that $V_{\rm th}$ is dominated by the positive interface fixed charge. We find that, for the devices without PGA, $V_{\rm th}$ is shifted positively in the recessed area in comparison with that in the non-recessed area. Even $d_{\rm ins} \sim 4$ nm is not enough to achieve $V_{\rm th} = 0$, owing to the high-density

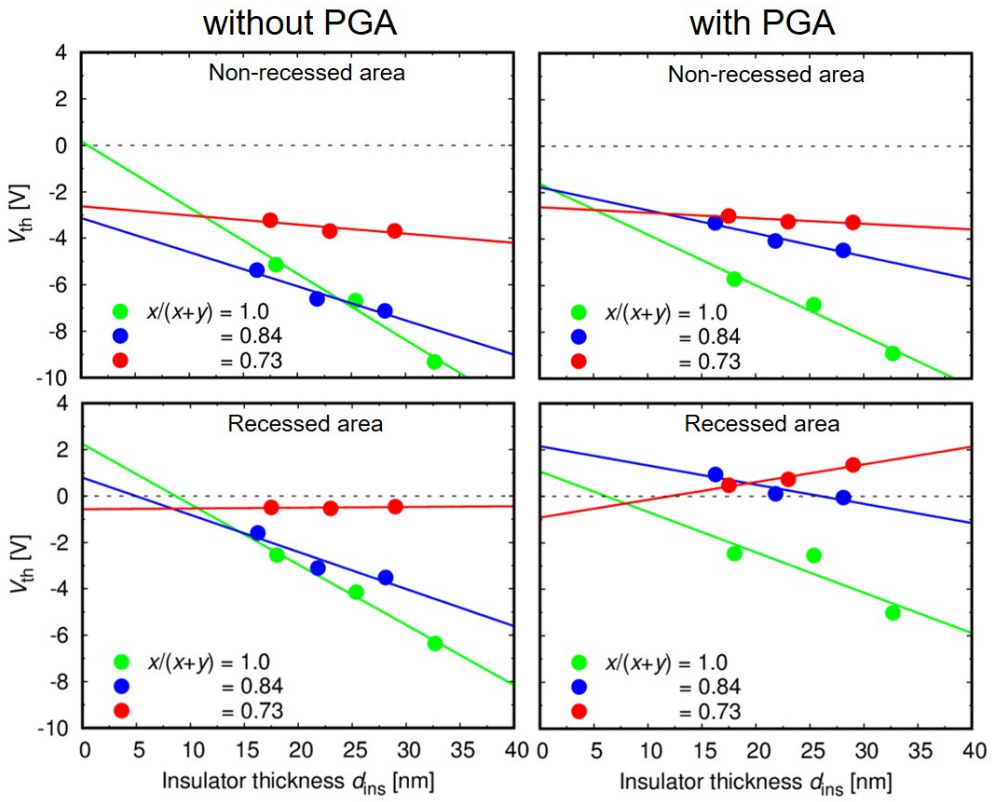

Figure 3.13: The threshold voltage $V_{\rm th}$ as functions of $d_{\rm ins}$ of the MIS-capacitors without and with PGA for the non-recessed and recessed areas.

positive interface fixed charge. On the other hand, PGA can shift the threshold voltages positively in both non-recessed and recessed areas compared to these in the devices without PGA. In particular, we observe $V_{\rm th} < 0$ of the recessed area for $x/(x+y) = 1.0$, showing that the AlGaN remaining thickness $d_{\rm AlGaN} \sim 4$ nm leads to normally-on operations for Al_2O_3/AlGaN/GaN MIS devices; whereas for $x/(x+y) = 0.84$ with $d_{\rm ins} < 26$ nm and $x/(x+y) = 0.73$ with $d_{\rm ins} > 12$ nm, we obtain $V_{\rm th} > 0$, normally-off operations for AlTiO/AlGaN/GaN MIS devices, where a positive $V_{\rm th}$-$d_{\rm ins}$ slope is observed for $x/(x+y) = 0.73$.

From the fitting using the relation (3.1), we can directly obtain $\Delta\sigma_{\rm ins} = \sigma_{\rm ins} - \sigma_{\rm GaN}$. Using the previous assumption in chapter 2, $\sigma_{\rm GaN} = 2.1 \times 10^{13}$ cm^{-2}, we evaluate $\sigma_{\rm ins}$ at the AlTiO/AlGaN interface for the non-recessed and recessed area, as summarized in Fig. 3.14, where the neutral AlTiO/AlGaN interface is indicated by the black dotted line. We find that, for the devices without PGA, there is almost no difference between $\sigma_{\rm ins}$ in non-recessed area and that in recessed area.

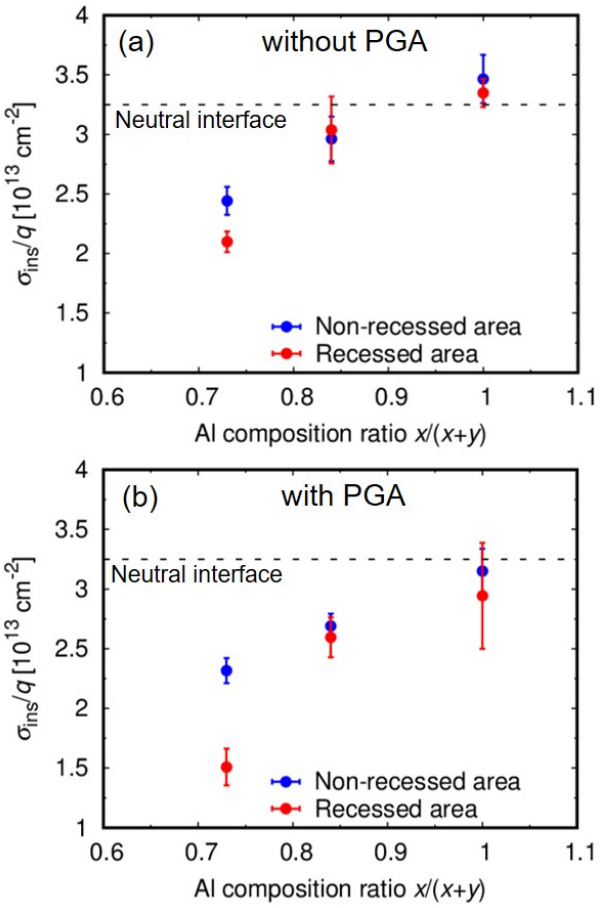

Figure 3.14: σ_{ins} as functions of the composition of the devices (a) without PGA and (b) with PGA. The black dotted line indicates neutral AlTiO/AlGaN interface.

This indicates no additional charge was introduced by the gate recess process; the threshold voltages in the recessed area are vertically shifted owing to the smaller AlGaN thickness. On the other hand, we find that σ_{ins} is suppressed for all devices in both non-recessed and recessed areas if PGA was conducted. We define $\sigma_{\mathrm{sup}} = \sigma_{\mathrm{ins}}$ (without PGA) $-\sigma_{\mathrm{ins}}$ (with PGA), namely the amount of positive interface fixed charge density suppressed by PGA, and plot it as function of the composition in Fig. 3.15. We find that while the effect of PGA for the non-recessed area decreases with a decrease in the composition, PGA can effectively decrease the positive interface fixed charge in the recessed area for lower compositions. As a result, for the $x/(x+y) = 0.73$ composition, we observe a rather low σ_{ins} leading to the positive V_{th}-d_{ins} slope. The positive slope is useful for fabricating normally-off devices, since more positive threshold voltages can be obtained by increasing

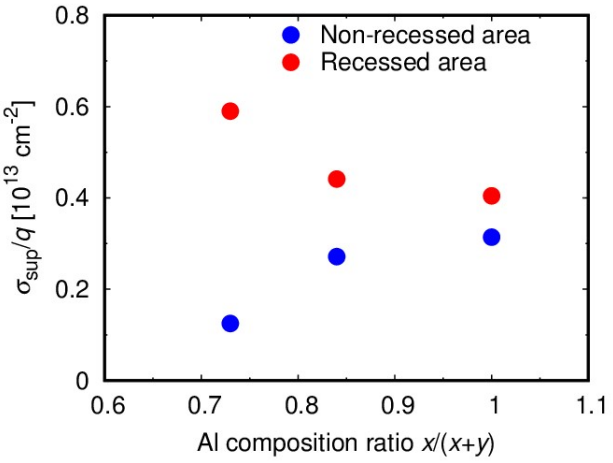

Figure 3.15: σ_{sup} depending on the composition.

the insulator thickness.

Figure 3.16 shows calculated 1D Poisson-Schrödinger band diagrams of the partially-recessed AlTiO/AlGaN/GaN MIS structures with $d_{\mathrm{AlGaN}} = 4$ nm and $d_{\mathrm{ins}} = 30$ nm at $V_{\mathrm{G}} = 0$ V, using σ_{ins} obtained by the experimental results. For the calculation, we assume that no damage was caused by the gate recess and PGA process, so only the change in σ_{ins} is observed. We then can use the same parameters obtained from the previous chapter such as the AlTiO-AlGaN conduction band offset φ and the metal-AlTiO barrier height ϕ to calculate the band diagram. We find that the decrease in the interface fixed charge density can reverse the direction of the electric fields in the AlTiO insulators for the $x/(x+y) = 0.84$ and 0.73 compositions. The larger the decrease in σ_{ins} is, the stronger the electric field is in AlTiO, shifting the threshold voltages positively. As a result, while all devices without PGA are normally-on devices, for the devices with PGA, we observe $V_{\mathrm{th}} < 0$ V for $x/(x+y) = 1.0$, while $V_{\mathrm{th}} \simeq 0$ V for $x/(x+y) = 0.84$, and in particular for $x/(x+y) = 0.73$, a clear normally-off operation $V_{\mathrm{th}} > 0$ V is indicated.

We conclude that using AlTiO with $x/(x+y) = 0.73$ composition is beneficial towards realization of normally-off operations for the partially-gate-recessed AlGaN/GaN MIS devices owing to the suppressed positive fixed charge density

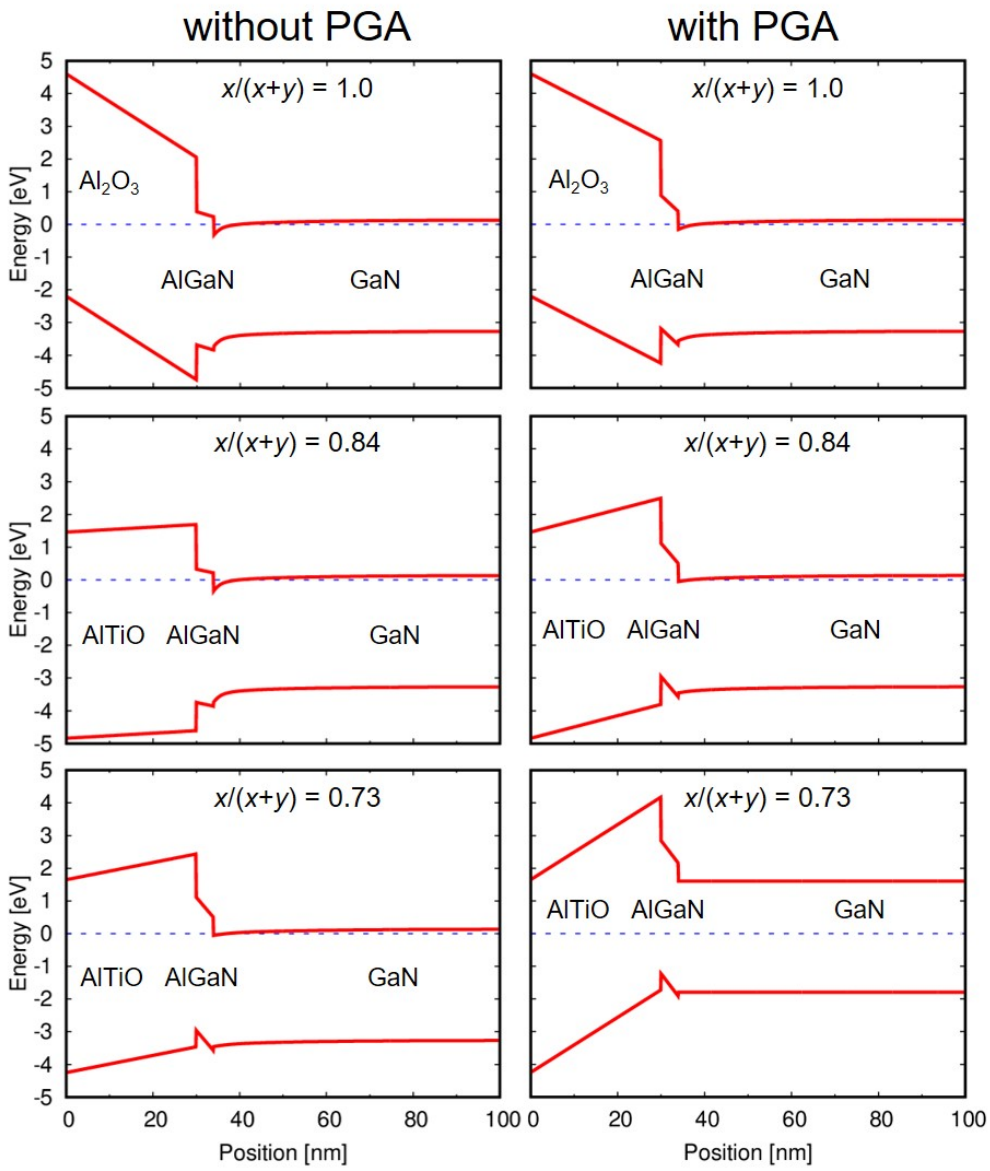

Figure 3.16: Calculated 1D Poisson-Schrödinger band diagrams of the partially-recessed AlTiO/AlGaN/GaN MIS structures with $d_{\mathrm{AlGaN}} = 4$ nm and $d_{\mathrm{ins}} = 30$ nm at $V_{\mathrm{G}} = 0$ V, using experimentally obtained σ_{ins}.

at AlTiO/recessed-AlGaN. However, towards the goal of achieving normally-off operations having good electron transport properties, the remaining AlGaN layer should be thicker, hence the positive interface fixed charge needs to be more suppressed. Using 1D Poisson-Schrödinger calculation for $x/(x+y) = 0.73$ composition, we estimate σ_{ins} needed to obtain the indicated threshold voltages in the partially-gate-recessed AlTiO/AlGaN/GaN MIS devices using $x/(x+y) = 0.73$

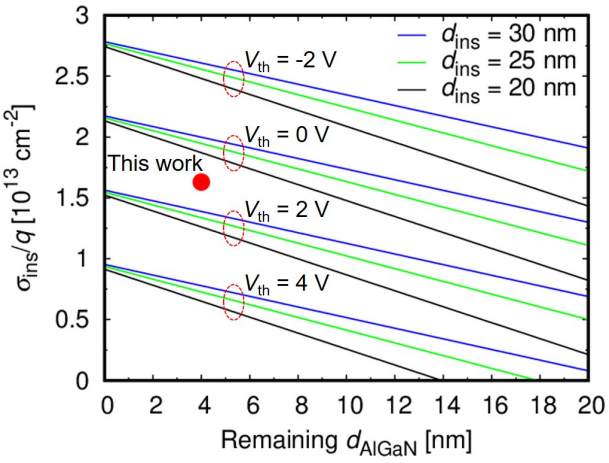

Figure 3.17: Estimated positive fixed charge density σ_{ins} at AlTiO ($x/(x+y) = 0.73$)/AlGaN interface depending on the remaining AlGaN thickness in order to obtain the indicated threshold voltages for some insulator thickness.

composition as depicted in Fig. 3.17. As we can see in the figure, this work is just a starting point, further investigations are needed to suppressed σ_{ins} to $\sim 10^{-12}$ cm^{-2} in order to realize normally-off operations for non-recessed AlGaN/GaN devices.

3.3 AlTiO/AlGaN/GaN MIS-FET characterization

In order to examine the normally-off operation, we characterized a partially-recessed AlTiO/AlGaN/GaN MIS-FET for $x/(x+y) = 0.73$ with PGA, whose

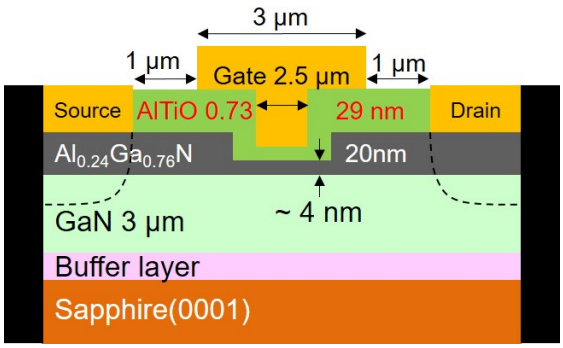

Figure 3.18: Schematics of the partially-recessed AlTiO/AlGaN/GaN MIS-FET.

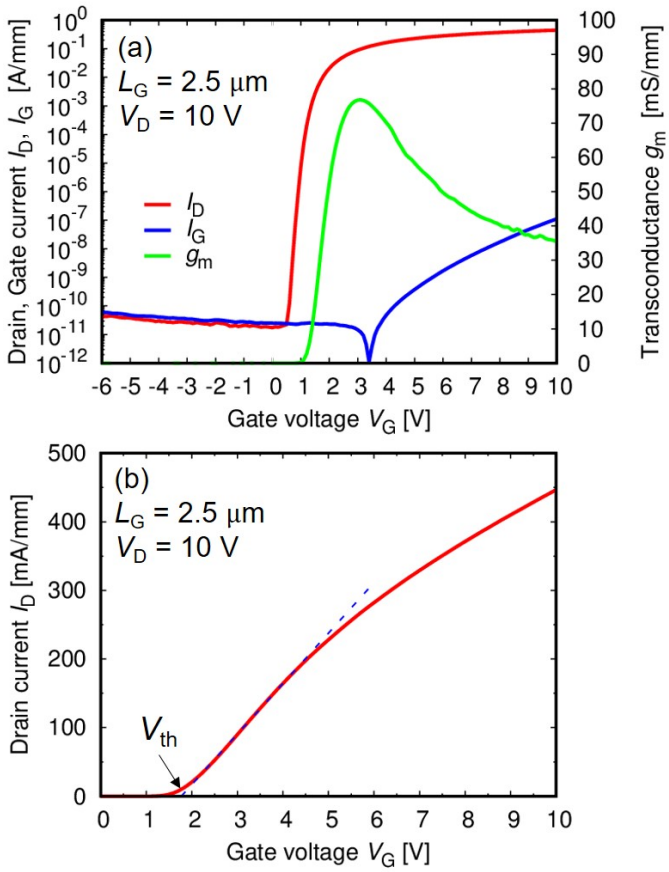

Figure 3.19: The transfer characteristics at V_D = 10 V of the partially-recessed Al-TiO/AlGaN/GaN MIS-FET.

device size is shown in Fig. 3.18, where $d_{AlGaN} \sim 4$ nm and $d_{ins} = 29$ nm.

The transfer characteristics are depicted in Fig. 3.19, showing the drain current I_D, the gate current I_G, and the transconductance g_m normalized by the channel width $W_G = 50$ μm. Figure 3.19(a) shows the transfer characteristics at $V_D = 10$ V, exhibiting a clear normally-off operation with a low leakage current $\sim 10^{-11}$ A/mm, a high on/off current ratio $\sim 10^{10}$, and the maximum of $g_m \simeq 80$ mS/mm. The threshold voltage is estimated to be 1.7 V by linear fitting of I_D as a function of V_G shown in Fig. 3.18(b), being consistent with the estimation from the C-V_G characteristics. We also check the hysteresis of the MIS-FET by measure I_D-V_G characteristics for the voltage sweep of $V_G = 0 \rightarrow +10$ V, $+10 \rightarrow -6$ V, and $-6 \rightarrow +10$ V, as shown in Fig. 3.20. There is almost no hysteresis for positive voltage applications in the range of $V_G \leq +10$ V. On the other hand, the negative voltage application down to $V_G = -6$ V leads to a negative

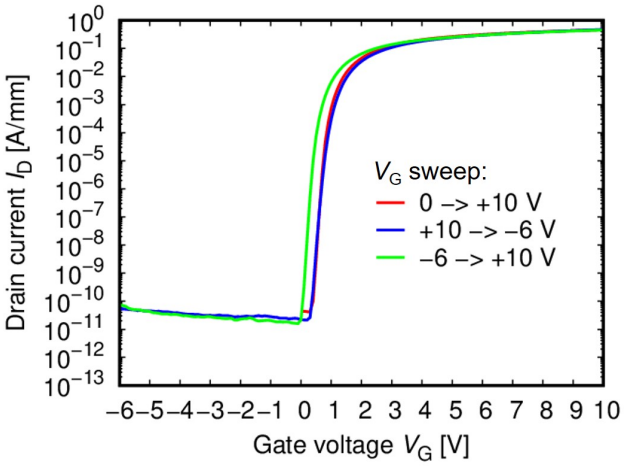

Figure 3.20: I_D-V_G characteristics depending on the voltage sweep.

threshold voltage shift of $\lesssim 0.5$ V. The output characteristics shown in Fig. 3.21 exhibits I_D as high as ~ 450 mA/mm, and a low on-resistance of 9.5 Ω·mm.

We calculate the sub-threshold swing $SS = [\partial(\log I_D)/\partial V_G]^{-1}$ and plot SS as functions of V_G and I_D for $V_D = 1$, 3, and 10 V in Fig. 3.22(a) and (b), respectively. We find a negative threshold voltage shift owing to the effect of drain-induced barrier lowering, although the effect is rather small ($\Delta V_{th} \simeq 0.5$ V). On the other hand, we observe excellent sub-threshold characteristics with the minimum

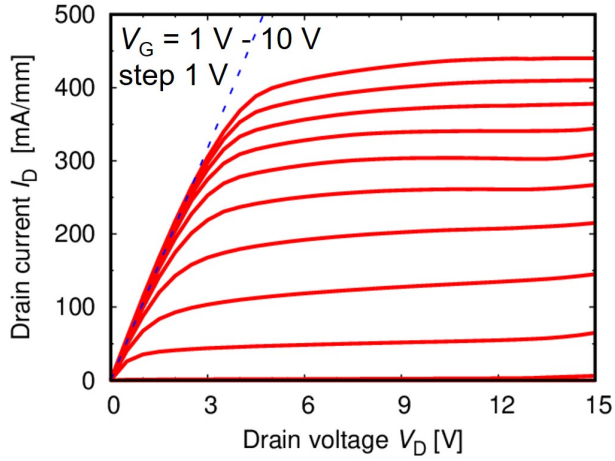

Figure 3.21: The output characteristics of the partially-recessed AlTiO/AlGaN/GaN MIS-FET. The gate voltage ranges from $V_G = 1 \rightarrow +10$ V with a step of 1 V.

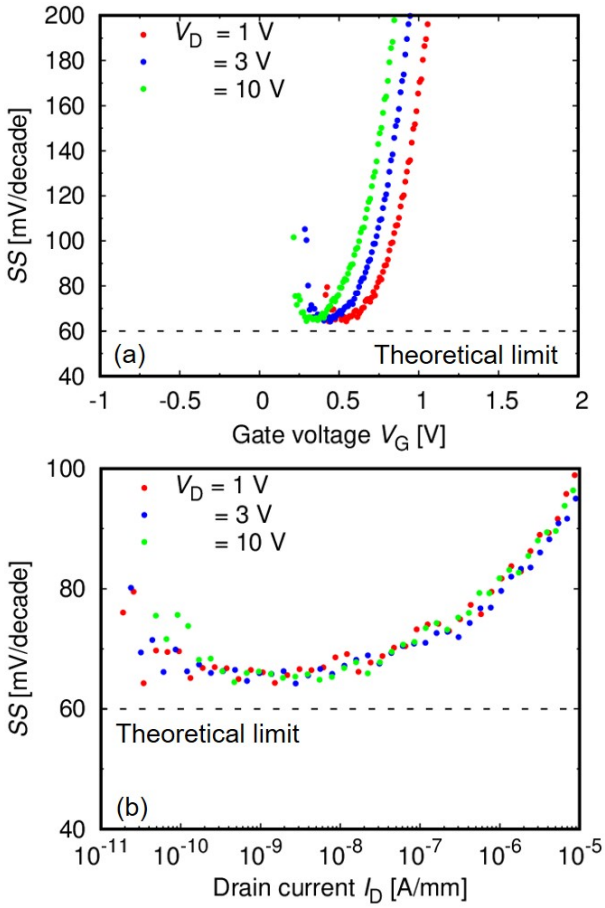

Figure 3.22: The sub-threshold swing $SS = [\partial(\log I_D)/\partial V_G]^{-1}$ as functions of (a) V_G and (b) I_D for $V_D = 1,\ 3$, and 10 V. The black dotted line shows the theoretical limit of 60 mV/decade.

$SS \sim 65$ mV/decade, which approaches the theoretical limit (60 mV/decade, plotted as the black dotted line) for a wide range of I_D.

The FET channel field mobility under the gate is usually calculated by

$$\mu = \frac{L_G}{CV_D}\frac{\partial I_D}{\partial V_G}. \tag{3.2}$$

However, based on a FET equivalent circuit shown in Fig. 3.23, the effects of the source resistance R_S and the drain resistance R_D must be taken into account. The channel field mobility under the gate should be obtained by

$$\mu = \frac{L_G}{CV_{D0}}\frac{\partial I_D}{\partial V_{G0}}, \tag{3.3}$$

where $V_{D0} = V_D - I_D(R_S + R_D)$, and $V_{G0} = V_G - I_D R_S$. The source resistance R_S and the drain resistance R_D are calculated from the contact resistance R_c and the

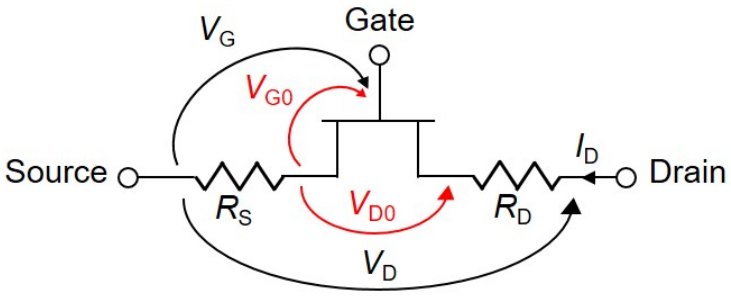

Figure 3.23: The equivalent circuit of the FET.

sheet resistance ρ_{sh} for the non-recessed area, by using

$$\begin{cases} R_S = R_c + \rho_{sh} \times L_{GS} \\ R_D = R_c + \rho_{sh} \times L_{GD} \end{cases}, \tag{3.4}$$

where L_{GS} and L_{GD} are the gate-source and gate-drain distance, respectively. Figure 3.24 shows the transfer length method (transmission-line model, TLM) characteristics for the non-recessed area. From the measurements, we estimate $R_c \simeq 1.2\ \Omega$·mm and $\rho_{sh} \sim 900\ \Omega/\square$. Thus, as shown in Fig. 3.25, we obtain the channel field mobility μ under the recessed-gate as a function of V_G for $V_D \leq 0.1$ V. We observe a maximum $\mu \simeq 730\ \mathrm{cm^2/V \cdot s}$, which is rather high as a channel field mobility of gate-recessed GaN-based MIS-FETs [89]. However, we observe a decrease in μ-V_G relation, which is similar to the decrease in g_m-V_G relation for

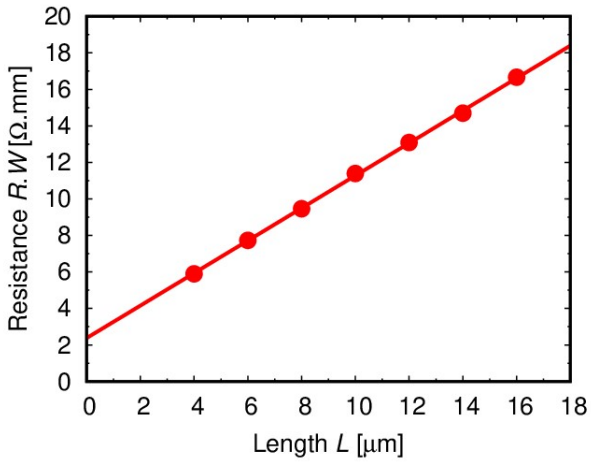

Figure 3.24: TLM measurements in the non-recessed area of the MIS-FET.

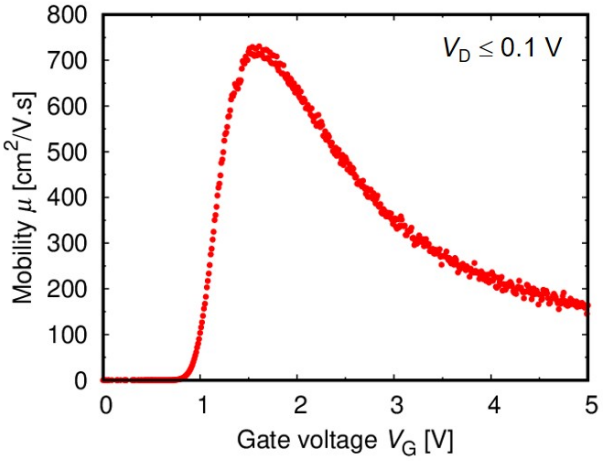

Figure 3.25: The channel electron mobility μ under the recessed gate as a function of V_G for $V_D \leq 0.1$ V.

high V_G, which can be attributed to interface states impeding the gate-control efficiency [44]. This suggests that the remaining AlGaN thickness ~ 4 nm is not enough to avoid degradation in the recessed channel. Therefore, if we can suppress the positive interface fixed charge density more and increase the remaining AlGaN thickness, the channel electron transport properties can be improved significantly.

Figure 3.26 compares V_{th} of the partially-recessed AlGaN/GaN MIS-FETs as function of the remaining AlGaN thickness between this work and other researches,

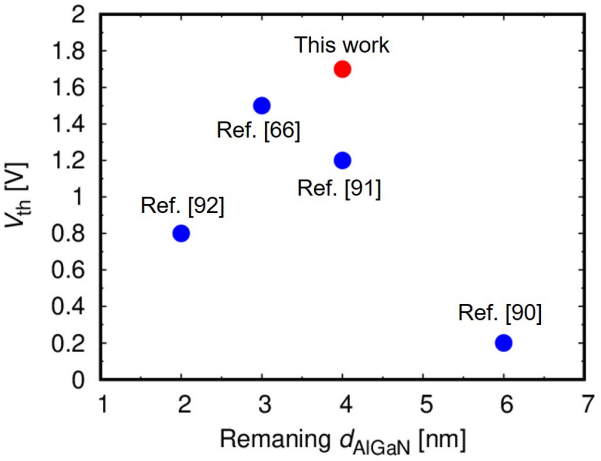

Figure 3.26: V_{th} of the partially-recessed AlGaN/GaN MIS-FETs.

showing that our device can achieve high threshold voltage while having rather thick remaining AlGaN layer. In order to show the advantages of combining interface charge engineering and the partial recess method, we compare the typical device parameters between our device with other gate-recessed AlGaN/GaN MIS-FETs as shown in Table 3.1. We can see that while our MIS-FET can have similar threshold voltage as other devices, its transport properties are much more superior than others', in particular channel electron mobility, subthreshold swing, and on-resistance. Moreover, owing to interface charge engineering, we obtain a low-density-positive-fixed-charge AlTiO/AlGaN interface, thus higher threshold voltages can be simply obtained by increasing the insulator thickness. In conclusion, employing interface charge engineering in partially-recessed AlGaN/GaN MIS-FETs is advantageous to realize high-threshold voltage normally-off operations with good channel transport properties.

Table 3.1: Comparison of typical device parameters between our device with other gate-recessed AlGaN/GaN MIS-FETs.

Gate insulator	d_{AlGaN} [nm]	L_{SD} [μm]	V_{th} [V]	R_{on} [Ω·mm]	max I_{D} [mA/mm]	$I_{\mathrm{on}}/I_{\mathrm{off}}$ ratio	max g_{m} [mS/mm]	min SS [mV/decade]	max μ [cm^2/V·s]	Reference
AlTiO	**$\sim$ 4**	**5**	**1.7**	**9.5**	**450**	**$\sim 10^{10}$**	**80**	**65**	**730**	**This work**
Al_2O_3	~ 6	15	0.3	9.0	660	$\sim 10^9$	207	112	1050	[90]
Si_3N_4	~ 4	23	1.2	12.2	430	$\sim 10^{10}$	65	–	200	[91]
Al_2O_3	~ 3	8	1.5	5.2	690	$\sim 10^8$	165	–	190	[66]
SiN_x	~ 2	14	0.8	10.0	590	$\sim 10^9$	101	–	180	[92]
Al_2O_3	0 (FR)	3	2.0	4.0	800	$\sim 10^{11}$	175	90	–	[67]
HfSiO	0 (FR)	30	2.1	11.5	490	$\sim 10^{10}$	170	84	410	[93]
SiN_x	0 (FR)	17	2.4	13.2	600	$\sim 5 \times 10^8$	150	97	160	[94]
Al_2O_3	0 (FR)	6	2.8	10.0	590	$\sim 10^9$	107	148	150	[95]
Al_2O_3	0 (FR)	6	3.2	8.8	660	$\sim 10^{10}$	99	–	180	[96]
Al_2O_3	0 (FR)	8.5	7.6	19.5	360	$\sim 3 \times 10^8$	–	–	70	[88]

FR: fully recessed

Chapter 4

Low-frequency noise characterization for AlTiO/AlGaN/GaN MIS devices

4.1 Introduction to low-frequency noise

Noise is the random deviations of a quantity around its mean value. In science and engineering, understanding noise is important because noise directly affects the device/instrument performances by limiting the measurement accuracy and the magnitude of detectable signals. In electronic circuits, currents and voltages are not constant but randomly fluctuate around the mean values due to the fluctuations of the carrier transport properties (velocity, concentration, and so on). These fluctuations generate noise, which are different from external disturbances. The disturbances can be completely removed by setting a good/proper measurement system, whereas noise can only be reduced partially (not fully) by circuit designs.

Noise is a stochastic (random) process, and is usually expressed by the power spectral density (PSD) $S(f)$ as a function of frequency f. When a physical quantity x shows noise, we may expressed it as a function of time t as

$$x(t) = \langle x \rangle + \delta x(t), \tag{4.1}$$

where the symbol $\langle\rangle$ denotes averaging over a long enough time interval, and $\delta x(t)$ is the fluctuation of x, which is given by

$$[\delta x(t)]^2 = \langle (x - \langle x \rangle)^2 \rangle = \langle x^2 \rangle - \langle x \rangle^2. \tag{4.2}$$

We then can define a correlation function $\psi_x(t_1, t_2)$ given by

$$\begin{aligned} \psi_x(t_1, t_2) \equiv \langle \delta x(t_1) \delta x(t_2) \rangle &= \langle x(t_1) x(t_2) \rangle - \langle x(t_1) \rangle \langle x(t_2) \rangle \\ &= \lim_{N \to \infty} \frac{1}{N} \sum_{i=1}^{N} \delta x_i(t_1) \delta x_i(t_2). \end{aligned} \tag{4.3}$$

In a stationary system, the correlation function remains invariable if both instants, t_1 and t_2, are shifted identically, thus ψ_x depends only on the difference $t_1 - t_2$. Moreover, the correlation function can also be determined by averaging over a sufficiently long record of the random process $x(t)$ in one system, i.e. by averaging over a long enough time of measurement t_m:

$$\psi_x(t_1 - t_2) \equiv \overline{\delta x(t_1) \delta x(t_2)} = \lim_{t_m \to \infty} \frac{1}{t_m} \int_{-t_m/2}^{t_m/2} \delta x(t_1 + t) \delta x(t_2 + t)\, dt. \tag{4.4}$$

According to Wiener-Khintchine theorem, the PSD of the quantity x is given by [97]

$$S_x(f) = 2 \int_{-\infty}^{+\infty} \psi_x(t_1 - t_2) e^{j\omega(t_1 - t_2)}\, d(t_1 - t_2), \tag{4.5}$$

where x can be electrical resistance R, current I, or voltage V. If we choose $t_1 = t,\ t_2 = 0$, and $\omega = 2\pi f$, we have:

$$\begin{aligned} S_x(f) &= 2 \int_{-\infty}^{+\infty} \psi_x(t) e^{2j\pi f t}\, dt \\ \psi_x(t) &= \langle \delta x(0) \delta x(t) \rangle. \end{aligned} \tag{4.6}$$

Let us discuss the properties of the PSD and the correlation function. First of all, if we set $t_m/2 = T$, we can rewrite Eq. (4.4) as

$$\psi_x(t) = \frac{1}{2T} \int_{-T}^{+T} \delta x(\tau) \delta x(t + \tau)\, d\tau, \tag{4.7}$$

thus

$$\begin{aligned} \psi_x(-t) &= \frac{1}{2T} \int_{-T}^{+T} \delta x(\tau) \delta x(-t + \tau)\, d\tau \\ &= \frac{1}{2T} \int_{-T}^{+T} \delta x(s + t) \delta x(s)\, ds, \text{ by setting } \tau - t = s \\ &= \psi_x(t). \end{aligned} \tag{4.8}$$

Hence, $\psi_x(t)$ is an even function, leading to $S_x(f)$ being also a even function, because

$$\begin{aligned} S_x(-f) &= 2\int_{-\infty}^{+\infty} \psi_x(t) e^{-2j\pi ft}\, dt \\ &= -2\int_{+\infty}^{-\infty} \psi_x(-s) e^{2j\pi fs}\, ds, \text{ by setting } -t = s \\ &= 2\int_{-\infty}^{+\infty} \psi_x(s) e^{2j\pi fs}\, ds \\ &= S_x(f). \end{aligned} \tag{4.9}$$

Therefore, if we carry out inverse Fourier transformation of Eq. (4.6), the correlation function becomes

$$\begin{aligned} \psi_x(t) &= \frac{1}{2}\int_{-\infty}^{+\infty} S_x(f) e^{-2j\pi ft}\, df \\ &= \int_{0}^{+\infty} S_x(f) e^{-2j\pi ft}\, df. \end{aligned} \tag{4.10}$$

At $t = 0$, we have

$$\begin{aligned} \psi_x(0) &= \int_{0}^{+\infty} S_x(f)\, df \\ &= \langle [\delta x(0)]^2 \rangle = (\delta x)^2, \end{aligned} \tag{4.11}$$

where $(\delta x)^2$ is the observable fluctuation of the physical quantity x that can be measured.

Depending on the frequency f, noise can be classified as (1) thermal noise whose PSD is independent of f, caused by thermal motion of carriers (it has other names such as Johnson-Nyquist, white, or system floor noise); (2) shot noise caused by some discrete physical process; (3) generation-recombination (g-r) noise whose PSD depending of f by a Lorentzian function, caused by capture and emission of traps; (4) $1/f$ noise (Flicker noise) whose PSD is inversely proportional to the frequency. These types are illustrated in Fig. 4.1. Low-frequency noise is the noise at low frequencies, usually below 10 kHz. In this range, g-r noise and $1/f$ noise dominate the PSD. In particular, the $1/f$ noise PSD always increases with a decrease in the frequency, thus it becomes the most significant noise source at very low frequencies. Therefore, the term "low-frequency noise" usually denotes

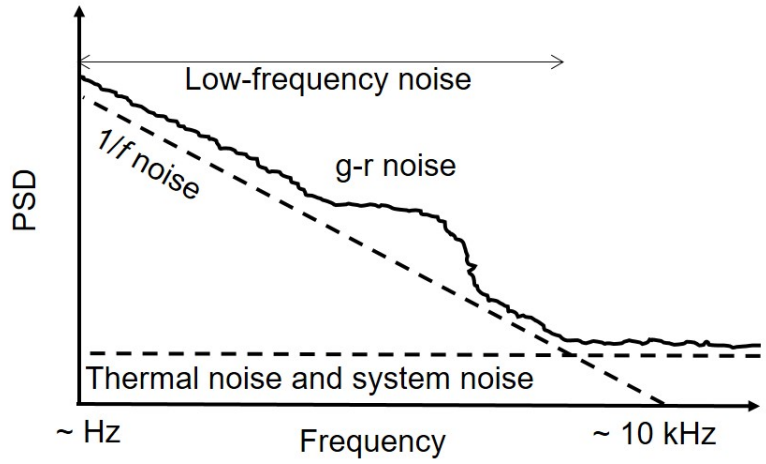

Figure 4.1: Noise power spectral density (PSD) as a function of the frequency f.

$1/f$ noise, whose PSD is given by the form [98, 99], for example,

$$S_I(f) = \frac{K.I^{\alpha}}{f^{\beta}}, \tag{4.12}$$

where I is the current, K is a constant, α is the current exponent and usually equals to 2, and β is the proportional constant and usually close to 1. This formula can be applied to other physical quantity like resistance R or voltage V by replacing I by R or V.

Although the thermal noise is fully elucidated [100, 101], the low-frequency noise including $1/f$ noise and bump characteristics remains as controversies [98, 102–104] even it has been discovered for a long time [105, 106]. For example, one simple question of the lower limit of $1/f$ noise still remains. The lowest measured frequency showing $1/f$ behavior is in order of 10^{-7} Hz [102], but we cannot conclude anything yet. Because noise always exists inside electronic devices and circuits, understanding the noise mechanism is of crucial importance for the device development. The signal-to-noise ratio (SNR), which indicates the reliability of the signal processing of a device (the higher the ratio, the better the signal), becomes smaller when the device size reduces [68], hence the $1/f$ noise becomes a major concern for nano-device technologies. Therefore, understanding and overcoming the $1/f$ problems are important for the future of electronic devices and circuits.

It has been shown in the previous chapter that employing AlTiO with $x/(x+$

$y) = 0.73$ composition can significantly suppress the interface fixed charge density at AlTiO/etched-AlGaN interface to realize normally-off operations. Therefore, in this chapter, we investigated the low-frequency noise in non-recessed and partially-recessed AlTiO/AlGaN/GaN MIS devices with $x/(x + y) = 0.73$ composition in order to understand AlTiO/AlGaN interface and improve device performances.

4.2 Low-frequency noise models

First of all, if we consider the current I flowing in a conductor is proportional to the total carrier number N and the average mobility μ, i.e.

$$I \propto N\mu, \tag{4.13}$$

hence we have

$$\Delta I \propto \Delta N\mu + N\Delta\mu + O(N, \mu). \tag{4.14}$$

Therefore, fluctuations in the current ΔI can be attributed to fluctuations in the carrier number ΔN and/or fluctuations in the mobility $\Delta\mu$. This is the main controversy in the origin of $1/f$ noise: fluctuations in the carrier number or the mobility?

Many models have been proposed to adapt the measurement data. One of these is Hooge model, which introduces a empirical formula for the resistance fluctuations on 1969 [107]

$$\frac{S_R(f)}{R^2} = \frac{\alpha_{\mathrm{H}}}{Nf}, \tag{4.15}$$

where $\alpha_{\mathrm{H}} \simeq 2 \times 10^{-3}$ is a universal constant. According to Eq. (4.15), the $1/f$ noise PSD depends only on the carrier number N. However, other data showed the invalidity of Eq. (4.15). Therefore, a modified formula in a more general form has been proposed [99]

$$\frac{S_x(f)}{x^2} = \left(\frac{\mu}{\mu_{\mathrm{ph}}}\right)^2 \frac{\alpha_{\mathrm{H}}}{Nf}, \tag{4.16}$$

where μ_{ph} is the mobility due to phonon scattering, x can be any physical quantity (R, V, or I), and α_{H} is not a universal constant. Although Eq. (4.16) is a empirical formula, it suggests that the origin of the $1/f$ noise is attributed to the mobility

fluctuations due to the phonon scattering. A strong evidence to that conclusion is the relation $\alpha_{\mathrm{H}} \propto \mu^2$ [98, 108].

On the other hand, McWhorter model considers the carrier-number fluctuations due to trapping/detrapping of carriers in traps located at a distance from the oxide insulator/semiconductor interfaces to be the noise source [99, 109]. The noise then will have the Lorentzian form [110]

$$S_n(f) = \langle (\Delta n)^2 \rangle \frac{4\tau}{1 + (2\pi f \tau)^2}, \tag{4.17}$$

where τ is the lifetime of the free-carrier-number fluctuation Δn. The $1/f$ behavior in the PSD is due to the superposition of Loretzian spectra [110]

$$S(f) \propto \int_0^\infty g(\tau) \frac{4\tau \overline{(\Delta n)^2}}{1 + (2\pi f \tau)^2}, \tag{4.18}$$

where $g(\tau)$ is a statistical weight. If we assume a non-uniform trap distribution with $g(\tau) \propto 1/\tau$, the noise PSD can be divided into three regions given by

$$S(f) \propto \begin{cases} \text{constant} & \text{for } 2\pi f \ll 1/\tau_1 \\ 1/f & \text{for } 1/\tau_1 < 2\pi f < 1/\tau_2 \\ 1/f^2 & \text{for } 2\pi f \gg 1/\tau_2 \end{cases}, \tag{4.19}$$

where τ_1 and τ_2 are the time constants determined by the smallest and largest distances of tunneling, respectively. The McWhorter model suggests that the $1/f$ noise comes from the fluctuations of the carrier number by the generation-recombination of electrons from the traps in the interface or surface states. The noise PSD spectra given by McWhorter model differ from these of Hooge model at the very low frequency, the spectra is similar to white noise.

In addition to these models, there are other models having been proposed to explain the $1/f$ noise such as temperature fluctuation model by Voss and Clarke [111] or by Dutta and Horn [102, 112], quantum mechanic model by Handel [113], and so on. We realize that these models are not always true because of various noise mechanisms. In reality, $1/f$ noise depends on the device dimensions as well as its materials [104]. Therefore, for $1/f$ noise characterization, a proper model should be carefully chosen, or even multiple models should be taken into account.

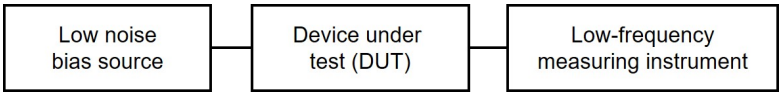

Figure 4.2: The configuration of low-frequency noise measurement system.

4.3 Low-frequency noise measurement system

A measurement system for low-frequency noise usually consists of three main component as shown in Fig. 4.2. The low-noise bias source is used to bias the measured devices which usually employs a battery. The purpose of using a battery is to avoid the noise from AC power supply, for example peaks at 60, 120, and 240 Hz. For measurements of three-terminal devices, we use a combination of a source measurement unit (SMU) and a low-pass filter (LPF) to bias third terminal (i.e. the gate of transistors). The LPF role is to suppress low-frequency noise from the SMU, which can affect the measured signals. Hence the LPF must have a cut-off frequency lower than the limit of the measured frequency range. In this work, the low-frequency noise measurement is from 1 Hz to 10 kHz, so the employed LPF should have the cut-off frequency below 0.1 Hz. Furthermore, since the LPF must not give additional noise to the device signals, it should be a passive type without amplification functions. The low-frequency measuring instrument is used to detect and analyze the signals, and is a combination of a low-noise current pre-amplifier (LNA) and a signal dynamic analyzer (DSA). The LNA is used to amplify the small signals before they enter the DSA. The detailed configuration of the measurement system for two-terminal (2T) device-under-test (DUT) such as diodes, and three-terminal (3T) DUT such as transistors are shown in Fig. 4.3(a) and (b), respectively. The difference between two configurations comes from the low-noise bias source. For 2T measurement system, the device is biased directly by using battery power supply of the LNA. The bias by LNA input is based on the virtual ground, which is a property of operational-amplifier components of the LNA. On the other hand, for 3T measurement system, LNA input is used to bias second terminal (the drain of transistors) and a combination of a SMU and a LPF is used to bias third terminal (the gate of transistors). Each component will be discussed in the following.

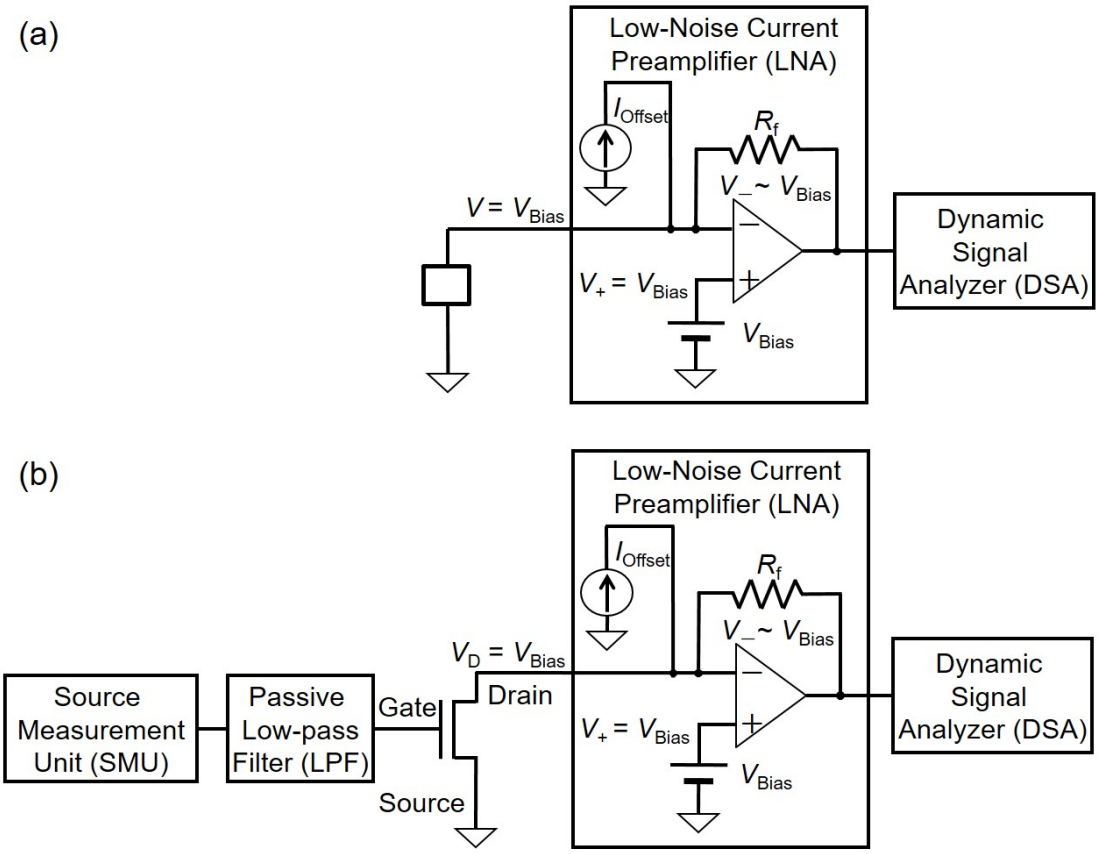

Figure 4.3: Low-frequency noise measurement system for (a) 2T DUTs and (b) 3T DUTs.

Low-pass filter

The LPF was made from a cement resistor of 10 kΩ and two film capacitors of 150 μF by our laboratory. An image of the LPF is shown in Fig. 4.4(a), and its circuit is schematically depicted in Fig. 4.4(b). When the LPF is connected to the gate of a transistor, the connection circuit will be as in Fig. 4.5. When a gate voltage V_G is applied, a gate leakage current I_G exists, so a voltage drop ΔV_G due to resistance R appears, and decreases the actual applied gate voltage V'_G. To reduce ΔV_G, the resistance must not be large. However, for LPF, the cut-off frequency is given by

$$f_T = \frac{1}{2\pi RC} \leq 0.1 \text{ Hz}, \tag{4.20}$$

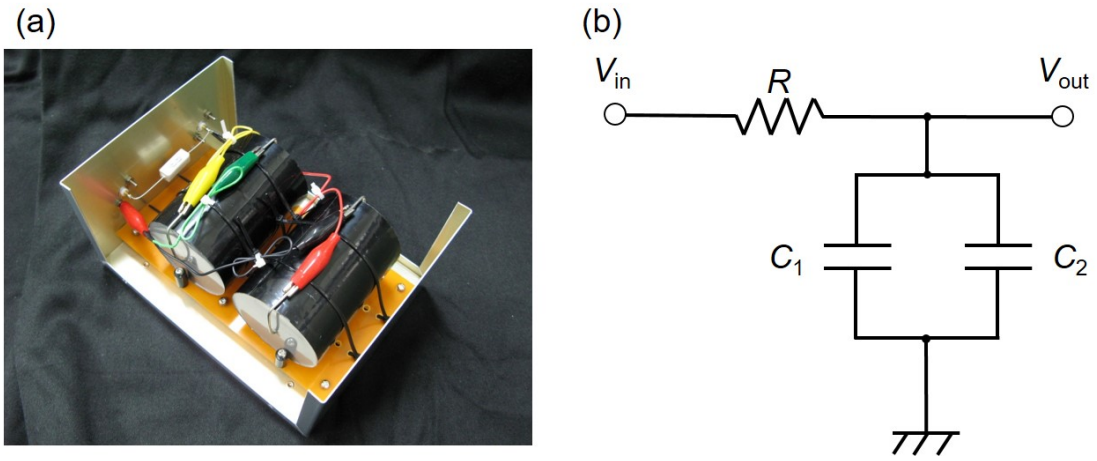

Figure 4.4: (a) An image of the LPF and (b) its circuit.

so small R leads to large C. A large-capacitance capacitor is not desirable due to its large leakage and size. Therefore, R cannot be arbitrarily small. Considering that in our measurements, the transistors usually have a gate leakage current of $\sim 10^{-6}$ A, and the gate voltages in order of 1 V, the resistance should be

$$R = \frac{\Delta V_{\mathrm{G}}}{I_{\mathrm{G}}} \ll \frac{V_{\mathrm{G}}}{I_{\mathrm{G}}} \sim 1\ \mathrm{M\Omega}. \tag{4.21}$$

Hence, we picked $R \simeq 10$ kΩ. According to Eq. (4.20), the corresponding C is ~ 300 μF. The cut-off frequency of the LPF is

$$f_{\mathrm{T}} = \frac{1}{2\pi RC} = \frac{1}{2\pi \times 10\ \mathrm{k\Omega} \times 300\ \mu\mathrm{F}} \simeq 0.05\ \mathrm{Hz}, \tag{4.22}$$

which is low enough for the measurement.

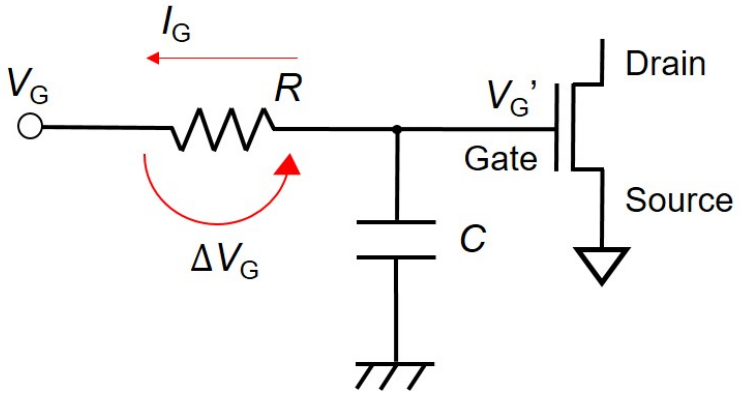

Figure 4.5: A circuit of the LPF and the gate of a FET in series connection.

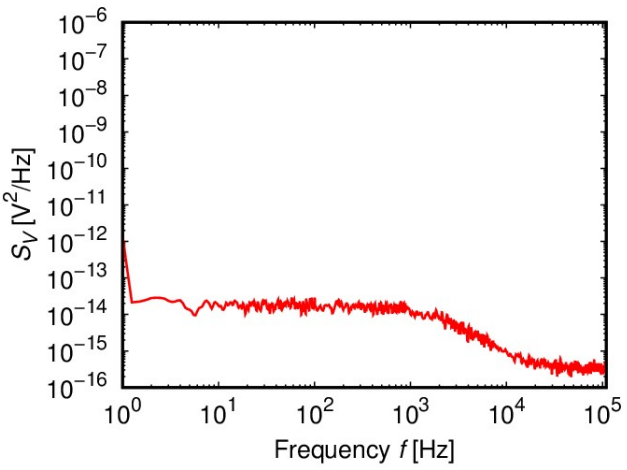

Figure 4.6: Background noise of the 35670A DSA.

Dynamic signal analyzer

We used a dynamic signal analyzer (DSA) type 35670A made by Agilent Technologies. The Agilent 35670A DSA is a versatile Fast-Fourier Transformation (FFT) analyzer with built-in source for general spectrum and network analysis. The 35670A DSA detects the voltage noise signal in the time domain, and converts it to frequency domain by using the FFT function. To obtain accurate results, the measurements should be repeated many times, and the results are averaged. Usually the averaging number is set to 30.

The DSA is a signal analyzer, so its background noise will set the lower limit for the measured signal. Figure 4.6 shows the background noise of the DSA, which is in order of 10^{-14} V^2/Hz. This is also the lower limit for the noise measurement. Therefore, the measured signals should be several order higher than this value to remove the effect the background noise. The main characteristics of the 35670A DSA are listed below.

- Frequency span: 98 mHz - 51 kHz.
- Frequency resolution: 400, 800 and 1600 lines.
- Input impedance: 1 MΩ.
- Output mode: voltage noise.
- Analysis mode: FFT.

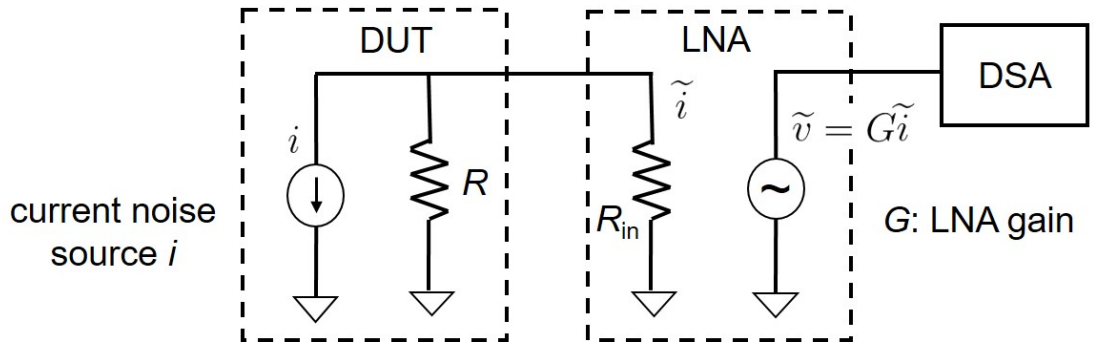

Figure 4.7: Equivalent circuit of DUT, LNA and DSA in series connection.

- Dynamic range: 90 dB, accuracy: 0.15 dB.

Low-noise current pre-amplifier

The low-noise current pre-amplifier is used to amplify the small signal before it enters DSA. The input of LNA is current noise signal S_I and the output is voltage noise signal S_V with an amplification. The output signal is amplified by the factor called sensitivity, or s_{LNA} by the formula

$$S_V[\mathrm{V}^2/\mathrm{Hz}] = s^2_{\mathrm{LNA}}[\mathrm{V}^2/\mathrm{A}^2] \times S_I[\mathrm{A}^2/\mathrm{Hz}]. \tag{4.23}$$

In order to choose a proper sensitivity for a measurement, first we need to examine how the amplification works by considering an equivalent circuit of DUT, LNA and DSA as shown in Fig. 4.7. The DUT with a resistance R will have its current noise signal i transferred to the LNA, and the current signal after the LNA input is $\tilde{i}$, which is given by

$$\tilde{i} = \frac{R}{R + R_{\mathrm{in}}} i = \frac{1}{1 + R_{\mathrm{in}}/R} i, \tag{4.24}$$

where R_{in} is the input resistance determined by the choice of sensitivity. The voltage signal at the LNA output is given by

$$\tilde{v} = G\tilde{i} = G\frac{1}{1 + R_{\mathrm{in}}/R} i, \tag{4.25}$$

where G is the LNA gain (or the sensitivity). We realize that

$$\tilde{v} = G\frac{1}{1 + R_{\mathrm{in}}/R} i \simeq Gi \Leftrightarrow R_{\mathrm{in}} \ll R. \tag{4.26}$$

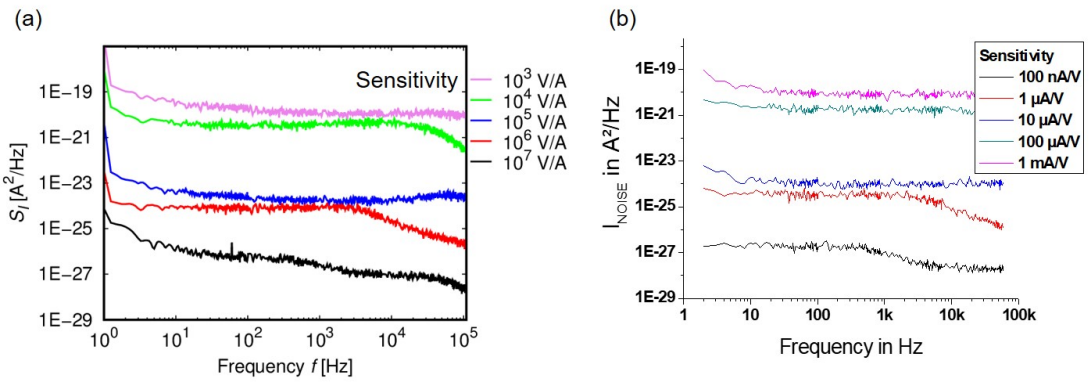

Figure 4.8: (a) Measurement system background noise and (b) its reference in [114] for each sensitivity.

To ensure the accuracy of the measurement, Eq. (4.26) should be guaranteed. For example, if we measure the DUT with $R = 200\ \Omega$, R_{in} should be $1\ \Omega$, corresponding to the sensitivity of 10^3 or 10^4 V/A. The specifications of the LNA are given below.

- Gain mode: low-noise.
- Maximum off-set current: 5 mA (down to 1 pA).
- Maximum bias voltage: 5 V (down to 1 mV).
- Frequency range: DC-1 MHz.
- Sensitivity (input resistance): 10^3, 10^4 V/A (1 Ω); 10^5, 10^6 V/A (100 Ω); 10^7, 10^8 V/A (10 kΩ); 10^9-10^{12} V/A (1 MΩ).

Depending on the choice of sensitivity, the lower limit of the background noise is different. Figure 4.8 compares the measurement background noise with the reference for each sensitivity, showing almost no differences, except for the very high sensitivity.

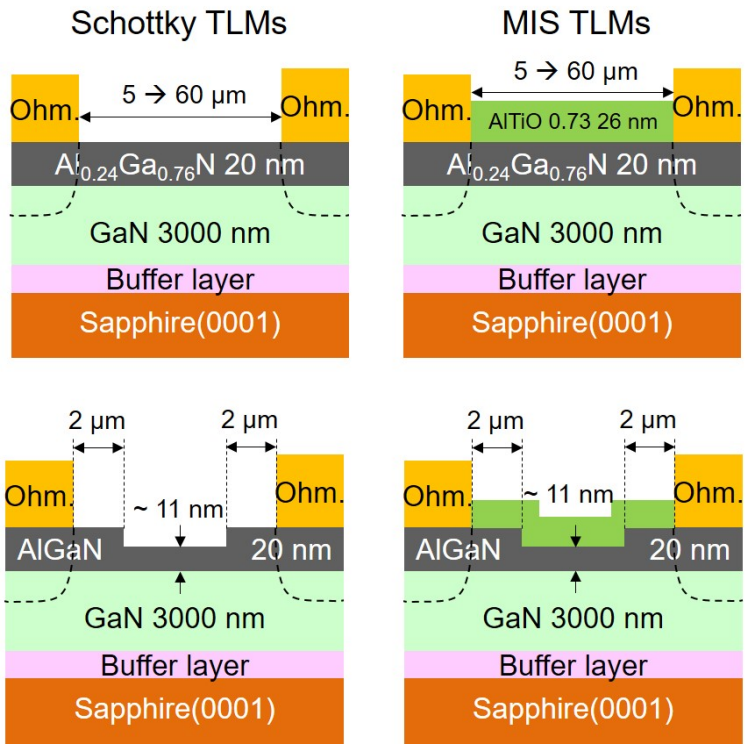

Figure 4.9: The Schottky and MIS transmission-line models (TLMs) dimensions used for low-frequency noise characterization. The width of the TLMs is 50 μm.

4.4 Low-frequency noise characterization of AlGaN/GaN-based ungated two-terminal devices

In this section, we investigated low-frequency noise in AlGaN/GaN-based ungated two-ternimal structures, which are AlTiO/AlGaN/GaN (MIS) and Schottky AlGaN/GaN transmission-line models (TLMs). Moreover, we also investigated low-frequency noise in the partially-recessed MIS and Schottky AlGaN/GaN TLMs. The devices dimensions are shown in Fig. 4.9. The thickness of the remaining AlGaN layer for the partially-recessed TLMs is $\sim$ 11 nm. For the non-recessed TLMs, the transfer length $L = 5 \rightarrow 60$ μm, whereas in the partially-recessed TLMs, the transfer length $L = 6 \rightarrow 56$ μm due to 4-μm non-recessed region.

Before carrying out low-noise frequency measurements, we calculated the resistance by I-V characteristics. Hence we can determine the off-set currents accord-

Table 4.1: Series resistance r_{ser} and sheet resistance ρ_{s} obtained from TLM characterization.

	r_{ser} [Ω·mm]	ρ_{s} [Ω/□]
$d_{\mathrm{AlGaN}} = 20$ nm	1.2	540
$d_{\mathrm{AlGaN}} = 11$ nm	2.4	650

ing to the applied bias voltages. Figure 4.10 shows the TLM characterization for the devices. We observe almost no differences between Schottky and MIS TLMs for a given AlGaN thickness, indicating that AlTiO deposition process does not affect the 2DEG. We summarize the results of the TLM characterization in Table 4.1, where series resistance r_{ser} is determined at $L = 0$, which is contact resistance in case of non-recessed TLMs, or the sum of contact resistance and access resistance in case of partially-recessed TLMs, and ρ_{s} is the sheet resistance.

Due to the small noise signals and the resistance of order 200 Ω, the measurements employed the largest magnification, i.e. the sensitivity of 10^3 V/A and the off-set currents from 3 mA to 5 mA. The bias voltages are set according to the corresponding resistance. The current noise PSD for each TLM structure are depicted in Fig. 4.11, where we show examples for the shortest and longest transfer length. We observe peaks at 30 and 45 Hz, owing to the self-heating problem of

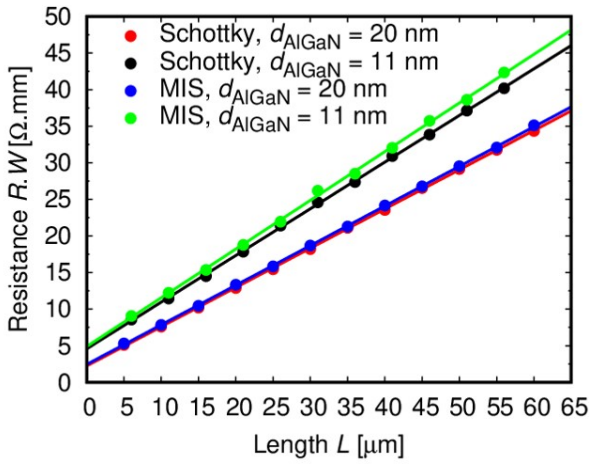

Figure 4.10: TLM characterization of the above devices.

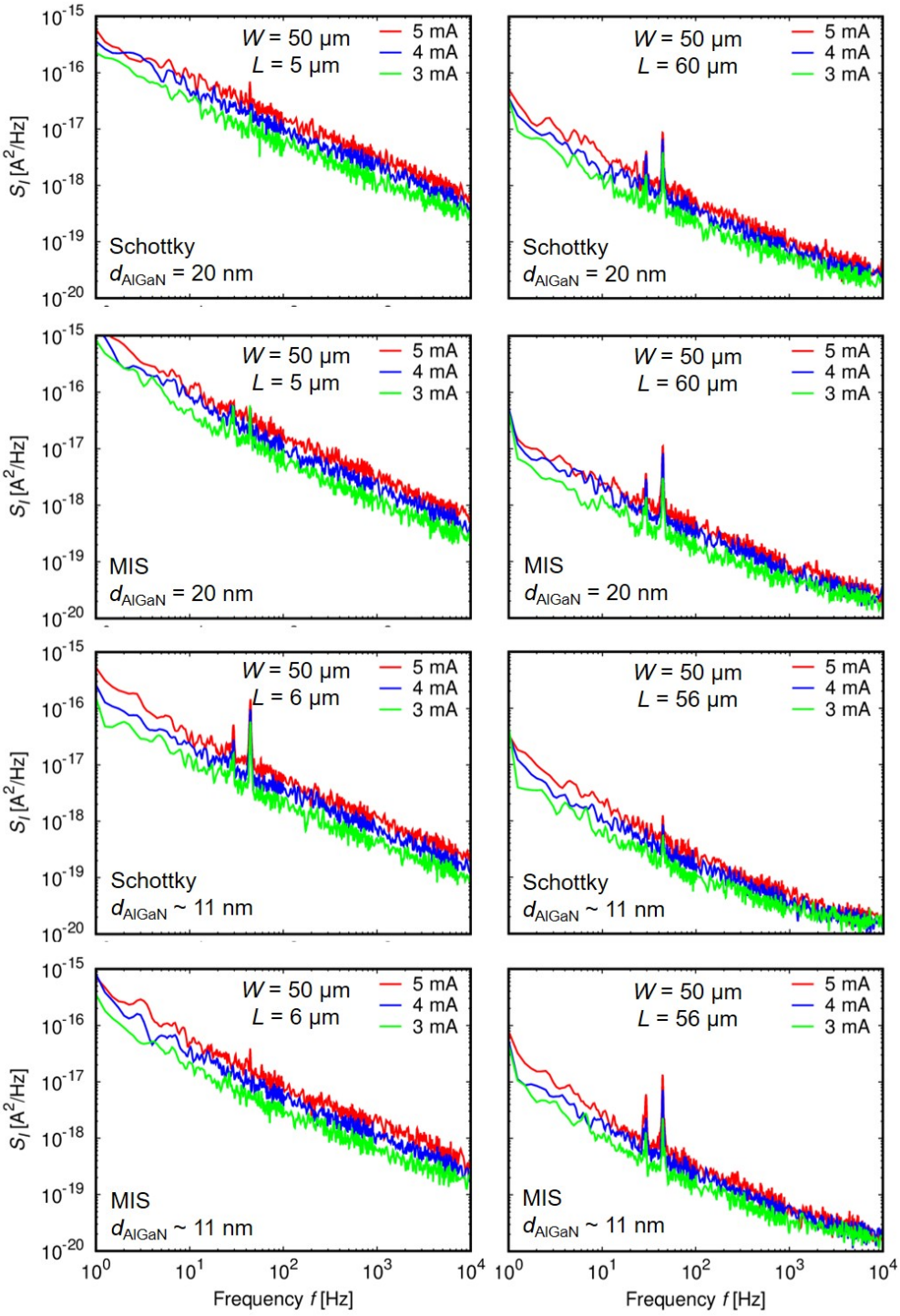

Figure 4.11: Examples of low-frequency spectra of the current noise of AlGaN/GaN-based ungated TLMs with the shortest and longest transfer length.

the DSA. No specific bumps or peaks owing to generation-recombination noise are observed.

Figure 4.12 illustrates S_I/I^2 as functions of f, showing a relation according to

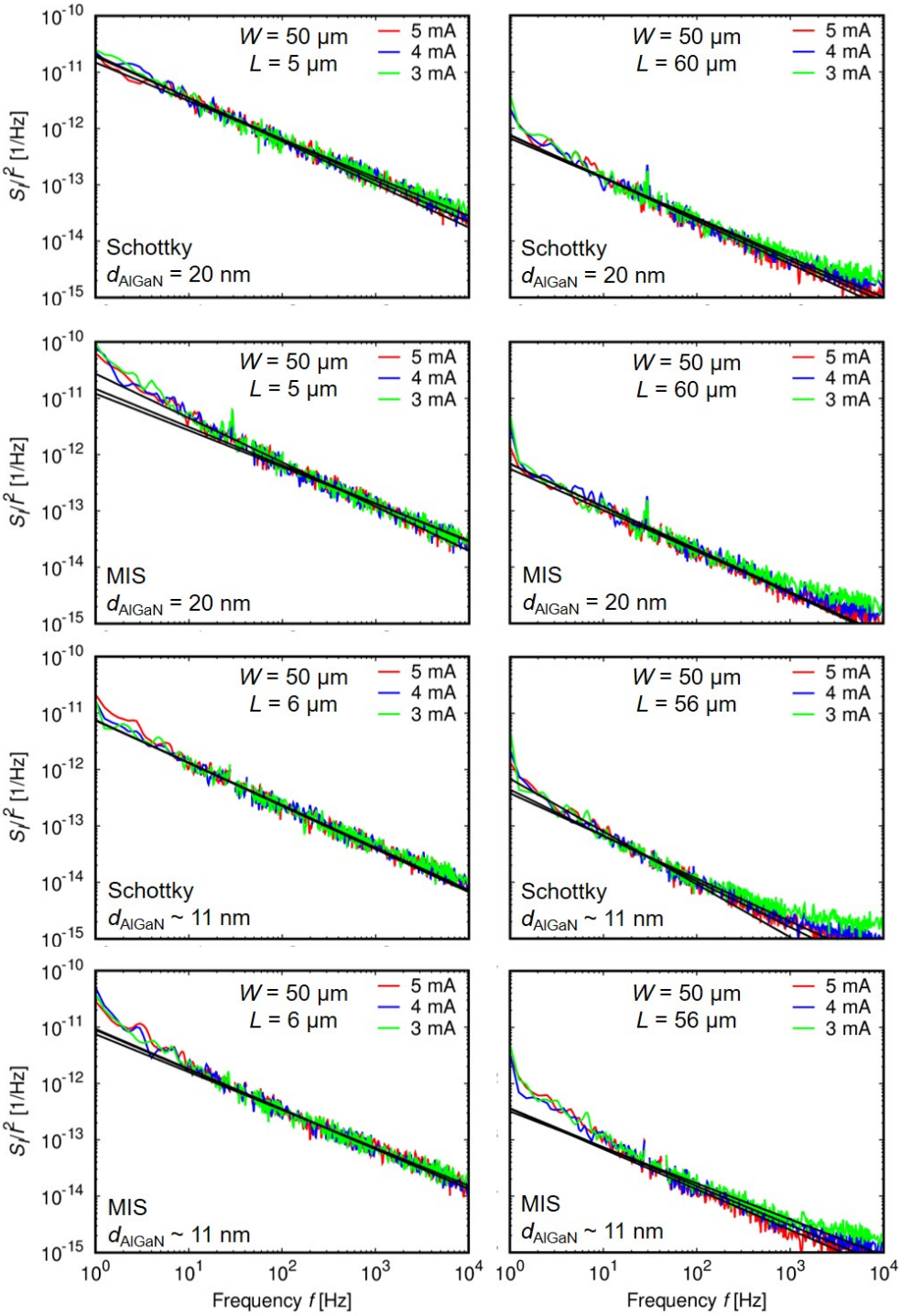

Figure 4.12: Examples of low-frequency spectra of the current noise of AlGaN/GaN-based ungated TLMs normalized by I^2 with the shortest and longest transfer length with the fitting lines based on Eq. (4.27).

the Hooge model

$$\frac{S_I}{I^2} = \frac{K}{f^\alpha}, \tag{4.27}$$

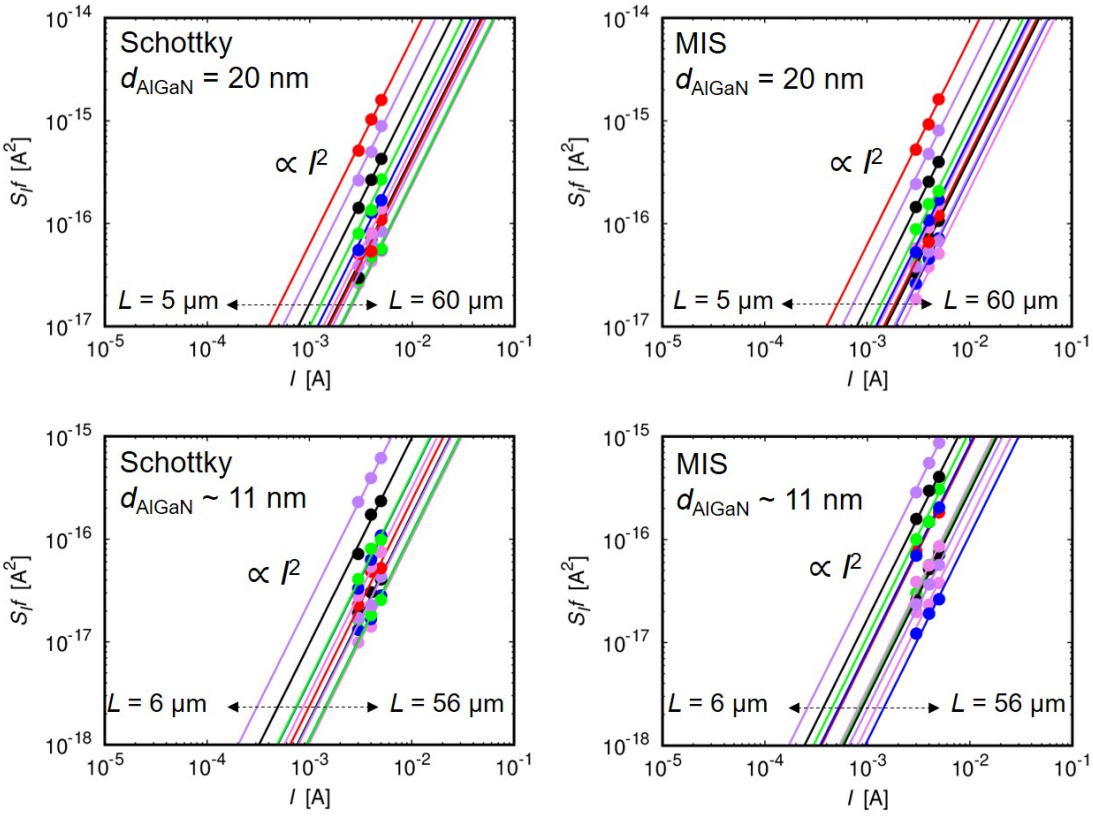

Figure 4.13: $S_I f$ as functions of the current I, showing a relation $S_I f \propto I^2$.

where $\alpha \simeq 0.8$ for our results. We have omitted the external noise peaks at 30 and 45 Hz, and fitted the equation from 10 Hz to 10 kHz, ignoring the frequency range less than 10 Hz due to measurement problem. Equation (4.27) indicates that $S_I f \propto I^2$. In order to clarify this conjecture, we plot $S_I f$ as functions of the current I for different L as shown in Fig. 4.13. This result confirms Eq. (4.27).

In order to analyze the results, first we accept the fact that the resistance of a semiconductor fluctuates with a $1/f$ spectrum. The resistance fluctuations can be measured as voltage fluctuations when a constant current is passed through or

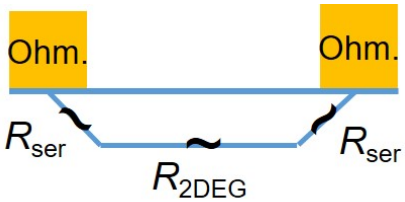

Figure 4.14: The measured TLM resistance can be consider as a series of resistors.

as current fluctuations when the voltage drop across the sample is constant:

$$\frac{S_R(f)}{R^2} = \frac{S_I(f)}{I^2} = \frac{S_V(f)}{V^2} = \frac{S_G(f)}{G^2}. \tag{4.28}$$

The derivation of this equation is given in Appendix C. Based on the transmission-line model, we can consider the measured resistance to be the sum of two resistors, the series resistor with resistance $2R_{\rm ser}$ and the 2DEG channel resistor with resistance $R_{\rm 2DEG}$, as shown in Fig. 4.14.

Now considering two resistors in series $R_{\rm A}$ and $R_{\rm B}$, we have the voltage drop $V = V_{\rm A} + V_{\rm B}$. The total noise PSD generated is given by (see Appendix C)

$$S_V = S_{V_{\rm A}}^{\rm A} + S_{V_{\rm B}}^{\rm B}, \tag{4.29}$$

or

$$\frac{S_I}{I^2}V^2 = \frac{S_I^{\rm A}}{I^2}V_{\rm A}^2 + \frac{S_I^{\rm B}}{I^2}V_{\rm B}^2, \tag{4.30}$$

according to Eq. (4.28). By applying Ohm's law, we have

$$S_I = S_I^{\rm A}\frac{V_{\rm A}^2}{V^2} + S_I^{\rm B}\frac{V_{\rm B}^2}{V^2} = S_I^{\rm A}\frac{R_{\rm A}^2}{(R_{\rm A}+R_{\rm B})^2} + S_I^{\rm B}\frac{R_{\rm B}^2}{(R_{\rm A}+R_{\rm B})^2}. \tag{4.31}$$

Applying Eq. (4.31), we obtain S_I for the TLMs

$$S_I = S_I^{\rm ser}\frac{2R_{\rm ser}^2}{(2R_{\rm ser}+R_{\rm 2DEG})^2} + S_I^{\rm 2DEG}\frac{R_{\rm 2DEG}^2}{(2R_{\rm ser}+R_{\rm 2DEG})^2}, \tag{4.32}$$

where $S_I^{\rm ser}$ is the current noise PSD generated by one series resistance $R_{\rm ser} = r_{\rm ser}/W$, and $S_I^{\rm 2DEG}$ is the current noise PSD generated by the channel resistance $R_{\rm 2DEG} = \rho_{\rm s}L/W$.

From Eq. (4.27) and (4.32), we extract the factor K

$$\begin{aligned} K &= \frac{S_I}{I^2}f^{\alpha} \\ &= K_{\rm ser}\frac{2R_{\rm ser}^2}{(2R_{\rm ser}+R_{\rm 2DEG})^2} + K_{\rm 2DEG}\frac{R_{\rm 2DEG}^2}{(2R_{\rm ser}+R_{\rm 2DEG})^2}, \end{aligned} \tag{4.33}$$

where $K_{\rm ser}$ and $K_{\rm 2DEG}$ are the factors for the series resistance and 2DEG channel, respectively. According to Hooge model [108], we have

$$K_{\rm 2DEG} = \frac{\alpha_{\rm ug}}{N} = \frac{\alpha_{\rm ug}}{n_{\rm sug}LW}, \tag{4.34}$$

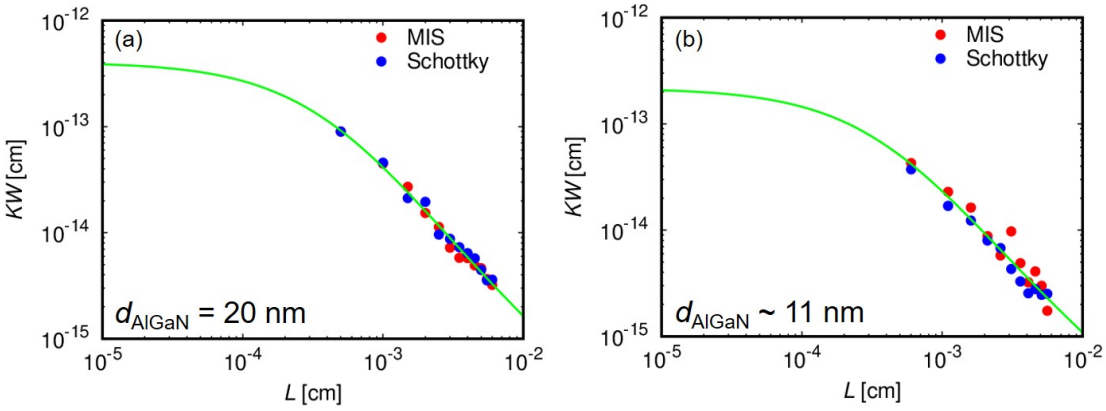

Figure 4.15: KW as functions of L for (a) non-recessed and (b) partially-recessed TLMs with the fitting lines.

where $\alpha_{\rm ug}$ is the Hooge parameter, N is the carrier number, and $n_{\rm sug}$ is the sheet concentration of the ungated 2DEG. We can then rewrite Eq. (4.34) as

$$KW = \frac{(K_{\rm ser}W/2) + (\alpha_{\rm ug}/n_{\rm sug})(\rho_{\rm s}/2r_{\rm ser})^2 L}{[1 + (\rho_{\rm s}/2r_{\rm ser}L)]^2}. \tag{4.35}$$

Equation (4.35) tells us that KW is a function of the device size. In the limit of small L, i.e. $L \to 0$, the terms with L in the RHS of Eq. (4.35) vanish, thus

$$K \simeq K_{\rm ser}/2 = \text{constant}. \tag{4.36}$$

In other words, the device noise is dominated by the series resistance noise. On the other hand, in the limit of large L, i.e. $L \to \infty$, the terms with L in the RHS of Eq. (4.35) dominate other terms, thus

$$KW \simeq \frac{\alpha_{\rm ug}}{n_{\rm sug}L} \propto \frac{1}{L}, \tag{4.37}$$

which means the device noise is dominated by the 2DEG channel noise.

Figure 4.15(a) and (b) depict KW as functions of L with the fitting lines based on Eq. (4.35) for the non-recessed and partially-recessed TLMs, respectively.

We observe that at small L, KW seems to become constant, and decrease $\propto 1/L$ at large L, satisfying the limit conditions. This result confirms the validity of the fittings. In both cases, we find almost no differences between MIS and Schottky TLMs, indicating that AlTiO deposition does not affect the contact and

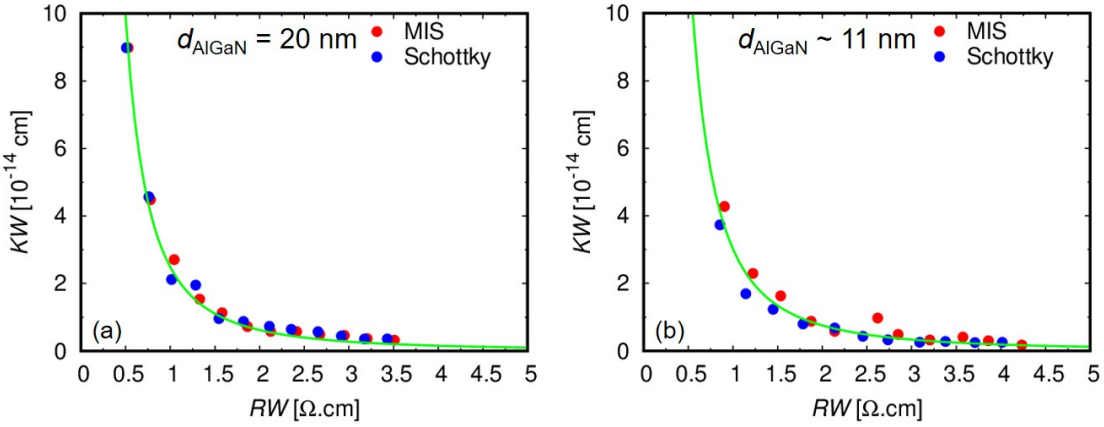

Figure 4.16: KW as functions of RW for (a) non-recessed and (b) partially-recessed TLMs with the fitting lines.

channel resistances. From the fittings, we obtain K_{ser} and Hooge parameter α_{ug} which are summarized in Table 4.2. The values of $K_{\text{ser}}W$ are different owing to the access resistance in case partially-recessed TLMs. We observe α_{ug} in the order of 10^{-5}, small compare to the normal value of Hooge parameter. According to Eq. (4.16), it is plausible to consider mobility fluctuations to be the dominant noise source in TLMs. Moreover, α_{ug} of the partially-recessed TLMs is lower than that of non-recessed TLMs, possibly due to a decrease in the electron mobility owning to the thinner remaining AlGaN layer for the partially-recessed TLMs.

In addition to the size dependence of K, we also obtain a size dependence of the total resistance R of the ungated region

$$RW = (2R_{\text{ser}} + R_{\text{2DEG}})W = 2r_{(}\text{ser}) + \rho_{\text{s}}\text{L}. \tag{4.38}$$

Table 4.2: The factor $K_{\text{ser}}W$ and Hooge parameter α_{ug} obtained from the fittings.

	$d_{\text{AlGaN}} = 20$ nm	$d_{\text{AlGaN}} = 11$ nm
$K_{\text{ser}}W$ [cm]	8.1×10^{-13}	2.5×10^{-13}
α_{ug}	8.1×10^{-5}	3.0×10^{-5}

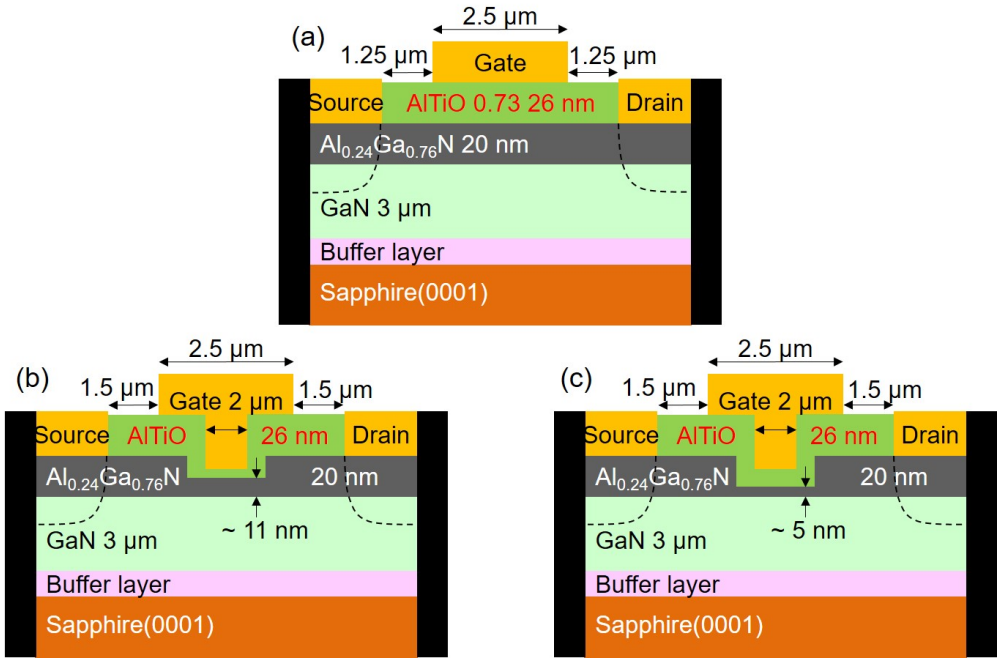

Figure 4.17: The dimensions of AlTiO/AlGaN/GaN MIS-FETs used for low-frequency noise measurement.

We can then rewrite Eq. (4.35) as

$$KW = \frac{2K_{\text{ser}}r_{\text{ser}} + (\alpha_{\text{ug}}\rho_{\text{s}}/n_{\text{sug}})(RW - 2r_{\text{ser}})}{(RW)^2}, \tag{4.39}$$

which implies that KW is a single-values function of RW. Figure 4.16 plots KW-RW relation based on Eq. (4.39) for non-recessed and partially-recessed TLMs.

4.5 Low-frequency noise characterization of AlTIO/AlGaN/GaN MIS-FETs

In this section, we investigated low-frequency noise in AlTIO/AlGaN/GaN MIS-FETs employing $x/(x+y) = 0.73$ composition and $d_{\text{ins}} = 26$ nm with different AlGaN thickness: $d_{\text{AlGaN}} = 20$ nm (non-recess), 11 nm, and 4 nm (partial recess). The device dimensions are given in Fig. 4.17. The devices transfer characteristics are shown in Fig. 4.18. The drain current I_{D}, the gate leakage current I_{G}, and the transconductance g_{m} are normalized by the gate width $W = 50$ μm. Low-frequency noise measurements were performed by using 3T-DUT measurement

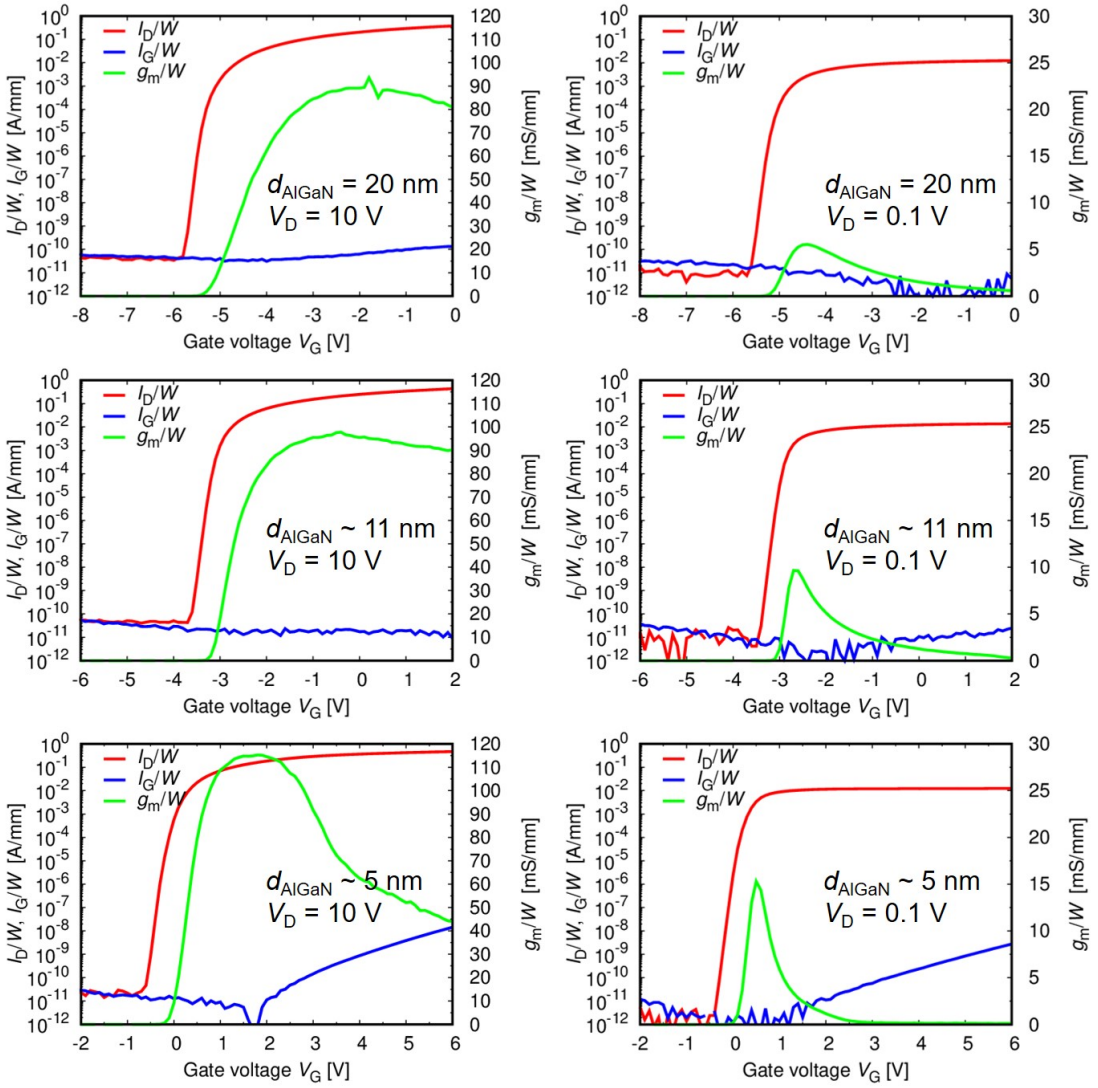

Figure 4.18: The transfer characteristics of the MIS-FETs under V_D = 10 V and 0.1 V.

system configuration shown in Fig. 4.3(b). The measurement procedures are almost similar to those for two-terminal devices. In order to determine the off-set current, we carried out I_D-V_D with a fixed V_G before measuring low-frequency noise using the same V_G. The off-set current corresponding to a bias voltage was taken out from the I_D-V_D data.

The drain current noise PSD S_{I_D} are shown in Fig. 4.19 for each device, where we show examples of the noise spectra with the gate voltage above threshold voltage and in sub-threshold voltage regions. We still observe the peaks at 30 Hz and 45 Hz due to self-heating of DSA. Otherwise no specific bumps or peaks are

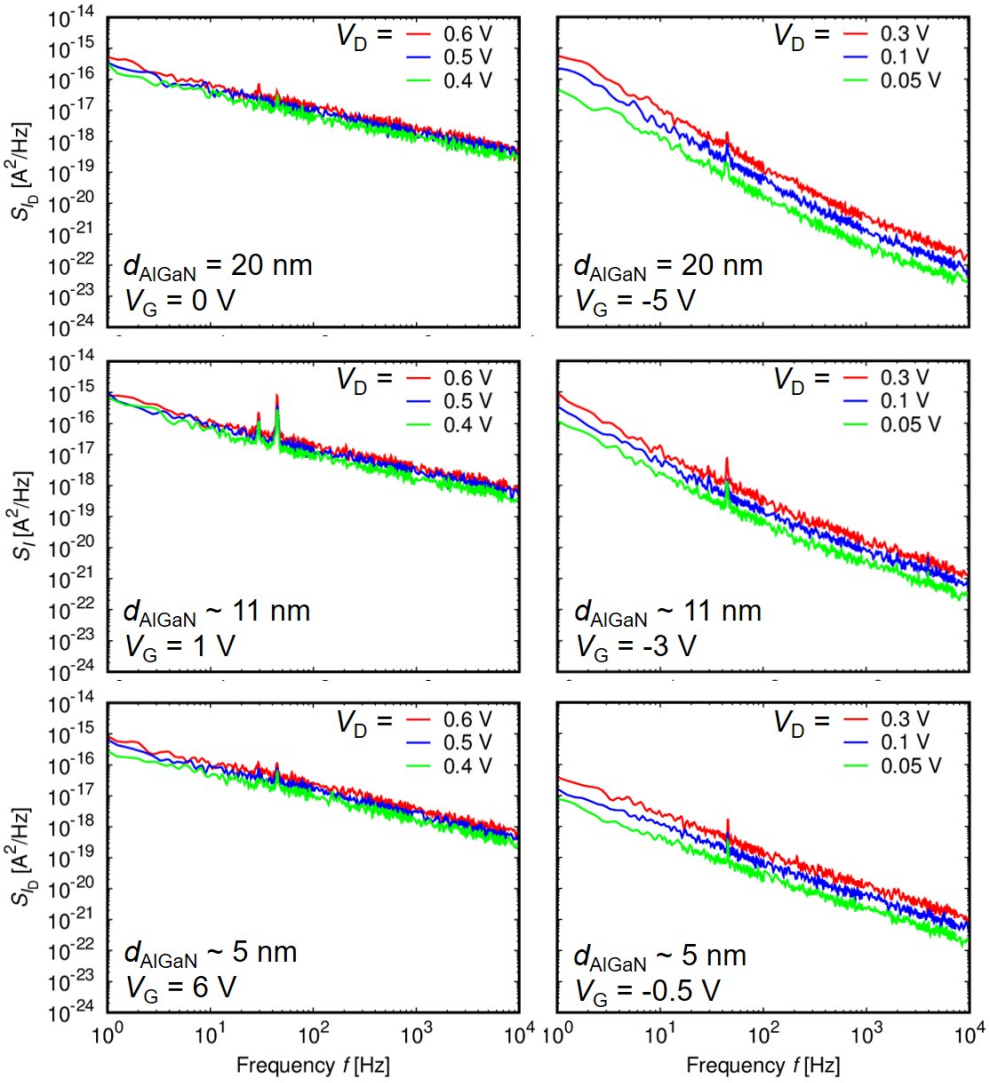

Figure 4.19: Low-frequency spectra of the drain current I_D noise as functions of the frequency f of AlTiO/AlGaN/GaN MIS-FETs with different AlGaN thickness. We show examples with the gate voltage above threshold voltage and in sub-threshold voltage regions.

observed, indicating no generation-recombination noise due to specific high-density electron traps with a specific time constant as well as no external noise effects.

As discussed before, S_{I_D} is proportional to I_D^2. To clarify this, we plot $S_{I_D} f$ as function of I_D for some V_G in Fig. 4.20. From the figure, we can confirm $S_{I_D} \propto I_D^2$. This may suggest that Hooge model can be applied to the drain current noise spectra, in other words

$$S_{I_D} \simeq \frac{K_{FET} I_D}{f^\alpha}, \tag{4.40}$$

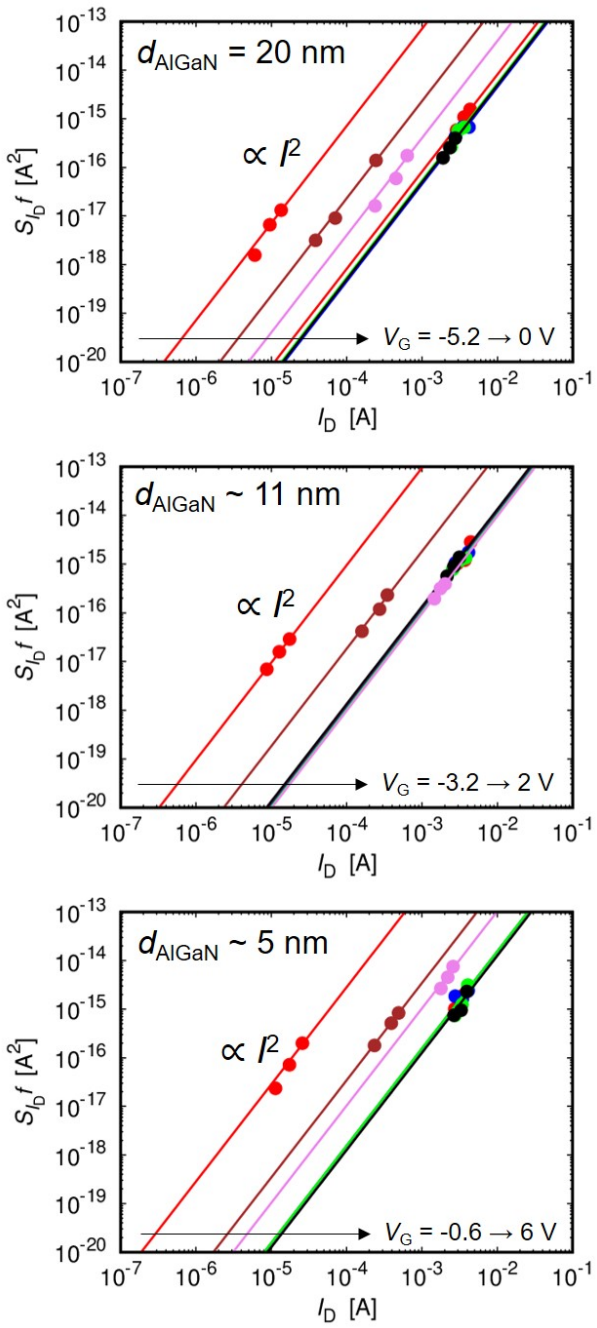

Figure 4.20: $S_{I_D} f$ as functions of the drain current I_D for AlTiO/AlGaN/GaN MIS-FETs with different AlGaN thickness.

where a constant factor K_{FET} depending on the gate bias V_G. Applying Eq. (4.40), we fit the drain current noise PSD as shown in Fig. 4.21 for some examples at different V_G. We observe that not only the factor K_{FET} but also the exponent α varies depending on the gate voltages. We extract K_{FET} and the exponent of

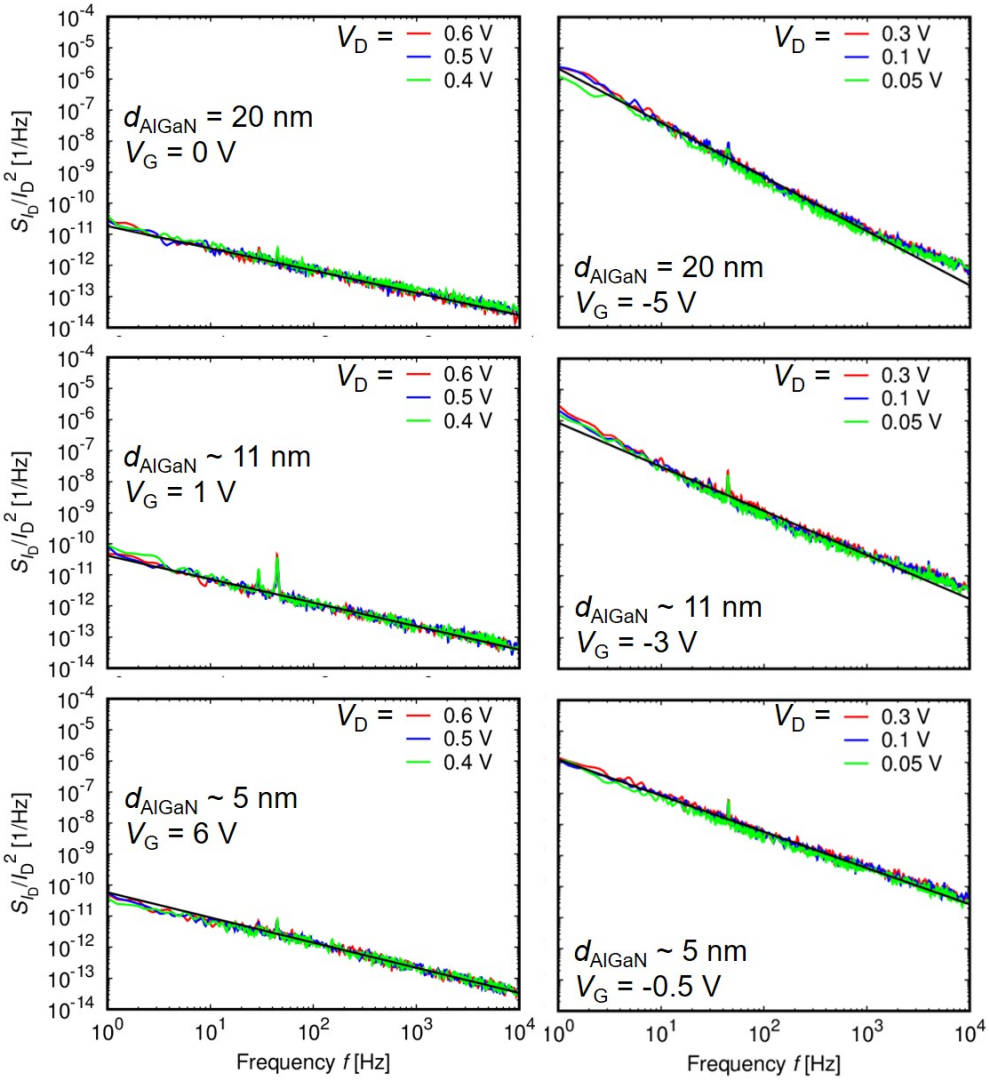

Figure 4.21: S_{I_D} normalized by I_D^2 for AlTiO/AlGaN/GaN MIS-FETs with different AlGaN thickness. The fitting lines are based on Eq. (4.40).

the frequency and plot them as functions of the gate voltage for each device in Fig. 4.22. We observe a behavior that, at high gate voltages, K_{FET} and α stay constantly, while they increase exponentially when the gate voltage decreases and enters the sub-threshold region. In order to confirm that this behavior is not due to noise of the gate voltage, we also measure the noise in case of gate open, and plot the values as dash lines in Fig. 4.22. The obtained results in gate open case is not different with these in $V_G = 0$ V case, indicating the noise originates from the AlTiO insulator. Moreover, although the increase in K_{FET} is same for all devices, the increase in the exponent of f is not. For $d_{\mathrm{AlGaN}} = 20$ nm, α rises quickly, and

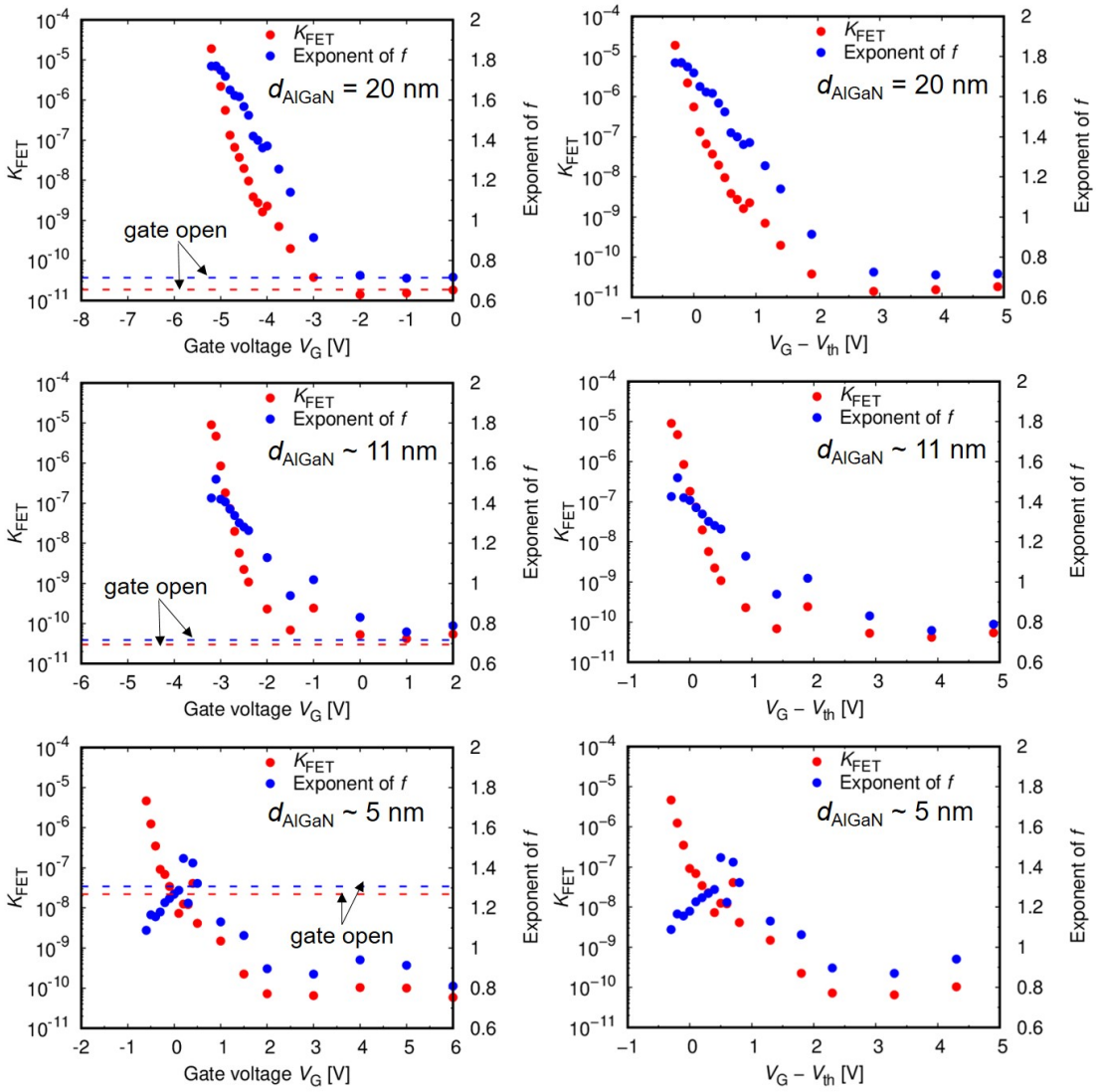

Figure 4.22: The factor K_{FET} and the exponent of the frequency f as functions of gate voltage (left) and $V_{\mathrm{G}} - V_{\mathrm{th}}$ (right) for each device. The dash lines are the measurement values in case of gate open.

seems to stay at ~ 1.8 at low gate voltages. For $d_{\mathrm{AlGaN}} = 11$ nm, α also rises quickly, but stays around ~ 1.4. In particular, for $d_{\mathrm{AlGaN}} = 4$ nm, α increases and decreases, and stays around ~ 1.2.

This behavior cannot be explained by Hooge model. We consider McWhorter model, in which noise is caused by carrier-number fluctuations due to trapping and detrapping of carriers in traps located near oxide/semiconductor interfaces. As discussed before in the previous section, if the device has many relaxation times

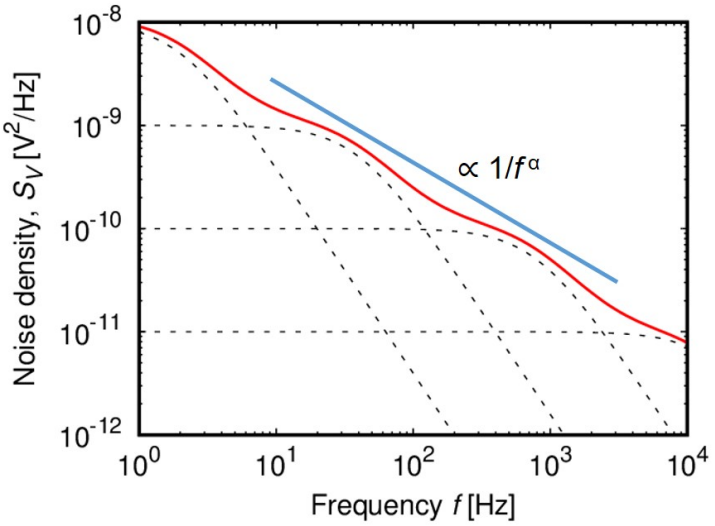

Figure 4.23: An example of how a noise PSD can have a $1/f^{\alpha}$ behavior based on Eq. (4.42).

between τ_1 and τ_2, and their statistical weight $g(\tau)$ is given by

$$g(\tau) = \frac{1}{\ln \tau_1/\tau_2}\frac{1}{\tau},\ \tau_1 > \tau > \tau_2, \tag{4.41}$$

then the noise PSD is

$$S(f) = \int_{\tau_2}^{\tau_1} g(\tau)\frac{4\tau\overline{(\Delta n)^2}}{1+(2\pi f\tau)^2}, \tag{4.42}$$

where τ is the lifetime of the free-carrier-number fluctuation Δn. Based on Eq. (4.42), the noise PSD is a superposition of many Lorentzian spectra having different lifetime τ. The resulting noise can have a $1/f^{\alpha}$ behavior, which is illustrated in Fig. 4.23.

Applying Eq. (4.42), we now can fit the measured noise spectra. Due to the limit of measurement system, the fitting frequency range is from 1 Hz to 1 kHz. The starting gate voltage is at which the systematic increase in K_{FET} and α shows in Fig. 4.22. We find that the superposition of three Lorentzian spectra can fit our data perfectly, as shown in Fig. 4.24. However, we do not observe a Lorentzian behavior in the frequency range $f \leq 10$ Hz, which suggests a very long time constant. Therefore, we can express the noise PSD as

$$\frac{S_{I_{\mathrm{D}}}}{I_{\mathrm{D}}^2} = \frac{A_1}{(2\pi f)^2} + \frac{A_2}{1+(2\pi f\tau_1)^2} + \frac{A_3}{1+(2\pi f\tau_2)^2}, \tag{4.43}$$

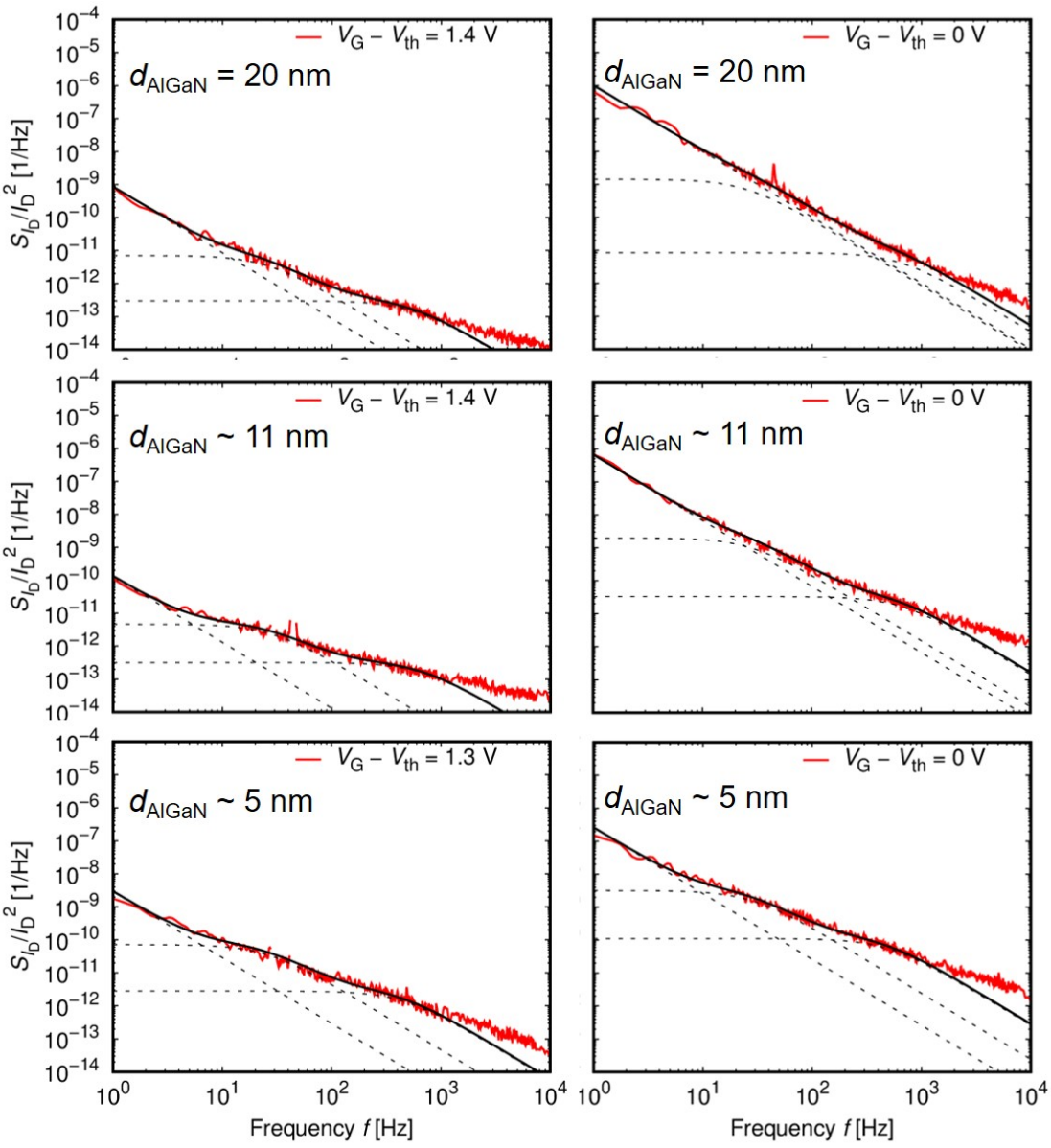

Figure 4.24: Examples of fitting of low-frequency noise spectra by a superposition of three Lorentzian for each device.

where A_1, A_2, and A_3 are Lorentzian prefactors, and τ_1 and τ_2 are time constant satisfying $\tau_1 > \tau_2$. As a result, we obtain time constants as functions of $V_G - V_{th}$ as shown in Fig. 4.25. We find that two specific time constants, $\tau_1 \sim 5$ ms and $\tau_2 \sim 0.3$ ms are independent of V_G and AlGaN thickness d_{AlGaN}. Although the previously-reported values of τ_1 and τ_2 for AlTiO with the same $(x/(x+y) = 0.73)$ composition are one order higher ($\tau_1 \sim 25$ ms and $\tau_2 \sim 3$ ms) [71], the previous

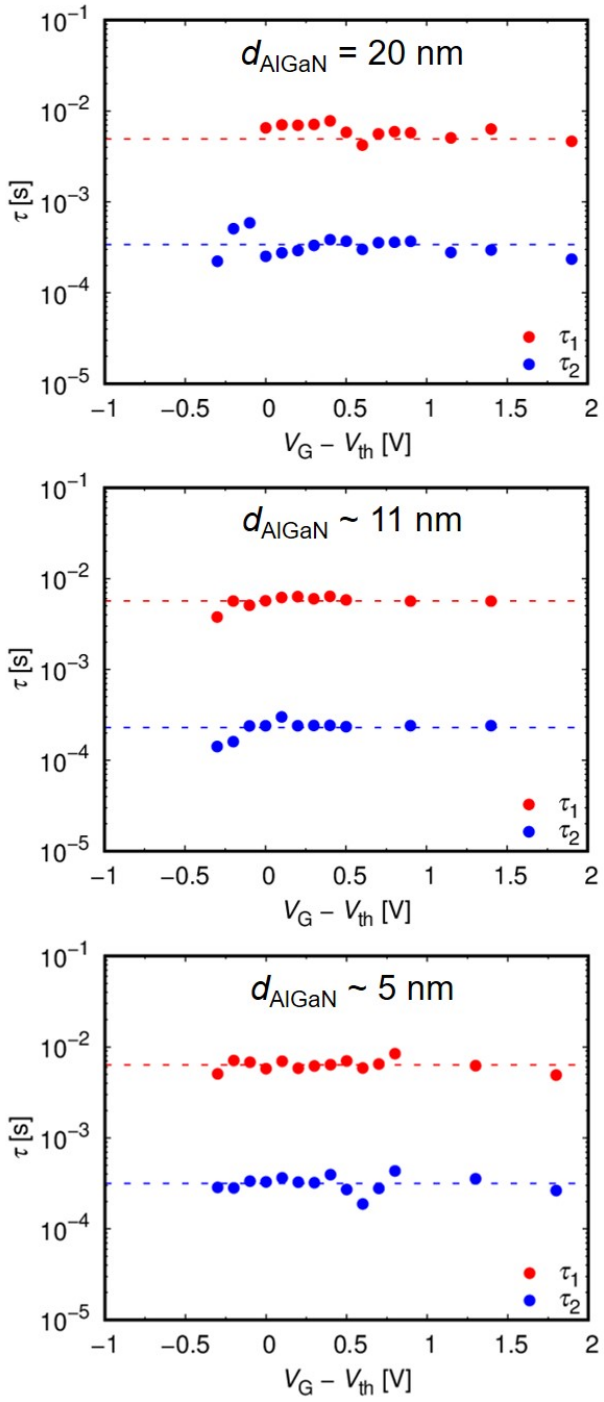

Figure 4.25: Time constants τ_1 and τ_2 as functions of $V_G - V_{th}$ for each device.

AlGaN/GaN structure is $Al_{0.27}Ga_{0.73}N$ (7 nm)/ n-$Al_{0.27}Ga_{0.73}N$ (20 nm, Si doping concentration of 2×10^{18} cm^{-3})/ $Al_{0.27}Ga_{0.73}N$ (3 nm)/ GaN (3000 nm), which is different from the structure used in this study. It might have effect on the time

constants, because in general, a time constant τ at temperature T is given by

$$\tau = \frac{1}{v_{\rm th}\sigma_{\rm e}N_{\rm c}}e^{E_{\rm a}/k_{\rm B}T} = \tau_0 e^{E_{\rm a}/k_{\rm B}T}, \tag{4.44}$$

where $k_{\rm B}$ is the Boltzmann constant, $v_{\rm th}$ is the electron thermal velocity, $\sigma_{\rm e}$ is the electron capture cross-section, $N_{\rm c}$ is the effective density of states in the conduction band, and $E_{\rm a}$ is the trap level depth. In order to evaluate τ, we need to determine other quantities value. The electron thermal velocity is given by

$$v_{\rm th} = \sqrt{\frac{3k_{\rm B}T}{m^*}}, \tag{4.45}$$

and the effective density of states is

$$N_{\rm c} \simeq 2\left(\frac{2\pi m^* k_{\rm B}T}{h^2}\right)^{3/2}, \tag{4.46}$$

where m^* is the electron effective mass and h is the Planck constant. Although we do not know AlTiO electron capture section and effective mass, we can assume a wide range of $\sigma_{\rm e} = 10^{-16} \rightarrow 10^{-13}$ cm^2 and m^* between $0.3m_0$ for Al_2O_3 [115] and $30m_0$ for TiO_2 [116, 117] (m_0: the bare electron mass), thus we obtain

$$\tau_0 = \frac{1}{v_{\rm th}\sigma_{\rm e}N_{\rm c}} = 1 \text{ fs } \rightarrow 10 \text{ ps}. \tag{4.47}$$

The trap level depths can be estimated to be

$$E_{\rm a_1} = k_{\rm B}T\ln\left(\frac{\tau_1}{\tau_0}\right) \simeq 0.46 \rightarrow 0.76 \text{ eV}, \tag{4.48}$$

and

$$E_{\rm a_2} = E_{\rm a_1} - \Delta E_{\rm a}, \tag{4.49}$$

with

$$\Delta E_{\rm a} = k_{\rm B}T\ln\left(\frac{\tau_1}{\tau_2}\right) \simeq 0.08 \text{ eV}. \tag{4.50}$$

We plot the relation between the time constant and the electron trap level depth in Fig. 4.26. The obtained electron trap level depths are consistent with the previous results [71].

On the other hand, the Lorentzian prefactors depend on $V_{\rm G}$. Figure 4.27 shows the normalized Lorentzian prefactors, which are the products of the prefactor and

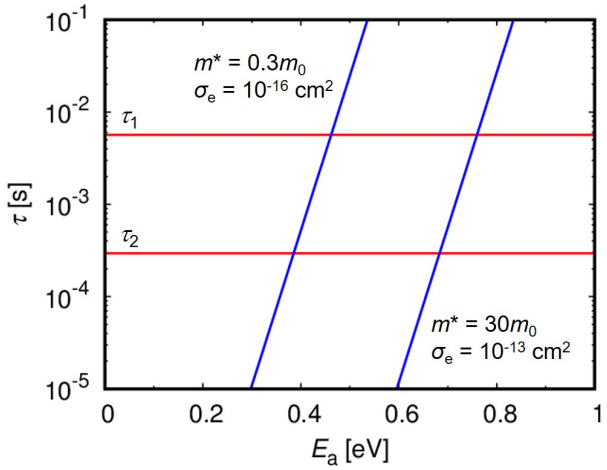

Figure 4.26: The relation between the time constant τ and the electron trap level depth E_{a}.

the gate area, $A_1 L_{\mathrm{G}} W$ and $A_2 L_{\mathrm{G}} W$ as functions of $V_{\mathrm{G}} - V_{\mathrm{th}}$. We observe a trend that the normalized Lorentzian prefactors increases with a decrease in $V_{\mathrm{G}} - V_{\mathrm{th}}$, implying that the effects of electron trapping/detrapping are more dominant near the threshold voltages. Therefore, for the well-above-threshold regime, Lorentzian LFN is buried in $1/f$ spectra.

In order to understand the meaning of the Lorentzian prefactors, we consider a general Lorentzian current PSD normalized by the current square

$$\frac{S_I}{I^2} = \frac{A}{1+(2\pi\tau f)^2} = \frac{2\pi\tau\alpha_{\mathrm{L}}}{N}\frac{1}{1+(2\pi\tau f)^2}, \tag{4.51}$$

with a prefactor A (in the unit of [1/Hz]) and a specific time constant τ (or a specific frequency $f_0 = 1/2\pi\tau$), where we define a dimensionless Hooge-like parameter α_{L} for Lorentzian LFN by $A = \alpha_{\mathrm{L}}/Nf_0 = 2\pi\tau\alpha_{\mathrm{L}}/N$ using the total carrier number N. Since the current fluctuation δI is given by

$$\begin{aligned}\frac{(\delta I)^2}{I^2} &= \int_0^\infty \frac{S_I}{I^2} df \\ &= \int_0^\infty \frac{2\pi\tau\alpha_{\mathrm{L}}}{N}\frac{1}{1+(2\pi\tau f)^2} df \\ &= \frac{\pi}{2}\frac{\alpha_{\mathrm{L}}}{N},\end{aligned} \tag{4.52}$$

and Burgess theorem [118] gives

$$\frac{(\delta I)^2}{I^2} = \frac{1}{N}\left[\frac{(\delta\mu)^2}{\mu^2} + \frac{(\delta N)^2}{N^2}\right], \tag{4.53}$$

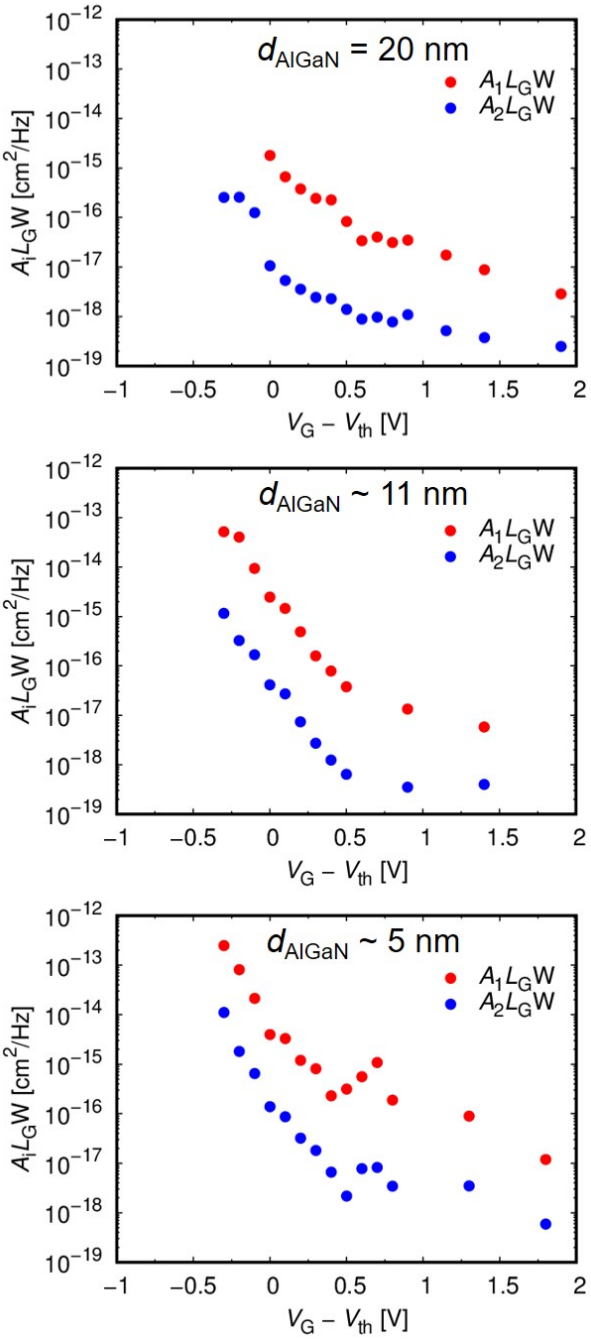

Figure 4.27: Normalized Lorentzian prefactors, products of the prefactor and the gate area, $A_1 L_G W$ and $A_2 L_G W$ as functions of $V_G - V_{th}$ for each device.

where $\delta\mu$ and δN are the fluctuations of the mobility μ and the carrier number N, respectively, we obtain

$$\alpha_L = \frac{2}{\pi}\left[\frac{(\delta\mu)^2}{\mu^2} + \frac{(\delta N)^2}{N^2}\right], \tag{4.54}$$

showing that the Hooge-like parameter is related to fluctuations of the mobility and

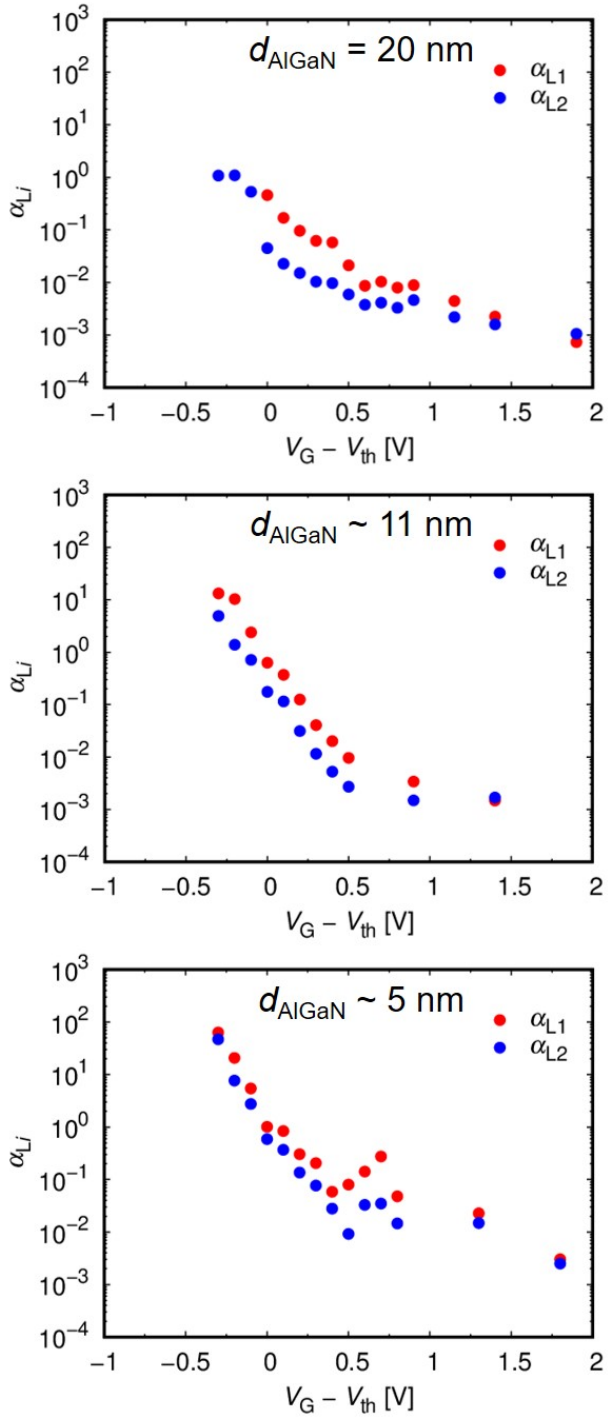

Figure 4.28: The Hooge-like parameters α_{Li} as functions of $V_G - V_{th}$ for each device.

carrier number. According to the definition, we evaluate $\alpha_{Li} = A_i N/(2\pi\tau_i)$ $(i = 1, 2)$. Figure 4.28 shows α_{Li} as functions of $V_G - V_{th}$ for each device, where we find $\alpha_{L1} \sim \alpha_{L2}$. This suggests the same origin of the two trap levels in the AlTiO gate insulator, which could attributed to an on-site Coulomb effect [119]. Al-

though two electrons (with opposite spins) can occupy one trap level, the on-site Coulomb repulsion shifts the effective level for the second electron shallower, thus give $\Delta E_{\mathrm{a}} \simeq 0.08$ eV. Moreover, we observe that $\alpha_{\mathrm{L}i}$ increases with a decrease in the ALGaN thickness, which could be owing to the decrease in the channel electron mobility. Physically speaking, the increase in the Hooge-like parameters means an increase in the noise magnitude, which could lower the device performances. Therefore, though interface charge engineering, we could realize normally-off Al-TiO/AlGaN/GaN MIS-FETs with thicker remaining AlGaN layers, which can have higher channel electron mobility and lower noise, thus higher reliability.

Chapter 5

Conclusion and future perspectives

5.1 Conclusion of this work

In this work, we investigated interface charge engineering using AlTiO gate insulators in order to realize normally-off operations in AlTiO/AlGaN/GaN metal-insulator-semiconductor (MIS) field-effect transistors (FETs). First of all, we systematically investigated the interface charge engineering in non-recessed AlTiO/AlGaN/GaN MIS devices by evaluating the positive interface fixed charge density depending on the AlTiO composition. We found a trend that the positive interface fixed charge density decreases with a decrease in the Al composition ratio, i.e increase in the Ti composition ratio, although, the trend is saturated below intermediate Al compositions, leading to the independence on the insulator thickness of the threshold voltage. This results indicate that AlTiO is a versatile insulator, which can be applied to energy gap engineering, dielectric constant engineering, and interface charge engineering via its composition. In order to realize normally-off operations with good transport properties for AlTiO/AlGaN/GaN MIS-FETs, we investigated the interface charge engineering in partially-recessed AlTiO/AlGaN/GaN MIS devices with a thick remaining AlGaN layer. We found that for AlTiO with a composition of $x/(x+y) = 0.73$, the positive fixed charge

is significantly suppressed at AlTiO/recessed-AlGaN interface in comparison with that at Al_2O_3/recessed-AlGaN interface, leading to a positive slope in the relation between the threshold voltage and the AlTiO insulator thickness. As a result, we successfully obtained normally-off operations in partially-gate-recessed AlTiO/AlGaN/GaN MIS-FETs with favorable performances, such as a threshold voltage of 1.7 V, an on-resistance of 9.5 Ω·mm, an output current of 450 mA/mm, a low sub-threshold swing of 65 mV/decade, and a rather high electron mobility of 730 cm^2/V·s.

In addition the these results, we also carried out material characterization such as X-ray photoelectron spectroscopy (XPS) to clarify the origin of the positive interface fixed charge. From the XPS analysis of the AlTiO/AlGaN interface, we found a relation between bonding states of Ga and the positive interface charge density σ_{ins}: an increase in Ga-N bonding state (i.e. a decrease in Ga-O bonding state) leads to an increase in σ_{ins}. We also carried out low-frequency noise (LFN) characterization for AlTiO/AlGaN/GaN MIS-FETs with the AlTiO composition of $x/(x+y) = 0.73$ and different remaining AlGaN thickness. We found a $1/f^{\alpha}$ behavior according to McWhorter model near the threshold voltage with two specific time constants $\sim$ 5 ms and $\sim$ 0.3 ms, corresponding to trap level depths of $0.46 - 0.76$ eV in the AlTiO insulator, which is independent of the remaining AlGaN thickness. Moreover, the decrease in the remaining AlGaN thickness leads to an increase in the noise magnitude owing to a decrease in the channel electron mobility.

5.2 Future perspectives of this work

Although we realized normally-off operations in AlTiO/AlGaN/GaN MIS-FETs though interface charge engineering, the positive interface fixed charge density is still high ($\sim 10^{13}$ cm^{-2}). More experiments and better understanding of the origin of the positive interface fixed charge are needed to suppress the positive interface fixed charge density. In order to elucidate the origin of the positive interface fixed charge, more evidences from XPS and other measurements need to be gathered

to draw a concrete conclusion. For LFN characterization, the measurement was carried out at room temperature. In the future, temperature-dependent LFN in AlTiO/AlGaN/GaN with different AlTiO compositions should be investigated in order to clarify the noise mechanisms.

Appendix A

Band diagram calculation

Figure A.1 shows the theoretical band diagram of Al_xTi_yO/AlGaN/GaN MIS devices. The notions are: the vacuum permittivity ϵ_0, the dielectric constant k_{ins} and k_{AlGaN}, the metal-insulator barrier height ϕ, the insulator-semiconductor conduction band offset φ, the AlGaN-GaN conduction band offset ΔE_{c}, the positive interface fixed charge density σ_{ins}, the AlGaN polarization charge density σ_{AlGaN}, and the GaN polarization charge density σ_{GaN}, and the 2DEG Fermi energy E_{F}.

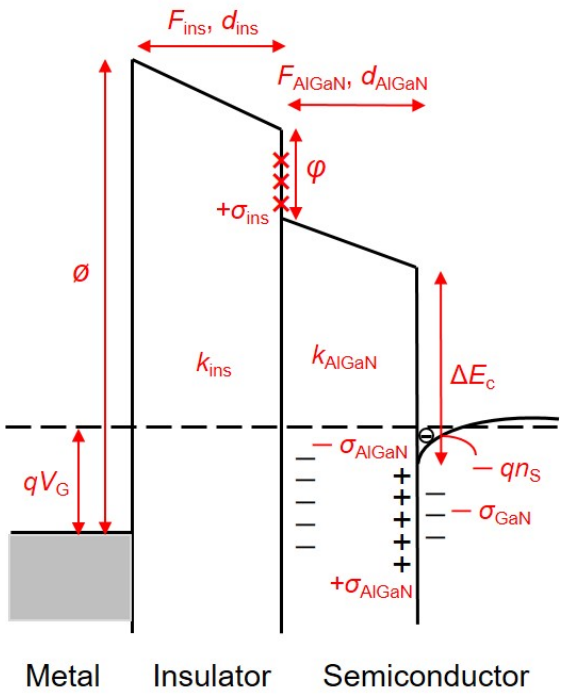

Figure A.1: Theoretical band diagram of the Al_xTi_yO/AlGaN/GaN MIS-devices.

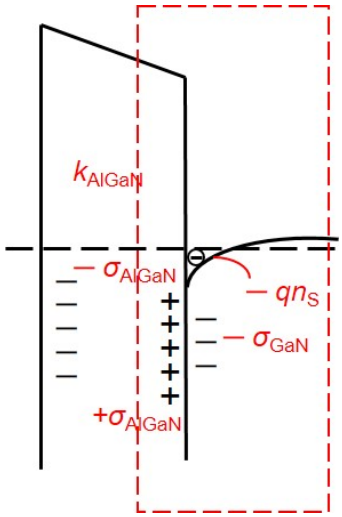

Figure A.2: Applying Gauss box in band diagram for AlGaN.

Based on the 1-dimension Poisson equation, we have

$$\frac{\partial^2 \psi}{\partial x^2} = -\frac{\rho}{\varepsilon}, \tag{A.1}$$

using the potential ψ. Taking the integral of Eq. A.1, we have

$$\frac{\partial \psi}{\partial x} = F, \tag{A.2}$$

where F is the electric field strength inside the insulator or AlGaN. We assume that the positive interface fixed charge and the polarization charge are at and/or near the interface, thereby we can apply Gauss law. Assume that we have a Gauss box covering both AlGaN and GaN shown in Fig. A.2, where the electric field on the left of the box is F_{AlGaN}, and the electric field on the right is F_{GaN}. The total charges inside the box will be $\rho = \sigma_{\mathrm{AlGaN}} - \sigma_{\mathrm{GaN}} - qn_{\mathrm{s}}$. Based on the Gauss equation, we have

$$\begin{aligned} F_{\mathrm{AlGaN}} - F_{\mathrm{GaN}} &= \frac{\rho}{\varepsilon} = \frac{\sigma_{\mathrm{AlGaN}} - \sigma_{\mathrm{GaN}} - qn_{\mathrm{s}}}{\varepsilon} \\ &= \frac{\Delta\sigma_{\mathrm{AlGaN}} - qn_{\mathrm{s}}}{k_{\mathrm{AlGaN}}\varepsilon_0}. \end{aligned} \tag{A.3}$$

For GaN part, the boundary condition implies that there is no charges as the right side of the box goes deeper, i.e. it is at neutral (equilibrium) state. Hence, no electric field inside GaN, or $F_{\mathrm{GaN}} = 0$. Therefore, we have

$$F_{\mathrm{AlGaN}} = \frac{\Delta\sigma_{\mathrm{AlGaN}} - qn_{\mathrm{s}}}{k_{\mathrm{AlGaN}}\varepsilon_0}. \tag{A.4}$$

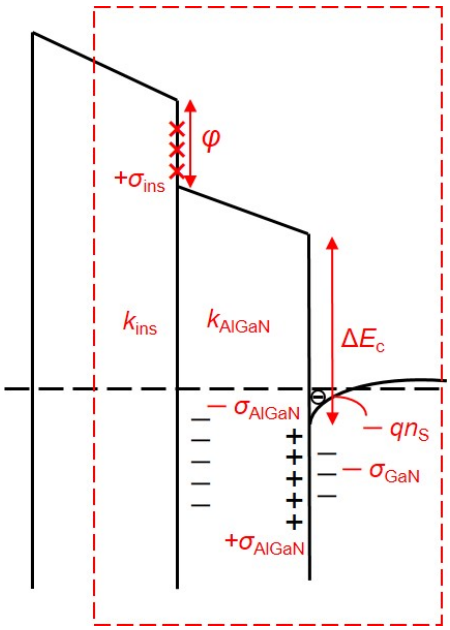

Figure A.3: Applying Gauss box in band diagram for the insulator.

The potential inside AlGaN is

$$\psi_{\mathrm{AlGaN}} = F_{\mathrm{AlGaN}} d_{\mathrm{AlGaN}} = \frac{\Delta\sigma_{\mathrm{AlGaN}} - qn_{\mathrm{s}}}{k_{\mathrm{AlGaN}}\varepsilon_0} d_{\mathrm{AlGaN}}. \tag{A.5}$$

Apply similar analysis for the insulator part, with the assumption that there is no bulk charge inside the insulator, as shown in Fig. A.3, we have

$$\begin{aligned} F_{\mathrm{ins}} &= \frac{\sigma_{\mathrm{ins}} + \sigma_{\mathrm{AlGaN}} - \sigma_{\mathrm{GaN}} - qn_{\mathrm{s}}}{\varepsilon} \\ &= \frac{\Delta\sigma_{\mathrm{ins}} - qn_{\mathrm{s}}}{k_{\mathrm{ins}}\varepsilon_0}. \end{aligned} \tag{A.6}$$

The potential inside the insulator then is

$$\psi_{\mathrm{ins}} = F_{\mathrm{ins}} d_{\mathrm{ins}} = \frac{\Delta\sigma_{\mathrm{ins}} - qn_{\mathrm{s}}}{k_{\mathrm{ins}}\varepsilon_0} d_{\mathrm{ins}}. \tag{A.7}$$

From the MIS band diagram in Fig. A.1, the sum of the potentials of the insulator and AlGaN can be calculated as

$$\psi_{\mathrm{ins}} + \psi_{\mathrm{AlGaN}} = -V_{\mathrm{G}} + (\phi - \varphi - \Delta E_{\mathrm{C}} + E_{\mathrm{F}})/q. \tag{A.8}$$

Here E_{F} is the Fermi level of GaN, so we can assume it to be at common level, i.e. $E_{\mathrm{F}} = 0$. Substitute all parameters into Eq. A.8, we have

$$\frac{\Delta\sigma_{\mathrm{ins}} - qn_{\mathrm{S}}}{k_{\mathrm{ins}}\varepsilon_0} d_{\mathrm{ins}} + \frac{\Delta\sigma_{\mathrm{AlGaN}} - qn_{\mathrm{S}}}{k_{\mathrm{AlGaN}}\varepsilon_0} d_{\mathrm{AlGaN}} = -V_{\mathrm{G}} + (\phi - \varphi - \Delta E_{\mathrm{C}})/q. \tag{A.9}$$

We can rewrite it as

$$\frac{\Delta\sigma_{\mathrm{ins}} - qn_{\mathrm{S}}}{k_{\mathrm{ins}}\varepsilon_0} d_{\mathrm{ins}} + \frac{\Delta\sigma_{\mathrm{AlGaN}} - qn_{\mathrm{S}}}{k_{\mathrm{AlGaN}}\varepsilon_0} d_{\mathrm{AlGaN}} = -V_{\mathrm{G}} + \psi/q, \tag{A.10}$$

where $\psi = \phi - \varphi - \Delta E_{\mathrm{C}}$ is a deduced constant.

Appendix B

Conductance method

For insulator-semiconductor interface of a MIS device, the electron occupation probability P at an interface state with energy E shown in Fig. B.1, is given by a time-dependent rate equation

$$\frac{\partial P}{\partial t} = \gamma(1-P)n - \alpha P, \tag{B.1}$$

where n is the semiconductor electron density at the interface, and γ and α are proportional constants. In Eq. B.1, the first term is related to the trapping and the second term is related to the detrapping. The constant γ is given by

$$\gamma = v_{\mathrm{th}}\sigma \tag{B.2}$$

where v_{th} is the electron thermal velocity and σ is the electron capture cross-section.

If we separate P, n and surface potential V into its direct current (DC) and alternative current (AC), we obtain

$$\begin{aligned} P &= P_0 + \widetilde{P}\exp(j\omega t) \\ n &= n_0 + \widetilde{n}\exp(j\omega t) \\ V &= V_0 + \widetilde{V}\exp(j\omega t). \end{aligned} \tag{B.3}$$

The P_0 component at energy E is given by Fermi-Dirac distribution

$$P_0(E) = \frac{1}{1+\exp[(E-E_{\mathrm{f}})/k_{\mathrm{B}}T]}. \tag{B.4}$$

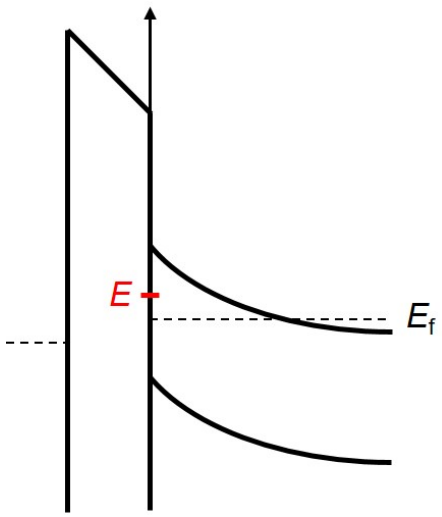

Figure B.1: Electron at energy E at the insulator-semiconductor interface.

Thus, we have

$$\begin{aligned}\frac{dP_0}{dE} &= -\frac{\exp[(E-E_\mathrm{f})/k_\mathrm{B}T]/k_\mathrm{B}T}{(1+\exp[(E-E_\mathrm{f})/k_\mathrm{B}T])^2} \\ &= -\frac{P_0(1-P_0)}{k_\mathrm{B}T}.\end{aligned} \tag{B.5}$$

Substitute the DC components into Eq. B.1, we obtain

$$\alpha = \gamma n_0(1-P_0)/P_0 = \frac{1-P_0}{\tau P_0}, \quad \text{with } \tau = \frac{1}{\gamma n_0}. \tag{B.6}$$

In the range of small AC signal modulation, α is approximated to Eq. B.6. From Eq. B.1, we have

$$j\omega\widetilde{P}\exp(j\omega t) = \gamma(1-P)n - \frac{(1-P_0)P}{\tau P_0}. \tag{B.7}$$

The right hand side of Eq. B.7 equals to

$$\begin{aligned}&\gamma(1-P)n - \frac{(1-P_0)P}{\tau P_0} = \frac{\gamma(1-P)n\tau P_0 - (1-P_0)P}{\tau P_0} \\ &= \frac{[1-P_0-\widetilde{P}\exp(j\omega t)][n_0+\widetilde{n}\exp(j\omega t)]P_0/n_0 - (1-P_0)(P_0+\widetilde{P}\exp(j\omega t))}{\tau P_0} \\ &= \frac{\widetilde{n}P_0/n_0 - P_0^2\widetilde{n}/n_0 - \widetilde{P} - \widetilde{P}\widetilde{n}P_0\exp(j\omega t)/n_0}{\tau P_0}\exp(j\omega t) \\ &= \frac{P_0(1-P_0)\widetilde{n}/n_0 - \widetilde{P}[\widetilde{n}P_0\exp(j\omega t)/n_0+1]}{\tau P_0}\exp(j\omega t).\end{aligned} \tag{B.8}$$

In case of small AC signal modulation, we have $\widetilde{n} \ll n_0$, thus $\widetilde{n}P_0 \exp(j\omega t/n_0) \ll 1$. With this approximation, Eq. B.7 turns into

$$j\omega\widetilde{P}\exp(j\omega t) \simeq \frac{P_0(1-P_0)\widetilde{n}/n_0 - \widetilde{P}}{\tau P_0}\exp(j\omega t). \tag{B.9}$$

We can rewrite Eq. B.9 as

$$\widetilde{P} \simeq \frac{P_0(1-P_0)}{1+j\omega\tau P_0}\frac{\widetilde{n}}{n_0} = \frac{P_0(1-P_0)}{1+j\omega\tau P_0}\frac{q\widetilde{V}}{k_{\mathrm{B}}T}, \tag{B.10}$$

at temperature T where k_{B} is Boltzmann constant. The total small signal AC admittance Y_{i} is calculated by taking sum over all interface states, i.e.

$$\begin{aligned} Y_{\mathrm{i}} &= G_{\mathrm{i}} + jC_{\mathrm{i}}\omega \\ &= \frac{j\omega q}{\widetilde{V}}\int D_{\mathrm{i}}(E)\widetilde{P}dE \\ &= \frac{j\omega q^2}{k_{\mathrm{B}}T}\int \frac{D_{\mathrm{i}}(E)P_0(1-P_0)}{1+j\omega\tau P_0}dE \\ &= j\omega q^2 \int \frac{D_{\mathrm{i}}(E)}{1+j\omega\tau P_0}\left(-\frac{dP_0}{dE}\right)dE, \end{aligned} \tag{B.11}$$

with interface state density D_{i}.

AC admittance for the low temperature limit

For low temperature, we have the approximation

$$-\frac{dP_0}{dE} \simeq \delta(E - E_{\mathrm{f}}). \tag{B.12}$$

Substitute into Eq. B.11, we have

$$\begin{aligned} G_{\mathrm{i}} + jC_{\mathrm{i}}\omega &= j\omega q^2 \int \frac{D_{\mathrm{i}}(E)}{1+j\omega\tau P_0}\left(-\frac{dP_0}{dE}\right)dE \\ &\simeq \frac{j\omega q^2 D_{\mathrm{i}}(E_{\mathrm{f}})}{1+j\omega\tau/2} \end{aligned} \tag{B.13}$$

Extract G_{i} and C_{i}, we obtain

$$\begin{aligned} \frac{G_{\mathrm{i}}}{\omega} &= \frac{\omega\tau q^2 D_{\mathrm{i}}}{2(1+\omega^2\tau^2/4)} \\ C_{\mathrm{i}} &= \frac{q^2 D_{\mathrm{i}}}{1+\omega^2\tau^2/4}. \end{aligned} \tag{B.14}$$

AC admittance for a discrete interface state

For a discrete interface state, the interface state density D_i becomes the delta function of the energy, i.e.

$$D_\mathrm{i}(E) = D_0\ \delta(E - E_0). \tag{B.15}$$

Substitute into Eq. B.11, we have

$$\begin{aligned} G_\mathrm{i} + jC_\mathrm{i}\omega &= j\omega q^2 \int \frac{D_\mathrm{i}(E)}{1 + j\omega\tau P_0} \left(-\frac{dP_0}{dE}\right) dE \\ &= \frac{j\omega q^2 D_0}{1 + j\omega\tau P_0(E_0)} \frac{\exp[(E_0 - E_\mathrm{f})/k_\mathrm{B}T]}{k_\mathrm{B}T(1 + \exp[(E_0 - E_\mathrm{f})/k_\mathrm{B}T])^2} \\ &= \frac{j\omega q^2 D_0}{4k_\mathrm{B}T(1 + j\omega\tau/2)}. \quad (\text{for } E_\mathrm{f} = E_0) \end{aligned} \tag{B.16}$$

Extract G_i and C_i, we obtain

$$\begin{aligned} \frac{G_\mathrm{i}}{\omega} &= \frac{\omega\tau q^2 D_0}{8k_\mathrm{B}T(1 + \omega^2\tau^2/4)} \\ C_\mathrm{i} &= \frac{q^2 D_0}{4k_\mathrm{B}T(1 + \omega^2\tau^2/4)}. \end{aligned} \tag{B.17}$$

AC admittance for general continuous interface states

For general continuous interface states, the interface state density D_i becomes a constant, not dependent of the energy. Equation B.11 now is

$$\begin{aligned} G_\mathrm{i} + jC_\mathrm{i}\omega &= j\omega q^2 \int \frac{D_\mathrm{i}(E)}{1 + j\omega\tau P_0} \left(-\frac{dP_0}{dE}\right) dE \\ &\simeq j\omega q^2 D_\mathrm{i} \int \frac{1}{1 + j\omega\tau P_0} \left(-\frac{dP_0}{dE}\right) dE \\ &= j\omega q^2 D_\mathrm{i} \int_0^1 \frac{dP_0}{1 + j\omega\tau P_0} \\ &= \frac{q^2 D_\mathrm{i} \ln(1 + j\omega\tau)}{\tau} \end{aligned} \tag{B.18}$$

Extract G_i and C_i, we obtain

$$\begin{aligned} \frac{G_\mathrm{i}}{\omega} &= \frac{\omega\tau q^2 D_0}{8k_\mathrm{B}T(1 + \omega^2\tau^2/4)} \\ C_\mathrm{i} &= \frac{q^2 D_0}{4k_\mathrm{B}T(1 + \omega^2\tau^2/4)}, \end{aligned} \tag{B.19}$$

which are the bases of the conductance method. The time constant τ is

$$\tau(E_\mathrm{f}) = \frac{1}{\gamma n_0(E_\mathrm{f})} = \frac{\exp[(E_\mathrm{c} - E_\mathrm{f})/k_\mathrm{B}T]}{v_\mathrm{th}\sigma N_\mathrm{c}} \propto \exp\left(\frac{E_\mathrm{c} - E_\mathrm{f}}{k_\mathrm{B}T}\right). \tag{B.20}$$

Appendix C

X-ray photoelectron spectroscopy (XPS)

When X-rays are irradiated on the sample surface in an ultrahigh vacuum, the inner shell electrons absorb light energy by the photoelectric effect and emit in the vacuum as photoelectrons. At this time, assuming that the photon energy of the irradiated X-rays is $h\nu$ and the binding energy of the bound electrons is E_{b} as shown in Fig. C.1, the kinetic energy E_{kin} of the photoelectron is given by Einstein's equation

$$E_{\mathrm{kin}} = h\nu - E_{\mathrm{b}}. \tag{C.1}$$

By detecting the number and the kinetic energy of the photoelectrons released in the vacuum, the distribution curve of the binding energy and the energy level of the electrons of the element in the sample can be determined, so that the element chemical state can be identified and quantified. This is also called Electron Spectroscopy for Chemical Analysis (ESCA).

A schematic diagram of the equipment used in this study is shown in Fig. C.2. X-rays are released by applying accelerated electrons emitted by the filament to the Al target of the anode. When the incident electrons knock the electrons at low level, electrons at high level relax and jump back to low level. This process emits electromagnetic waves. For Al metal, when an electron from orbital 2p jumps back to 1s, it releases X-ray with the energy of 1486.6 eV as shown in Fig. C.3,

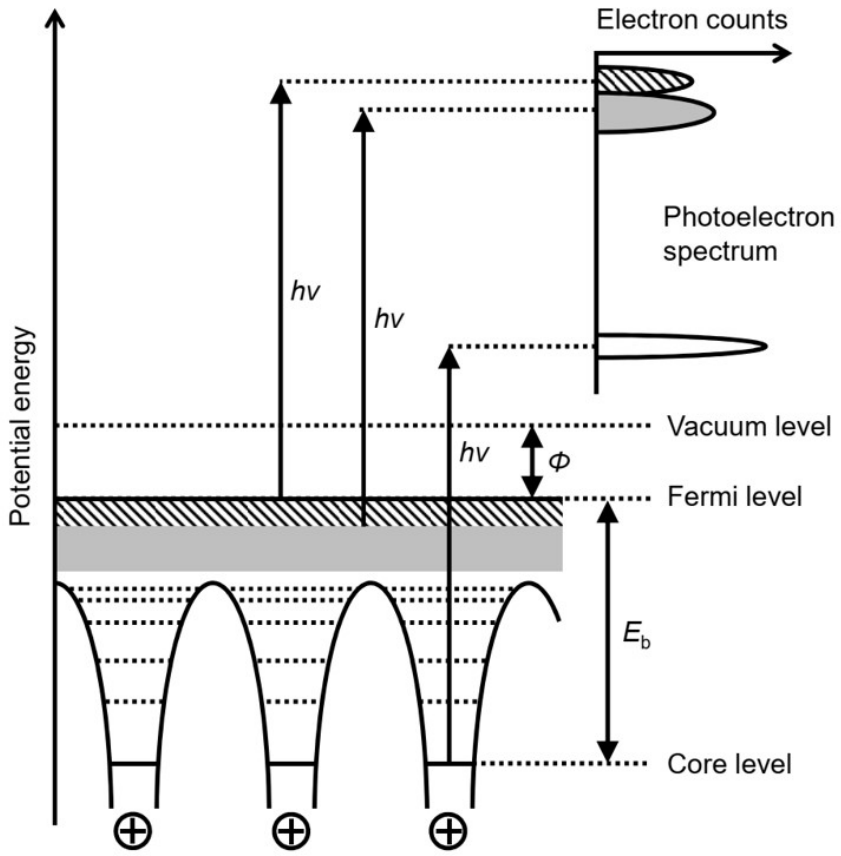

Figure C.1: Schematic diagram of photoelectron emission from solid.

which is called Al Kα.

In addition, in order to perform highly accurate analysis, it is necessary to improve the resolution. By irradiating the monochromator with X-rays, continuous X-rays due to braking radiation and background due to satellite interference can

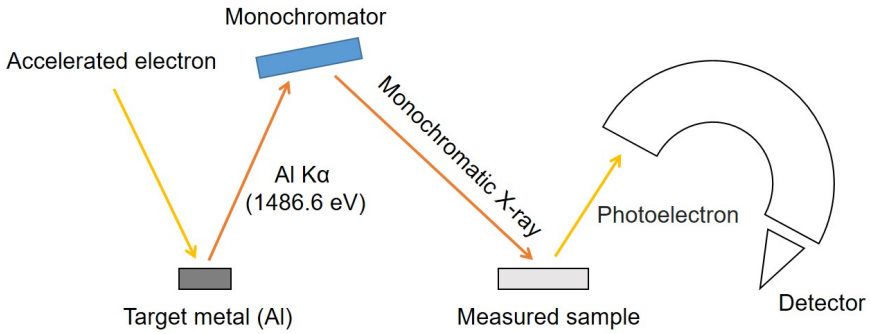

Figure C.2: Schematic diagram of XPS system.

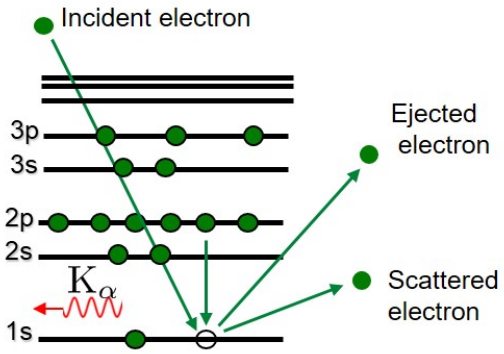

Figure C.3: Al Kα X-ray is emitted when an electron moves from 2p to 1s orbital.

be removed. Bragg equation is given by

$$2d \sin\theta = n\lambda, \tag{C.2}$$

where the X-ray having the wavelength λ among the X-rays incident at the Bragg angle θ with respect to the crystal having the interplanar spacing d is reflected. Quartz crystal is used for the Al radiation source ($\lambda = 0.83$ nm), when using quartz (1010) surface with $d = 0.425$ nm, θ becomes 78.5°, which is convenient for the arrangement of each device. The monochromated X-rays are irradiated to the sample, and the photoelectrons emitted from the sample are converged and decelerated by the electron lens and enter a concentric hemispherical analyzer (CHA). Here, photoelectrons are polarized by flight trajectories by electric field, where energy sorting is carried out. They are converted into electric signals by detectors and recorded as photoelectron spectra.

Appendix D

Some general calculations for fluctuations in electronic devices

D.1 Relative fluctuations

If a physical quantity x can be expressed by a sum of x_1 and x_2, we have

$$\begin{aligned} x &= x_1 + x_2, \\ \langle x^2 \rangle &= \langle (x_1 + x_2)^2 \rangle \\ &= \langle (x_1^2 \rangle + \langle x_2^2 \rangle + 2\langle x_1 x_2 \rangle, \\ \langle x \rangle^2 &= \langle x_1^2 \rangle^2 \\ &= (\langle x_1 \rangle + \langle x_2 \rangle)^2 \\ &= \langle (x_1^2 \rangle + \langle x_2^2 \rangle + 2\langle x_1 \rangle \langle x_2 \rangle. \end{aligned} \tag{D.1}$$

By using an assumption of the independence

$$\langle x_1 x_2 \rangle = \langle x_1 \rangle \langle x_2 \rangle, \tag{D.2}$$

we have

$$\begin{aligned} S_x &= \langle x^2 \rangle - \langle x \rangle^2 \\ &= (\langle x_1^2 \rangle - \langle x_1 \rangle^2) + (\langle x_2^2 \rangle - \langle x_2 \rangle^2) = S_{x_1}^{(1)} + S_{x_2}^{(2)}, \end{aligned} \tag{D.3}$$

or

$$\begin{aligned}\frac{S_x}{\langle x\rangle^2} &= \frac{S_{x_1}^{(1)}}{\langle x\rangle^2} + \frac{S_{x_1}^{(1)}}{\langle x\rangle^2} \\ &= \frac{S_{x_1}^{(1)}}{\langle x_1\rangle^2}\frac{\langle x_1\rangle^2}{\langle x\rangle^2} + \frac{S_{x_2}^{(2)}}{\langle x_2\rangle^2}\frac{\langle x_2\rangle^2}{\langle x\rangle^2}.\end{aligned} \tag{D.4}$$

If $x_1 = x_2 = x/2$, we have

$$\frac{S_x}{\langle x\rangle^2} = \frac{S_{x_1}^{(1)} + S_{x_2}^{(2)}}{\langle x_1 + x_2\rangle^2} = \frac{2S_{x_1}^{(1)}}{4\langle x_1\rangle^2} = \frac{2S_{x_2}^{(2)}}{4\langle x_2\rangle^2}. \tag{D.5}$$

D.2 Correlation between current/voltage and conductance/resistance fluctuations

Current I flowing in a conductor with conductance G or voltage V drop between two ends of a resistor with resistance R does not fluctuate itself, it only reflects the resistance/conductance fluctuations. To measure ideally current fluctuations, we keep the voltage constant, hence

$$\frac{S_I}{\langle I\rangle^2} = \frac{\langle I^2\rangle - \langle I\rangle^2}{\langle I\rangle^2} = \frac{\langle (V.G)^2\rangle - \langle V.G\rangle^2}{\langle (V.G)^2\rangle} = \frac{S_G}{\langle G\rangle^2}, \tag{D.6}$$

meaning that the fluctuation of the current is actually that of the conductance.

To measure ideally voltage fluctuations, we keep the current constant, hence

$$\frac{S_V}{\langle V\rangle^2} = \frac{\langle V^2\rangle - \langle V\rangle^2}{\langle V\rangle^2} = \frac{\langle (I.R)^2\rangle - \langle I.R\rangle^2}{\langle (I.R)^2\rangle} = \frac{S_R}{\langle R\rangle^2}, \tag{D.7}$$

meaning that the fluctuation of the voltage is actually that of the resistance.

On the other hand, in case of small fluctuations, i.e.

$$\delta G \to 0,\ \delta R \to 0, \tag{D.8}$$

we have

$$G = \frac{1}{R} \Rightarrow \ln G = -\ln R \Rightarrow \frac{\delta G}{G} = -\frac{\delta R}{R} \Rightarrow \frac{(\delta G)^2}{G^2} = -\frac{(\delta R)^2}{R^2}, \tag{D.9}$$

thus

$$\frac{S_V}{\langle V\rangle^2} = \frac{S_I}{\langle I\rangle^2} = \frac{S_R}{\langle R\rangle^2} = \frac{S_G}{\langle G\rangle^2}. \tag{D.10}$$

Appendix E

Fluctuation of two-variable functions

We consider fluctuation of a quantity that equals to product of two independent variables x and y: $z = xy$. If the product does not have statistical properties, i.e. that is simply the product of two quantities, the variance of the fluctuations of z is

$$\begin{aligned}
\sigma_z = (\delta z)^2 = \langle (z - \langle z \rangle)^2 \rangle &= \langle z^2 \rangle - \langle z \rangle^2 \\
&= \langle x^2 y^2 \rangle - \langle xy \rangle^2 \\
&= \langle x^2 \rangle \langle y^2 \rangle - \langle x \rangle^2 \langle y \rangle^2 \\
&= \langle x^2 \rangle \langle y^2 \rangle - \langle x^2 \rangle \langle y \rangle^2 + \langle x^2 \rangle \langle y \rangle^2 - \langle x \rangle^2 \langle y \rangle^2 \\
&= \langle x^2 \rangle \sigma_y + \langle y \rangle^2 \sigma_x \\
&= [\sigma_x + \langle x \rangle^2] \sigma_y + \langle y \rangle^2 \sigma_x \\
&= \sigma_x \sigma_y + \langle x \rangle^2 \sigma_y + \langle y \rangle^2 \sigma_x .
\end{aligned} \tag{E.1}$$

Hence

$$\begin{aligned}
\frac{\sigma_z}{\langle z \rangle^2} &= \frac{\sigma_x}{\langle x \rangle^2} \frac{\sigma_y}{\langle y \rangle^2} + \frac{\sigma_x}{\langle x \rangle^2} + \frac{\sigma_y}{\langle y \rangle^2} \\
&\simeq \frac{\sigma_x}{\langle x \rangle^2} + \frac{\sigma_y}{\langle y \rangle^2},
\end{aligned} \tag{E.2}$$

if

$$\frac{\sigma_x}{\langle x \rangle^2} \ll 1, \text{ or } \frac{\sigma_y}{\langle y \rangle^2} \ll 1. \tag{E.3}$$

If the product has statistical properties, e.g.

$$z = Nx = \sum_{i=1}^{N} x_i, \tag{E.4}$$

the variance of the fluctuations of z is

$$\sigma_z = \langle z^2 \rangle - \langle z \rangle^2 = \langle (\sum_{i=1}^{N} x_i)^2 \rangle - \langle \sum_{i=1}^{N} x_i \rangle^2. \tag{E.5}$$

Using Burgess theorem, we obtain

$$\langle \sum_{i=1}^{N} x_i \rangle = \langle \langle \sum_{i=1}^{N} x_i \rangle_{(x)} \rangle_{(N)} = \langle \sum_{i=1}^{N} \langle x \rangle \rangle_{(N)} = \langle x \rangle \langle \sum_{i=1}^{N} 1 \rangle_{(N)} = \langle x \rangle \langle N \rangle, \tag{E.6}$$

and

$$\langle (\sum_{i=1}^{N} x_i)^2 \rangle = \langle \sum_{i=1}^{N} x_i^2 + \sum_{i \neq j}^{N} x_i x_j = \langle \sum_{i=1}^{N} x_i^2 \rangle + \langle \sum_{i \neq j}^{N} x_i x_j \rangle. \tag{E.7}$$

Similarly to Eq. (E.6), we have

$$\langle \sum_{i=1}^{N} x_i^2 \rangle = \langle x^2 \rangle \langle N \rangle, \tag{E.8}$$

and

$$\begin{aligned} \langle \sum_{i \neq j}^{N} x_i x_j \rangle &= \langle \sum_{i \neq j}^{N} \langle x_i x_j \rangle \rangle_{(N)} = \langle \sum_{i \neq j}^{N} \langle x_i \rangle \langle x_j \rangle \rangle_{(N)} = \langle \sum_{i \neq j}^{N} \langle x \rangle^2 \rangle_{(N)} \\ &= \langle x \rangle^2 \langle \sum_{i \neq j}^{N} 1 \rangle_{(N)} = \langle x \rangle^2 \langle N^2 - N \rangle. \end{aligned} \tag{E.9}$$

Hence, Eq. (E.7) becomes

$$\langle (\sum_{i=1}^{N} x_i)^2 \rangle = \langle x^2 \rangle \langle N \rangle + \langle x \rangle^2 \langle N^2 - N \rangle. \tag{E.10}$$

From this result, we can obtain

$$\sigma_z = \langle x^2 \rangle \langle N \rangle + \langle x \rangle^2 \langle N^2 - N \rangle - \langle x \rangle^2 \langle N \rangle^2 = \langle N \rangle \sigma_x + \langle x \rangle^2 \sigma_N, \tag{E.11}$$

thus

$$\frac{\sigma_z}{\langle z \rangle^2} = \frac{1}{\langle N \rangle} \frac{\sigma_x}{\langle x \rangle^2} + \frac{\sigma_N}{\langle N \rangle^2}. \tag{E.12}$$

Applying Eq. (E.12) to an electrical current

$$I = Nev = Ne\mu E = eE \sum_{i=1}^{N} \mu_i, \tag{E.13}$$

we have a current fluctuation of which the power spectrum is

$$\frac{S_I}{\langle I \rangle^2} \propto \frac{(\delta I)^2}{\langle I \rangle^2} = \frac{1}{\langle N \rangle} \frac{(\delta \mu)^2}{\langle \mu \rangle^2} + \frac{(\delta N)^2}{\langle N \rangle^2}. \tag{E.14}$$

List of publications

Journal

[1] Son Phuong Le, Duong Dai Nguyen, and Toshi-kazu Suzuki, "Insulator-semiconductor interface fixed charges in AlGaN/GaN metal-insulator-semiconductor devices with Al_2O_3 or AlTiO gate dielectrics", Journal of Applied Physics **123** (3), 034504, 2018.

[2] Duong Dai Nguyen and Toshi-kazu Suzuki, "Interface charge engineering in AlTiO/AlGaN/GaN metal–insulator–semiconductor devices", Journal of Applied Physics **127** (9), 094501, 2020.

[3] Duy Cong Le, Duong Dai Nguyen, Savanna Lloyd, Toshi-kazu Suzuki, and Hideyuki Murata, "Degradation of fluorescent organic light emitting diodes caused by quenching of singlet and triplet excitons", Journal of Materials Chemistry C **8** (42), 14873-14879, 2020.

[4] Duong Dai Nguyen, Takehiro Isoda, Yuchen Deng, and Toshi-kazu Suzuki, "Normally-off operations in partially-gate-recessed AlTiO/AlGaN/GaN field-effect transistors based on interface charge engineering", Journal of Applied Physics **130** (1), 014503, 2021.

Conference

[1] Duong Dai Nguyen, Son Phuong Le, and Toshi-kazu Suzuki, "Threshold voltages of AlGaN/GaN MIS devices depending on Al_xTi_yO gate insulator compositions", 50th Int. Conf. on Solid State Devices and Materials, D-1-03, oral presentation (2018).

[2] Duong Dai Nguyen, Yuchen Deng, and Toshi-kazu Suzuki, "Impacts of nitrogen plasma surface cleaning on threshold voltages of AlTiO/AlGaN/GaN MIS devices", 51st Int. Conf. on Solid State Devices and Materials, PS-4-17, poster presentation (2019).

[3] Hirotomo Demura, Yuchen Deng, Duong Dai Nguyen, and Toshi-kazu Suzuki, "Threshold voltages of AlGaN/GaN metal-insulator-semiconductor devices with AlN or Al2O3 gate insulators", 46th Int. Symp. on Compound Semiconductors, TuB1-6, oral presentation (2019).

[4] Duy Cong Le, Duong Dai Nguyen, Savanna Lloyd, Toshi-kazu Suzuki, and Hideyuki Murata, "Mechanisms of initial luminance loss in fluorescent organic light emitting diodes unveiled by time-resolved spectrocopies", 27th International Display Workshops, OLED1-3, online oral presentation (2020).

[5] Takehiro Isoda, Jumpei Shimura, Duong Dai Nguyen, Yuchen Deng, and Toshi-kazu Suzuki, "Threshold voltage control in AlGaN/GaN MIS devices with AlTiO gate insulators and gate-recess structures", The papers of technical meeting on electron devices, IEE Japan, EDD-21-032, online oral presentation (2021).

[6] Duong Dai Nguyen, Takehiro Isoda, Yuchen Deng, and Toshi-kazu Suzuki, "Interface-charge-engineered normally-off AlTiO/AlGaN/GaN field-effect transistors", 82nd JSAP Autumn Meeting, 13a-N305-4, online oral presentation (2021).

Bibliography

[1] J.-Y. Duboz, Phys. Status Solidi A **176**, 5 (1999).

[2] S. Colak, B. Singer, and E. Stupp, IEEE Electron Device Lett. **1**, 51 (1980).

[3] H. Kroemer, Proceedings of the IRE **45**, 1535 (1957).

[4] T. Mimura, S. Hiyamizu, T. Fujii, and K. Nanbu, Jpn. J. Appl. Phys. **19**, L225 (1980).

[5] Y. Ohno and M. Kuzuhara, IEEE Trans. Electron Devices **48**, 517 (2001).

[6] H. Wang, *Investigation of power semiconductor devices for high frequency high density power converters* (2007).

[7] I. Ferain, C. A. Colinge, and J.-P. Colinge, Nature **479**, 310 (2011).

[8] L. Wang, 25th International Conference on Microelectronics p. 576 (2006).

[9] S. Oktyabrsky and P. D. Ye, *Fundamentals of III-V Semiconductor MOSFETs* (Springer, 2010).

[10] E. O. Johnson, RCA Electronic Components and Devices **13**, 27 (1965).

[11] Y. Jeong, M. Shindo, M. Akabori, and T. kazu Suzuki, Appl. Phys. Express **1**, 021201 (2008).

[12] I. Vurgaftman, J. R. Meyer, and L. R. Ram-Mohan, J. Appl. Phys. **89**, 5815 (2001).

[13] I. Vurgaftman and J. R. Meyer, J. Appl. Phys. **94**, 3675 (2003).

[14] H. Amano, N. Sawaki, I. Akasaki, and Y. Toyoda, Appl. Phys. Lett. **48**, 353 (1986).

[15] C. Bulutay, B. K. Ridley, and N. A. Zakhleniuk, Phys. Rev. B **62**, 15754 (2000).

[16] N. Tanaka, *Nitride compound semiconductor electronic device fabrication process and research on electron transport within the device* (2010).

[17] ITRS (2005), URL `http://www.itrs.net/Links/2005ITRS/Wireless2005.pdf`.

[18] ITRS (2007), URL `http://www.itrs.net/Links/2005ITRS/Wireless2007.pdf`.

[19] ITRS (2009), URL `http://www.itrs.net/Links/2005ITRS/Wireless2009.pdf`.

[20] H. Ohashi, I. Omura, S. Matsumoto, Y. Sato, H. Tadano, and I. Ishii, IEICE Trans. Commun. **87**, 3422 (2004).

[21] F. Bernardini, V. Fiorentini, and D. Vanderbilt, Phys. Rev. B **56**, R10024 (1997).

[22] O. Ambacher, B. Foutz, J. Smart, J. R. Shealy, N. G. Weimann, K. Chu, M. Murphy, A. J. Sierakowski, W. J. Schaff, L. F. Eastman, R. Dimitrov, A. Mitchell, and M. Stutzmann, J. Appl. Phys. **87**, 334 (2000).

[23] M. Khan, A. Bhattarai, J. Kuznia, and D. Olson, Appl. Phys. Lett. **63**, 1214 (1993).

[24] M. Asif Khan, J. N. Kuznia, D. T. Olson, W. J. Schaff, J. W. Burm, and M. S. Shur, Appl. Phys. Lett. **65**, 1121 (1994).

[25] S. Arulkumaran, T. Egawa, H. Ishikawa, and T. Jimbo, Appl. Phys. Lett. **82**, 3110 (2003).

[26] W. Xu, H. Rao, and G. Bosman, Appl. Phys. Lett. **100**, 223504 (2012).

[27] J.-J. Zhu, X.-H. Ma, B. Hou, W.-W. Chen, and Y. Hao, Appl. Phys. Lett. **104**, 153510 (2014).

[28] Y. Liu, J. A. Bardwell, S. P. McAlister, S. Rolfe, H. Tang, and J. B. Webb, Phys. Status Solidi C **0**, 69 (2002).

[29] N. Tsurumi, H. Ueno, T. Murata, H. Ishida, Y. Uemoto, T. Ueda, K. Inoue, and T. Tanaka, IEEE Trans. Electron Devices **57**, 980 (2010).

[30] S. Huang, Q. Jiang, S. Yang, C. Zhou, and K. Chen, IEEE Electron Device Lett. **33**, 516 (2012).

[31] T. Hashizume, S. Ootomo, and H. Hasegawa, Appl. Phys. Lett. **83**, 2952 (2003).

[32] G. Dutta, S. Turuvekere, N. Karumuri, N. DasGupta, and A. DasGupta, IEEE Electron Device Lett. **35**, 1085 (2014).

[33] K.-Y. Park, H.-I. Cho, J.-H. Lee, S.-B. Bae, C.-M. Jeon, J.-L. Lee, D.-Y. Kim, C.-S. Lee, and J.-H. Lee, Phys. Status Solidi C **0**, 2351 (2003).

[34] P. Kordoš, R. Stoklas, D. Gregušová, v. Gaži, and J. Novák, Appl. Phys. Lett. **96**, 013505 (2010).

[35] S. Yang, Z. Tang, K.-Y. Wong, Y.-S. Lin, C. Liu, Y. Lu, S. Huang, and K. Chen, IEEE Electron Device Lett. **34**, 1497 (2013).

[36] C. Liu, E. F. Chor, and L. S. Tan, Appl. Phys. Lett. **88**, 173504 (2006).

[37] A. Kawano, S. Kishimoto, Y. Ohno, K. Maezawa, T. Mizutani, H. Ueno, T. Ueda, and T. Tanaka, Phys. Status Solidi C **4**, 2700 (2007).

[38] S. Yagi, M. Shimizu, M. Inada, Y. Yamamoto, G. Piao, H. Okumura, Y. Yano, N. Akutsu, and H. Ohashi, Solid-State Electron. **50**, 1057 (2006).

[39] T.-Y. Wu, S.-K. Lin, P.-W. Sze, J.-J. Huang, W.-C. Chien, C.-C. Hu, M.-J. Tsai, and Y.-H. Wang, IEEE Trans. Electron Devices **56**, 2911 (2009).

[40] D. Kikuta, K. Ito, T. Narita, and T. Kachi, Appl. Phys. Express **13**, 026504 (2020).

[41] Y. Liu, J. Bardwell, S. McAlister, S. Rolfe, H. Tang, and J. Webb, Phys. Status Solidi C **0**, 69 (2003).

[42] H.-A. Shih, M. Kudo, M. Akabori, and T. Suzuki, Jpn. J. Appl. Phys. **51**, 02BF01 (2012).

[43] H.-A. Shih, M. Kudo, and T. Suzuki, Appl. Phys. Lett. **101**, 043501 (2012).

[44] H.-A. Shih, M. Kudo, and T. Suzuki, J. Appl. Phys. **116**, 184507 (2014).

[45] S. P. Le, T. Q. Nguyen, H.-A. Shih, M. Kudo, and T. Suzuki, J. Appl. Phys. **116**, 054510 (2014).

[46] J.-C. Gerbedoen, A. Soltani, M. Mattalah, M. Moreau, P. Thevenin, and J.-C. D. Jaeger, Diamond Relat. Mater. **18**, 1039 (2009).

[47] T. Q. Nguyen, H.-A. Shih, M. Kudo, and T. Suzuki, Phys. Status Solidi C

10, 1401 (2013).

[48] T. Sato, J. Okayasu, M. Takikawa, and T. Suzuki, IEEE Electron Device Lett. **34**, 375 (2013).

[49] M. Nozaki, K. Watanabe, T. Yamada, H.-A. Shih, S. Nakazawa, Y. Anda, T. Ueda, A. Yoshigoe, T. Hosoi, T. Shimura, and H. Watanabe, Jpn. J. Appl. Phys. **57**, 06KA02 (2018).

[50] J. T. Asubar, Z. Yatabe, D. Gregusova, and T. Hashizume, J. Appl. Phys. **129**, 121102 (2021).

[51] S. Ganguly, J. Verma, G. Li, T. Zimmermann, H. Xing, and D. Jena, Appl. Phys. Lett. **99**, 193504 (2011).

[52] M. Esposto, S. Krishnamoorthy, D. N. Nath, S. Bajaj, T.-H. Hung, and S. Rajan, Appl. Phys. Lett. **99**, 133503 (2011).

[53] M. Ťapajna and J. Kuzmík, Appl. Phys. Lett. **100**, 113509 (2012).

[54] J. Son, V. Chobpattana, B. M. McSkimming, and S. Stemmer, Appl. Phys. Lett. **101**, 102905 (2012).

[55] T.-H. Hung, S. Krishnamoorthy, M. Esposto, D. N. Nath, P. S. Park, and S. Rajan, Appl. Phys. Lett. **102**, 072105 (2013).

[56] M. Ťapajna, M. Jurkovič, L. Válik, Š. Haščík, D. Gregušová, F. Brunner, E.-M. Cho, T. Hashizume, and J. Kuzmík, J. Appl. Phys. **116**, 104501 (2014).

[57] M. Matys, B. Adamowicz, A. Domanowska, A. Michalewicz, R. Stoklas, M. Akazawa, Z. Yatabe, and T. Hashizume, J. Appl. Phys. **120**, 225305 (2016).

[58] M. Ťapajna, L. Válik, F. Gucmann, D. Gregušová, K. Frohlich, Š. Haščík, E. Dobročka, L. Tóth, B. Pécz, and Kuzmík, J. Vac. Sci. Technol. B **35**, 01A107 (2017).

[59] V. Kumar, A. Kuliev, T. Tanaka, Y. Otoki, and I. Adesida, Electron. Lett. **39**, 1758 (2003).

[60] T. Oka and T. Nozawa, IEEE Electron Device Lett. **29**, 668 (2008).

[61] Yong Cai, Yugang Zhou, K. J. Chen, and K. M. Lau, IEEE Electron Device Lett. **26**, 435 (2005).

[62] X. Hu, G. Simin, J. Yang, M. Asif Khan, R. Gaska, and M. Shur, Electron. Lett. **36**, 753 (2000).

[63] Y. Uemoto, M. Hikita, H. Ueno, H. Matsuo, H. Ishida, M. Yanagihara, T. Ueda, T. Tanaka, and D. Ueda, IEEE Trans. Electron Devices **54**, 3393 (2007).

[64] N. Harada, Y. Hori, N. Azumaishi, K. Ohi, and T. Hashizume, Appl. Phys. Express **4**, 021002 (2011).

[65] C. Yadav, P. Kushwaha, S. Khandelwal, J. P. Duarte, Y. S. Chauhan, and C. Hu, IEEE Electron Device Lett. **35**, 612 (2014).

[66] Q. Zhou, B. Chen, Y. Jin, S. Huang, K. Wei, X. Liu, X. Bao, J. Mou, and B. Zhang, IEEE Trans. Electron Devices **62**, 776 (2015).

[67] T. Sato, K. Uryu, J. Okayasu, M. Kimishima, and T. Suzuki, Appl. Phys. Lett. **113**, 063505 (2018).

[68] M. J. Deen and O. Marinov, AIP Conf. Proc. **780**, 3 (2005).

[69] S. P. Le, D. D. Nguyen, and T. Suzuki, J. Appl. Phys. **123**, 034504 (2018).

[70] T. Ui, M. Kudo, and T. Suzuki, Phys. Status Solidi C **10**, 1417 (2013).

[71] S. P. Le, T. Ui, T. Q. Nguyen, H.-A. Shih, and T. Suzuki, J. Appl. Phys. **119**, 204503 (2016).

[72] D. D. Nguyen and T. Suzuki, J. Appl. Phys. **127**, 094501 (2020).

[73] D. D. Nguyen, T. Isoda, Y. Deng, and T. Suzuki, J. Appl. Phys. **130**, 014503 (2021).

[74] Airliquide, *http://www.airliquide.com/*.

[75] F. Bernardini, V. Fiorentini, and D. Vanderbilt, Phys. Rev. B **63**, 193201 (2001).

[76] J. A. Garrido, J. L. Sanchez-Rojas, A. Jimenez, E. Munoz, F. Omnes, and P. Gibart, Appl. Phys. Lett. **75**, 2407 (1999).

[77] E. J. Miller, E. T. Yu, C. Poblenz, C. Elsass, and J. S. Speck, Appl. Phys. Lett. **80**, 3551 (2002).

[78] A. T. Winzer, R. Goldhahn, G. Gobsch, A. Link, M. Eickhoff, U. Rossow, and A. Hangleiter, Appl. Phys. Lett. **86**, 181912 (2005).

[79] H. D. Trinh, M. T. Nguyen, Y. C. Lin, Q. V. Duong, H. Q. Nguyen, and E. Y. Chang, Appl. Phys. Express **6**, 061202 (2013).

[80] F. Marques and J. Jasieniak, Appl. Surf. Sci. **422**, 504 (2017).

[81] M. P. Seah and W. A. Dench, Surf. Interface Anal. **1**, 2 (1979).

[82] T. Hashizume, S. Ootomo, T. Inagaki, and H. Hasegawa, J. Vac. Sci. Technol. **21**, 1828 (2003).

[83] J. Ziegler, J. Biersack, and M. Ziegler, *Srim-the stopping and ranges of ions in solids* (2008).

[84] S. Kucheyev, J. Williams, and S. Pearton, Mater. Sci. Eng. R-Rep. **33**, 51 (2001).

[85] C. Ronning, E. Carlson, and R. Davis, Phys. Rep. **351**, 349 (2001).

[86] S. J. Pearton, C. B. Vartuli, J. C. Zolper, C. Yuan, and R. A. Stall, Appl. Phys. Lett. **67**, 1435 (1995).

[87] X. A. Cao, S. J. Pearton, G. T. Dang, A. P. Zhang, F. Ren, R. G. Wilson, and J. M. Van Hove, J. Appl. Phys. **87**, 1091 (2000).

[88] Q. Zhou, L. Liu, A. Zhang, B. Chen, Y. Jin, Y. Shi, Z. Wang, W. Chen, and B. Zhang, IEEE Electron Device Lett. **37**, 165 (2016).

[89] Q. Hu, B. Hu, C. Gu, T. Li, S. Li, S. Li, X. Li, and Y. Wu, IEEE Trans. Electron Devices **66**, 4591 (2019).

[90] S. Huang, X. Liu, X. Wang, X. Kang, J. Zhang, J. Fan, J. Shi, K. Wei, Y. Zheng, H. Gao, Q. Sun, M. Wang, B. Shen, and K. J. Chen, IEEE Transactions on Electron Devices **65**, 207 (2018).

[91] Z. Zhang, S. Qin, K. Fu, G. Yu, W. Li, X. Zhang, S. Sun, L. Song, S. Li, R. Hao, Y. Fan, Q. Sun, G. Pan, Y. Cai, and B. Zhang, Appl. Phys. Express **9**, 084102 (2016).

[92] M.-J. Kang, M.-S. Lee, G.-H. Choi, I.-H. Hwang, H.-Y. Cha, and K.-S. Seo, Phys. Status Solidi A **214**, 1600726 (2017).

[93] Q. Hu, B. Hu, C. Gu, T. Li, S. Li, S. Li, X. Li, and Y. Wu, IEEE Trans. Electron Devices **66**, 4591 (2019).

[94] M. Hua, Z. Zhang, J. Wei, J. Lei, G. Tang, K. Fu, Y. Cai, B. Zhang, and

K. J. Chen, in *2016 IEEE International Electron Devices Meeting (IEDM)* (2016), pp. 10.4.1–10.4.4.

[95] M. Wang, Y. Wang, C. Zhang, B. Xie, C. P. Wen, J. Wang, Y. Hao, W. Wu, K. J. Chen, and B. Shen, IEEE Trans. Electron Devices **61**, 2035 (2014).

[96] Y. Shi, S. Huang, Q. Bao, X. Wang, K. Wei, H. Jiang, J. Li, C. Zhao, S. Li, Y. Zhou, H. Gao, Q. Sun, H. Yang, J. Zhang, W. Chen, Q. Zhou, B. Zhang, and X. Liu, IEEE Trans. Electron Devices **63**, 614 (2016).

[97] S. Kogan, *Electronic noise and fluctuations in solids* (Cambridge University Press, 1996).

[98] F. Hooge, IEEE Trans. Electron Devices **41**, 1926 (1994).

[99] H. Wong, Microelectron. Reliab. **43**, 585 (2003).

[100] J. B. Johnson, Phys. Rev. **32**, 97 (1928).

[101] H. Nyquist, Phys. Rev. **32**, 110 (1928).

[102] P. Dutta and P. M. Horn, Rev. Mod. Phys. **53**, 497 (1981).

[103] M. B. Weissman, Rev. Mod. Phys. **60**, 537 (1988).

[104] L. Vandamme, X. Li, and D. Rigaud, IEEE Trans. Electron Devices **41**, 1936 (1994).

[105] J. B. Johnson, Phys. Rev. **26**, 71 (1925).

[106] W. Schottky, Phys. Rev. **28**, 74 (1926).

[107] F. Hooge, Phys. Lett. A **29**, 139 (1969).

[108] F. N. Hooge, T. G. M. Kleinpenning, and L. K. J. Vandamme, Rep. Prog. Phys. **44**, 479 (1981).

[109] A. L. McWhorter, *Semiconductor Surface Physics* (University of Pennsylvania Press, 1956).

[110] F. Hooge, Phys. B: Condens. Matter **336**, 236 (2003).

[111] R. F. Voss and J. Clarke, Phys. Rev. B **13**, 556 (1976).

[112] P. Dutta, P. Dimon, and P. M. Horn, Phys. Rev. Lett. **43**, 646 (1979).

[113] P. H. Handel, Phys. Rev. A **22**, 745 (1980).

[114] F. Korndörfer, MOS-AK Meeting **11284** (2007).

[115] M. L. Huang, Y. C. Chang, C. H. Chang, T. D. Lin, J. Kwo, T. B. Wu, and

M. Hong, Appl. Phys. Lett. **89**, 012903 (2006).

[116] B. Enright and D. Fitzmaurice, J. Phys. Chem. **100**, 1027 (1996).

[117] M. D. Stamate, Appl. Surf. Sci. **205**, 353 (2003).

[118] R. Burgess, J. Phys. Chem. Solids **22**, 371 (1961).

[119] M. Grundmann, *The Physics of Semiconductors* (Springer, 2010).